

# A multifrequency method for the solution of the acoustic inverse scattering problem

by

Carlos Eduardo Cardoso Borges

A Thesis

Submitted to the Faculty

of

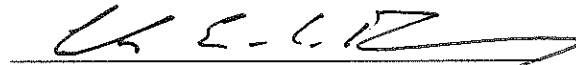
WORCESTER POLYTECHNIC INSTITUTE

In partial fulfillment of the requirements for the

Degree of Doctor of Philosophy

in

Mathematical Sciences



December 2012

APPROVED:



Professor Marcus Sarkis, Advisor  
Department of Mathematical Sciences  
Worcester Polytechnic Institute



Professor Homer Walker  
Department of Mathematical Sciences  
Worcester Polytechnic Institute



Professor L. Ramdas Ram-Mohan  
Department of Physics  
Worcester Polytechnic Institute



Professor Darko Volkov  
Department of Mathematical Sciences  
Worcester Polytechnic Institute



Priv. Doz. Dr. Mourad Sini  
Radon Institute of Computational and  
Applied Mathematics  
Austrian Academy of Sciences



Professor Mahadevan Ganesh  
Department of Applied Mathematics  
and Statistics  
Colorado School of Mines

# Acknowledgments

I would like to thank to my advisor, Prof. Marcus Sarkis. It has been an honor to be his student. I appreciate all his patience, kindness, advices, and am thankful that he has been available for discussions when they were needed and at the same time providing freedom for my research. Without his support, guidance, care, and promptness in both my research and in writing the dissertation, I would not have been able to have completed my work on time.

I would like to thank Prof. Homer Walker for all his useful suggestions. I am also very grateful to Prof. L. Ramdas Ram-Mohan, Prof. Mahadevan Ganesh, Prof. Mourad Sini and Prof. Darko Volkov for their time, and for being part of my committee.

I would like to thank the department for providing the financial support for my entire period at WPI, and all its faculty and staff for their help and kindness. I would also like to thank Prof. Bogdan Vernescu for accepting all my requests for funds to participate in conferences. I would like to thank all of my friends in the department.

I am thankful to my wife for her patience, encouragement, support, and caring. Without her continuous support this endeavor would have been much more tougher for me. I am also grateful to my parents whose encouragement, support, and guidance brought me to this stage.

Finally, I would like to thank General Aléssio Ribeiro Souto for supporting my endeavor in pursuing a Ph.D. outside Brazil. I would also like to thank Brigadier Ramon Borges Cardoso, Colonel Paulo Afonso Cunha, Colonel Antonio Carlos Castañon Vieira and Lieutenant Colonel Samuel Machado Leal da Silva for supporting my request, and for introducing me to General Aléssio Ribeiro Souto.

## Abstract

We are interested in solving the time-harmonic inverse acoustic scattering problem for planar sound-soft obstacles. In this work, we introduce four methods for solving inverse scattering problems. The first method is a variation of the method introduced by Johansson and Sleeman. This method solves the inverse problem when we have the far field pattern given for only one incident wave. It is an iterative method based on a pair of integral equations used to obtain the far field pattern of a known single object. The method proposed in this thesis has a better computational performance than the method of Johansson and Sleeman.

The second method we present is a multi-frequency method called the recursive linearization algorithm. This method solves the inverse problem when the far field pattern is given for multiple frequencies. The idea of this method is that from an initial guess, we solve the single frequency inverse problem for the lowest frequency. We use the result obtained as the initial guess to solve the problem for the next highest frequency. We repeat this process until we use the data from all frequencies. To solve the problem at each frequency, we use the first method proposed. To improve the quality of the reconstruction of the shadowed part of the object, we solve the inverse scattering problem of reconstructing an unknown sound-soft obstacle in the presence of known scatterers. We show that depending on the position of the scatterers, we may be able to obtain very accurate reconstructions of the entire unknown object.

Next, we introduce a method for solving the inverse problem of reconstructing a convex sound-soft obstacle, given measures of the far field pattern at two frequencies that are not in the resonance region of the object. This method is based on the use of an approximation formula for the far field pattern using geometric optics. We are able to prove that for the reconstruction of the circle of radius  $R$  and center at the origin, the size of the interval of convergence of this method is proportional to the inverse of the wavenumber. This procedure is effective at reconstructing the illuminated part of the object; however, it requires an initial guess close to the object for frequencies out of the resonance region.

Finally, we propose a globalization technique to obtain a better initial guess to solve the inverse problem at frequencies out of the resonance region. In this technique, given the far field pattern of a convex object at two frequencies out of the resonance region, we use our extrapolation operator to generate synthetic data for low frequencies. We apply the recursive linearization algorithm, using as a single frequency solver the method that is based on geometric optics. We obtain an approximation of the object that can be used as the initial guess to apply the recursive linearization algorithm using the first method introduced as the single frequency solver.

# List of Figures

2.1	The direct scattering problem . . . . .	9
2.2	The inverse scattering problem . . . . .	16
2.3	Newton’s method for the inverse problem . . . . .	22
2.4	Backtracking line-search framework . . . . .	31
2.5	The heuristic Method B . . . . .	32
2.6	The Recursive Linearization Algorithm. . . . .	34
2.7	Recursive Linearization Algorithm using Method B . . . . .	34
4.1	Matrices for the B-spline $H^1$ -penalty term . . . . .	49
4.2	Numerical implementation of Method B . . . . .	53
4.3	Plot of reconstruction Methods A and B . . . . .	57
4.4	Comparison of the B-spline and trigonometric polynomial solution spaces . . . . .	67
4.5	Influence of frequency and initial guess on the solution of the inverse problem I . . . . .	68
4.6	Influence of frequency and initial guess on the solution of the inverse problem II . . . . .	69
4.7	Implementation of the RLA-B . . . . .	70
4.8	Multifrequency method for the Kite . . . . .	71
4.9	Multifrequency method for the 7-gear . . . . .	72
4.10	Multifrequency method for the 9-gear . . . . .	73
4.11	Multifrequency method for the 15-gear . . . . .	74
4.12	Residue $\times$ frequency for multi-frequency method . . . . .	75
4.13	Multifrequency method in the presence of known objects . . . . .	76
4.14	Residue $\times$ frequency for multifrequency method in the presence of known objects . . . . .	77
5.1	Far field pattern for $S^1$ and $k = 10$ : Nyström $\times$ Kirchhoff . . . . .	84
5.2	Far field pattern for Egg and $k = 10$ : Nyström $\times$ Kirchhoff . . . . .	85
5.3	Far field pattern for the Kite and $k = 20$ : Nyström $\times$ Kirchhoff . . . . .	86
5.4	Kirchhoff based iterative method . . . . .	92
5.5	Far field generation for the ellipse using $k_a = 19$ and $k_b = 20$ . . . . .	107
5.6	Error with respect to the far field obtained with the Nyström method of the data generated for the ellipse using $k_a = 19$ and $k_b = 20$ . . . . .	108
5.7	Error with respect to the Kirchhoff approximation of the far field generated for the ellipse using $k_a = 19$ and $k_b = 20$ . . . . .	109
5.8	Far field generation for the rotated Egg using $k_a = 11$ and $k_b = 12$ . . . . .	110
5.9	Error with respect to the far field obtained with the Nyström method of the data generated for the Egg using $k_a = 11$ and $k_b = 12$ . . . . .	111

5.10	Error with respect to the Kirchhoff approximation of the data generated for the Egg using $k_a = 11$ and $k_b = 12$ . . . . .	112
5.11	Far field generation for the Kite using data for $k_a = 14$ and $k_b = 15$ . . . . .	113
5.12	Error with respect to the far field obtained with the Nyström method of the data generated for the Kite using $k_a = 14$ and $k_b = 15$ . . . . .	114
5.13	Error with respect to the Kirchhoff approximation of the far field generated for the Kite using $k_a = 14$ and $k_b = 15$ . . . . .	115
5.14	Applying the RLA-C method to find the ellipse having $k_a = 50$ and $k_b = 51$ .	116
5.15	Applying the RLA-C method to find the Egg having $k_a = 55$ and $k_b = 56$ . .	116
5.16	Applying the RLA-C method to find the Kite having $k_a = 45$ and $k_b = 46$ . .	117
5.17	Applying the RLA-C method to find the Egg using $\epsilon_{\hat{x}} = \pi/2, \pi/4$ and $\pi/8$ .	118

# List of Tables

3.1	Far field for the circle of radius 1 . . . . .	42
3.2	Far field pattern for the Kite . . . . .	42
4.1	Comparison of the reconstruction of the Pear using Methods A and B . . . .	56
4.2	Comparison of the B-spline and trigonometric polynomial solution spaces . .	59
5.1	Convergence interval for the circle problem with $u_\infty$ . . . . .	97
5.2	Convergence interval for the circle problem with $\tilde{u}_\infty$ . . . . .	97

# Contents

<b>1</b>	<b>Introduction</b>	<b>1</b>
<b>2</b>	<b>Formulation of the problem</b>	<b>9</b>
2.1	Direct scattering problem . . . . .	9
2.1.1	Introduction to the direct scattering problem . . . . .	9
2.1.2	Direct scattering problem with multiple objects . . . . .	15
2.2	Inverse scattering problem . . . . .	16
2.2.1	Introduction to the inverse scattering problem . . . . .	16
2.2.2	Ill-posed problems and regularization . . . . .	17
2.2.3	Newton method for a single frequency . . . . .	19
2.2.4	The variation of the Method of Johansson and Sleeman–Method B . . . . .	24
2.2.5	Globalization techniques . . . . .	30
2.2.6	The use of multiple frequencies . . . . .	31
2.2.7	Inverse scattering of a single object in the presence of multiple scatterers . . . . .	35
<b>3</b>	<b>Numerical solution of the direct problem at low frequencies</b>	<b>36</b>
3.1	The case of a single scatterer . . . . .	36
3.1.1	Numerical implementation . . . . .	36
3.1.2	Numerical analysis . . . . .	40
3.1.3	Numerical results . . . . .	41
3.2	The case of multiple scatterers . . . . .	43
<b>4</b>	<b>Numerical solution of the inverse problem at low frequencies</b>	<b>45</b>
4.1	Inverse scattering problem for a single frequency . . . . .	45
4.1.1	Implementation of Method B . . . . .	45
4.1.2	Numerical results . . . . .	54
4.2	Inverse scattering problem for multiple frequencies . . . . .	61
4.2.1	Numerical implementation of the RLA-B . . . . .	62
4.2.2	Numerical results . . . . .	63
4.3	Inverse scattering problem for multiple frequencies in the presence of multiple scatterers . . . . .	64
4.3.1	Numerical results . . . . .	65

<b>5</b>	<b>A globalization technique for inverse problems</b>	<b>78</b>
5.1	Direct problem at frequencies out of the resonance region for convex objects	79
5.1.1	The Kirchhoff approximation formula . . . . .	79
5.1.2	Numerical implementation and results . . . . .	83
5.2	Inverse problems using the Kirchhoff approximation formula . . . . .	87
5.2.1	Inverse problem for single frequency using the Kirchhoff approximation formula . . . . .	87
5.2.2	Numerical implementation of Method C . . . . .	90
5.2.3	The special case of the circle with fixed center . . . . .	93
5.3	Globalization technique for frequencies out of the resonance region . . . . .	98
5.3.1	Generating synthetic data . . . . .	98
5.3.2	Inverse problem for multiple frequency using Kirchhoff approximation	102
5.3.3	Numerical results using the RLA-C method . . . . .	104
<b>6</b>	<b>Conclusion</b>	<b>119</b>

# Chapter 1

## Introduction

There is an increasing interest in the solution of inverse problems in the areas of

- medical imaging: reconstruction and location of tumors;
- non-destructive testing: location of cracks in materials;
- defense applications: radar and sonar, and land mine detection;
- analysis of subsurface strata for resource identification and recovery: oil and prospecting;

In these types of problem, a set of measured data is given from experimentation and, using this data, the goal is to reconstruct the object or its properties. We consider in this thesis the problem of acoustic scattering by infinitely long cylinders; namely, we solve the associated direct and inverse scattering problems.

The propagation of acoustic waves in a homogeneous isotropic medium with constant speed of sound  $c$  is governed by the wave equation

$$\Delta U = \frac{1}{c^2} \frac{\partial^2 U}{\partial t^2},$$

for the potential  $U(x, t)$ . If we consider time-harmonic waves with frequency  $\omega$ , then we can factor out the time dependence and obtain

$$U(x, t) = \operatorname{Re} (u(x)e^{-i\omega t}),$$

which, used in the wave equation, gives us the Helmholtz equation

$$\Delta u + k^2 u = 0,$$

where  $k = \omega/c$ ,  $k > 0$  is the wavenumber. We consider two types of problems for sound-soft obstacles  $D$ :

1. Direct scattering problem: Given an incident plane wave  $u^{\text{inc}} = e^{ikx \cdot d}$  for  $x \in \mathbb{R}^2$ , find the scattered field  $u^{\text{scat}}$  such that it satisfies the Helmholtz equation

$$\Delta u^{\text{scat}} + k^2 u^{\text{scat}} = 0 \quad \text{in } \mathbb{R}^2 \setminus \overline{D},$$

the boundary condition

$$u^{\text{scat}} = -u^{\text{inc}} \quad \text{on } \partial D,$$

and the Sommerfeld radiation condition

$$\lim_{r \rightarrow \infty} \sqrt{r} \left( \frac{\partial u^{\text{scat}}}{\partial \nu} - ik u^{\text{scat}} \right) = 0, \quad r = |x|.$$

The radiation condition implies that the scattered wave has the asymptotic behavior of an outgoing cylindrical wave

$$u^{\text{scat}} = \frac{e^{ik|x|}}{\sqrt{|x|}} \left[ u_\infty(\hat{x}) + \mathcal{O}\left(\frac{1}{|x|}\right) \right], \quad |x| \rightarrow \infty,$$

in all directions  $\hat{x} = \frac{x}{|x|}$ . We call the function  $u_\infty$  the far field pattern of the object  $D$ .

2. Inverse scattering problem: Given the far field pattern  $u_\infty$  of a sound-soft object  $D$  for one or several incident plane waves  $u^{\text{inc}}$ , reconstruct the shape of the scatterer  $D$ .

In the literature, there are several different known methods of solving this inverse problem. In his paper [1], Kress classified the inverse scattering methods by three different types: iterative, decomposition and sampling methods. The description of each is as follows:

1. Iterative methods: The inverse problem is interpreted as a nonlinear ill-posed operator equation

$$F(\partial D) = u_\infty,$$

where the operator  $F : \partial D \rightarrow u_\infty$  maps the boundary  $\partial D$  of the scatterer onto the far field pattern  $u_\infty$  generated by the scattering of the incident plane wave  $u^{\text{inc}}$ . This equation is solved by iteration methods such as regularized Newton's methods, Landweber iterations or conjugate gradient methods. These methods generally produce good results; however, they require the solution of the direct problem at each step. For details, see [2–4].

2. Decomposition methods: These methods separate the nonlinear ill-posed inverse problem into an ill-posed problem to reconstruct the scattered field  $u^{\text{scat}}$  from the far field pattern  $u_\infty$ , and a non-linear problem to reconstruct the domain  $\partial D$  using the boundary condition. Some examples are the potential method of Kirsch and Kress [5], and the point-source method of Potthast [6–8]. The main advantage of these methods is that they do not require a forward solver. The disadvantage is that in general, good *a priori* information on the unknown scatterer is needed, and the quality of the reconstruction is inferior to that given by Newton's method.

3. Sampling methods: In these methods, we choose an indicator function  $f$  on  $\mathbb{R}^n$ , where  $n$  depends on the dimension of the problem that we are solving, such that depending on the value of the function at a point in the domain, this point may be inside or outside the scatterer. Some examples are the linear sampling method by Colton and Kirsch [9], the singular source method by Potthast [8; 10], the factorization method by Kirsch [11], and the probe method by Ikehata [12]. The advantages of these methods are their simple implementation and the fact that we do not need *a priori* information on the object. The disadvantages are that these methods require a great amount of data and the quality of their reconstruction depends on the number of points where the indicator function is evaluated.

Some approaches that combine the ideas of these methods have been presented. One of these approaches, called the hybrid method, was presented by Kress in [4], and implemented and analyzed by Serranho in [13].

Another approach was presented by Kress and Rundell for the problem of reconstructing the shape of a perfectly conducting inclusion within a two-dimensional homogeneous host medium from overdetermined Cauchy data in [14], not the far field pattern, and later adapted for the case of inverse obstacle and crack scattering [15]. This approach is based on nonlinear integral equations arising from Green's integral theorem. Both of these equations are solved iteratively. The advantage of this method compared with Newton's method is that the derivative of the integral operators in this method with respect to the domain are boundary integral operators that can be expressed in explicit form. The disadvantage is that the system that we need to solve in each iteration is composed of two coupled equations, and is thus relatively large.

Finally, Johansson and Sleeman implemented and analyzed in [16] a method proposed by Sleeman in [17] for reconstruction of the shape of a two-dimensional sound-soft obstacle with a polar representation using measures of the far field pattern for one incident wave. We refer to this method as Method A. This method was later extended for domains represented by more general curves by Ivanyshyn and Johansson in [18]. The idea of this method is very similar to that of the method developed in [14]: to decompose the problem into two different integral equations obtained using Green's integral theorem. We point out that this method is for the far field pattern of the scattered field, while in [14], the method is used for the near field measures of the scattered field. Johansson and Sleeman's method was introduced as faster and easier to implement than the classical Newton's method [3]. In the Johansson and Sleeman algorithm, an initial guess for the solution is chosen and a pair of integral equations, one related to the boundary condition of the problem and another related to the linearization of the integral equation associated with the far field measure, is solved iteratively. After solving this pair of equations, an approximation of the domain is updated. We repeat this process until we reach a stopping criterion, *i.e.*, when the desired number of iterations, absolute value of the residue, or other criteria are reached [19; 20].

The first problem that we deal with in this thesis is to reconstruct the shape of the sound-soft obstacle  $D$  given the far field pattern measures generated by one incident wave. We can phrase the problem as the following:

**Problem 1** *Given the far field pattern measures  $u_\infty(\hat{x}_l)$  at the  $N_{ff}$  points  $\hat{x}_l \in \Omega$ , where  $\Omega$  is the unit circle, generated by the scattering of the incident plane wave  $u^{inc}(x) = e^{ikx \cdot d}$  with fixed direction  $d$  and wavenumber  $k$  by an unknown sound-soft object  $D$ , reconstruct the shape of the object  $D$ .*

We develop in this thesis a variation of Method A, which we call Method B. We believe that Johansson and Sleeman's method has a slight advantage over Ivanyshyn's method, due to the smaller system that is solved at each iteration, and because it is simpler to implement.

In this thesis, we present in Chapter 2 a variation of Johansson and Sleeman's method that produces equivalent results to Johansson and Sleeman's method, but has better computational performance, requiring fewer iterations in general.

In each of these methods, we must determine the set in which to look for solutions. We consider that the scatterer  $D$  that we want to reconstruct is star shaped, having a parameterization  $x : [0, 2\pi] \rightarrow \mathbb{R}^2$ , where  $x(t) = x_r(t) (\cos(t), \sin(t))$ . When solving the problem, we must choose a space in which to look for the function  $x_r(t)$ . We tested two spaces:

- The space of trigonometric polynomials, with  $x_r(t) > 0$  and  $x_r(0) = x_r(2\pi)$ , and
- The space of B-splines, with  $x_r(t) > 0$  and  $x_r(0) = x_r(2\pi)$ .

Comparison of the results obtained by solving the inverse problem using the two spaces showed that both produce reconstructions with the same quality; however, the reconstruction using trigonometric polynomials is computationally less expensive than that using B-splines.

The choice of initial guess is fundamental to obtain convergence of Methods A and B to the correct solution. When we apply these algorithms, it becomes clear that at low frequencies we are able to obtain fuzzy reconstructions of the object using initial guesses that are not very close to the object, while when we increase the frequency we can obtain sharp reconstructions of the object, and this requires an initial guess much closer to the object to be reconstructed.

It was pointed out by Chen in [21] that we cannot determine features of the scatterer that are less than half a wavelength in size. Thus, to obtain a detailed reconstruction of the object, we must use frequencies high enough to reconstruct the details. The main issue of increasing the frequency is that for frequencies out of the resonance region, the initial guess used in the method to reconstruct the object needs to be closer to the solution. Chen considered the following problem:

**Problem 2** Given  $N_{total} = N_{ff} \times N_{inc}$  far field pattern measures at the  $N_{ff}$  points  $\hat{x}_l \in \Omega$ , where  $\Omega$  is the unit circle, generated by the scattering of the  $N_{inc}$  incident plane waves  $u_j^{inc}(x) = e^{ik_j x \cdot d}$  with fixed direction  $d$  and varying wavenumbers  $k_j$  for  $j = 1, \dots, N_{inc}$ , by an unknown sound-soft object  $D$ , where  $k_1 < k_2 < \dots < k_{N_{inc}}$ , reconstruct the shape of the object  $D$ .

To solve this problem, we use the Recursive Linearization Algorithm (RLA) that was proposed by Chen in [21] for the potential problem. This algorithm was later analyzed by Bao and Triki in [22] for the case of the inhomogeneous problem with noiseless data and by Sini and Nguyen in [23] for the case of impenetrable sound-soft obstacles with the presence of noise. The idea of this algorithm is to replace the nonlinear least-squares objective functional at each frequency by a linearized one using the Taylor expansion at the solution at a lower frequency. When lower frequency data is available, it is possible to use an initial guess not so close to the object for Newton's method [3]. Once a desired approximation of the object is found for a lower frequency, it is used as an initial guess to reconstruct the object at a higher frequency. We repeat this process iteratively for the data up to the highest frequency available. If the amount of data available for all frequencies is sufficient, it is possible to obtain a very sharp approximation of the part of the object illuminated by the plane wave. A drawback of this method is that it is not possible to obtain a very good reconstruction of the object in the shadowed part. Another problem with the method is that we need the far field pattern scattered by the object at very low frequencies if we want to start the method with an initial guess that is not very close to the object. Another issue is that Newton's method is computationally very expensive, since several integral equations are required to perform the linearization. Here, we use Method B instead of Newton's method in [3]. We denote this Method by RLA-B, because for each frequency we solve the problem using Method B. The reconstructions obtained by our method have the same quality as the reconstructions obtained in [23].

Unfortunately, neither RLA-B nor the RLA method of Chen are effective in producing good reconstructions in the shadowed part of the object. To remedy this setback, Nguyen and Sini (work in progress) make use of known scatterers to obtain good approximations of the shadowed part of the object, where these known scatterers are placed in such a position as to reflect the incident wave, and thereby illuminate the shadowed part of the object that we intend to recover. Implementing a similar algorithm using Method B, we move from a single object scattering problem to a multiple object scattering problem, for which the implementation is well discussed in Martin [24], and in Ganesh and Hawkins [25]. We must be very careful when introducing the scatterers into our configuration. In the implementation of RLA-B with multiple scatterers, we prefer to insert objects with simple geometries, such as circles or ellipses. The distance from the inserted object to the object that we want to reconstruct cannot be too short, otherwise the results are not satisfactory. The size and position of the objects should be chosen to best reflect the incident wave onto the shadowed part of the object.

Finally, we consider a different problem, in which we do not have far field pattern measures at several different frequencies, in particular, at low frequencies. We assume that we

have only the far field data for two frequencies  $k_a$  and  $k_b$ , where  $k_a < k_b$ , and  $k_a$  and  $k_b$  are frequencies outside of the resonance region of the object. We also assume that the scatterer is strictly convex. The problem is as follows:

**Problem 3** *Given  $2N_{ff}$  far field pattern measures at the  $N_{ff}$  points  $\hat{x}_l \in \Omega$ , where  $\Omega$  is the unit circle, generated by the scattering of two incident plane waves  $u_j^{inc}(x) = e^{ik_j x \cdot d}$  with fixed direction  $d$  and varying wavenumbers  $k_a$  and  $k_b$ , by an unknown sound-soft strictly convex object  $D$ , where  $k_a < k_b$ , and  $k_a$  is of a greater order of magnitude than the radius of the object, reconstruct the shape of the object  $D$ .*

In this case, there are two main issues for solving this problem. One issue is that the forward solver becomes computationally expensive when the frequency is very high. We do not deal with this issue in this thesis, but to solve this issue, we direct the reader to the work of Bruno *et al.* [26] and of Giladi [27], which was based on the works of Keller [28–30]. The other issue is that at higher frequencies, we need to provide an initial guess for the method very close to the object that we want to reconstruct, and most of the time we do not have such a good initial guess available.

To obtain a good initial guess to be used for solving the problem at the  $k_a$  wavenumber, we present a set of procedures. First, we present an approximation formula based on the Kirchhoff approximation of the scattered field at frequencies out of the resonance region for strictly convex objects. The derivation of this formula follows [31]. It is derived using the stationary phase method for highly oscillatory integrals [32], and the geometric optics approximation

$$\frac{\partial u}{\partial \nu}(x) = \begin{cases} 2 \frac{\partial u^{inc}}{\partial \nu}(x), & \text{for } x \in \partial D_d^+ \\ 0, & \text{for } x \in \partial D_d^-, \end{cases}$$

where  $\partial D_d^+$  is the part of the object  $D$  illuminated by the incident plane wave  $u^{inc}$  with incidence direction  $d$  and  $\partial D_d^-$  is the shadowed part of the object. We propose a method, which we call Method C, to reconstruct the shape of a strictly convex obstacle based on this approximation formula. We prove, see Theorem 5.2.3, that the size of the interval of convergence of this method for the reconstruction of a circle of radius  $R$  centered at the origin is proportional to the inverse of the wavenumber.

Next, using the approximation formula obtained for the far field pattern, we are able to obtain an operator that generates far field synthetic data for low wavenumbers using the far field pattern for the wavenumbers  $k_a$  and  $k_b$ . The data is generated in general for wavenumbers lower than  $k_a$ . The quality of the data generated by this operator is good in the illuminated part of the object; however, in the shadowed part of the object the approximation is not efficient.

Finally, our globalization technique is based on the extrapolator operator of synthetic data. We call this Method RLA-C. We do the following:

1. Given the far field data for the wavenumbers  $k_a$  and  $k_b$ , we generate synthetic far field data for lower frequencies, in this case, as many as we judge are necessary to implement the globalization technique;
2. Apply the RLA with Method C for each wavenumber lower than  $k_a$ , using the data generated by the extrapolator operator;
3. Use the solution obtained in the previous step as the initial guess for the Method RLA-B for the wavenumbers  $k_a$  and  $k_b$ .

We present some results of the application of this method for the reconstruction of obstacles that have an illuminated convex part, obtaining good approximations. If the same initial guess used for those reconstructions were used for the RLA-B for each frequency for the data given for the wavenumbers  $k_a$  and  $k_b$ , the method would not converge. This shows that our globalization technique RLA-C is effective.

The outline of this thesis is the following:

- In Chapter 2, we present the theory of the direct and inverse acoustic scattering problems. To solve the inverse scattering problem, we present a variation of Johansson and Sleeman's method called Method B. We also present the RLA-B method, which has the framework of the RLA and uses Method B as the solver for each frequency. We finish Chapter 2 presenting the reconstruction of an unknown sound-soft obstacle in the presence of known scatterers.
- In Chapter 3, we present the details of the numerical implementation of the direct scattering problem. We follow the ideas in [3; 33; 34] and derive the formulas for the use of the Nyström method for the solution of the direct scattering problem.
- In Chapter 4, we present the details of the numerical implementation of the inverse scattering methods. We start by presenting the implementation of Method B, followed by numerical examples of the use of this method for the solution of the inverse scattering problem. We also compare the performance of Method B with that of Method A using numerical examples. Method A is shown to be computationally more expensive than Method B. Next, we present details of the numerical implementation of the RLA for the multi-frequency inverse problem using the Method B as the solver for each frequency. We present numerical results showing improvement in the reconstruction of details using this method. This method does not produce good approximations of the shadowed part of the object. To improve the quality of the reconstruction of the shadowed part of the object, we show the implementation of Method RLA-B for the reconstruction of an unknown sound-soft obstacle in the presence of known scatterers.

We finish Chapter 4 by presenting some numerical examples confirming the effectiveness of the multiple object scattering technique.

- In Chapter 5, we begin by presenting an approximation formula to calculate the far field pattern of a strictly convex object  $D$  that uses the Kirchhoff approximation for incident waves with frequency out of the resonance region. We present some examples showing the accuracy of this formula in the illuminated part of  $D$ . Next, we present an iterative method based on the approximation formula for the far field pattern, to reconstruct the convex object  $D$ , and we refer to this procedure as Method C. We are able to prove that for the reconstruction of a circle centered at the origin and of radius  $R$ , the size of the interval of convergence of the method is  $\mathcal{O}(1/k)$ . Next, we present a procedure for generating synthetic far field data, where we have the far field patterns  $u_\infty^{k_a}$  and  $u_\infty^{k_b}$ , for wavenumbers  $k_a$  and  $k_b$ , where  $k_a < k_b$ , and where the order of magnitude of  $k_a$  is higher than the radius of the object. We present some examples showing the quality of the generated data compared with the data given from the integral equation formulation of Chapter 3. Finally, we present a globalization procedure to reconstruct the object given the far field pattern  $u_\infty^{k_a}$  and  $u_\infty^{k_b}$ , for wavenumbers  $k_a$  and  $k_b$ , where  $k_a < k_b$ , and where the order of magnitude of  $k_a$  is higher than the radius of the object. We make use of this procedure to generate synthetic data together with the RLA to obtain a good initial guess for our problem. For the synthetic data, instead of using Method B for each wavenumber of the RLA, we use the Method C. We present details of the numerical implementation of Method RLA-C. We present some results of the method applied to the reconstruction of strictly convex obstacles and to the reconstruction of an object that has a convex illuminated part.
- In Chapter 6, we present the conclusion of our results, with a discussion of possible future works and problems for research.

# Chapter 2

## Formulation of the problem

### 2.1 Direct scattering problem

#### 2.1.1 Introduction to the direct scattering problem

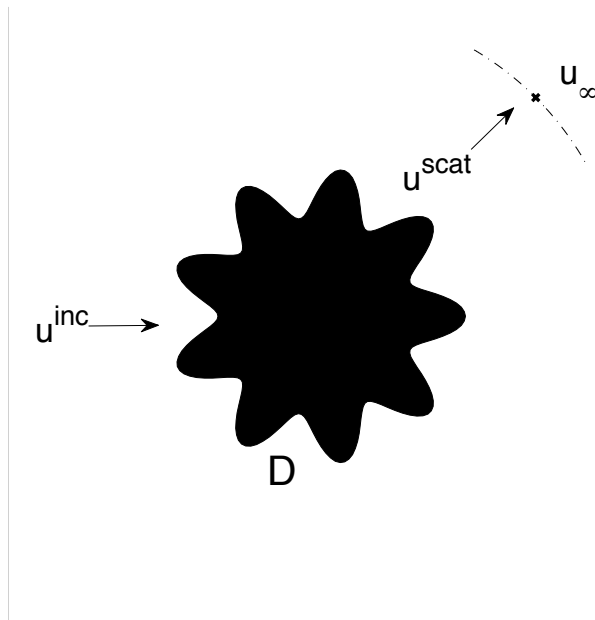


Figure 2.1: The direct scattering problem of finding the field scattered by an impenetrable obstacle.

We want to calculate the scattered acoustic field  $u^{\text{scat}}$  on  $\mathbb{R}^2 \setminus D$  of an impenetrable  $C^2$  sound-soft obstacle  $D$  due to an incident plane wave with direction  $d$ ,  $\|d\| = 1$ , and wavenumber  $k > 0$ . We consider the two dimensional problem. This problem can be deduced from a three dimensional infinite cylinder with cross-section  $D$  in the presence of an incident plane wave  $u^{\text{inc}}(x) = \exp(ikx \cdot d)$  perpendicular to the cylinder's axis. We seek to solve the following problem:

**Problem 4 Sound-Soft Acoustic Exterior Dirichlet Problem**

Find the solution  $u^{scat} \in C^2(\mathbb{R}^2 \setminus \overline{D}) \cap C(\mathbb{R}^2 \setminus D)$  to the problem

$$\begin{aligned} \Delta u^{scat}(x) + k^2 u^{scat}(x) &= 0 \quad \text{in } \mathbb{R}^2 \setminus \overline{D} \\ u^{scat}(x) &= f \quad \text{on } \partial D, \end{aligned}$$

with  $f = -u^{inc}$ , where  $u^{scat}(x)$  satisfies the Sommerfeld condition

$$\lim_{r \rightarrow \infty} r^{1/2} \left( \frac{\partial u^{scat}}{\partial r} - ik u^{scat} \right) = 0, \quad r = |x|.$$

Solving this problem, we can obtain the total field

$$u(x) = u^{inc}(x) + u^{scat}(x), \quad x \in \mathbb{R}^2 \setminus \overline{D}$$

such that  $u(x) = 0$  on  $\partial D$ .

We have the following results with respect to uniqueness of the solution of this problem.

**Theorem 2.1.1** *The Sound-Soft Exterior Dirichlet Problem has a unique solution, and the solution depends continuously on  $f$  in the maximum norm, i.e., small deviations in  $f$  in the maximum norm cause small deviations in  $u$  with respect to the maximum norm on  $\mathbb{R}^2 \setminus D$  and in all its derivatives with respect to the maximum norm on closed subsets of  $\mathbb{R}^2 \setminus D$ .*

**Proof:** The proof for the three-dimensional case is on page 48 of [3]. With appropriate changes in the fundamental solution, the radiation condition, and the spherical wave functions, it is possible to replicate the proof for the two-dimensional case.  $\square$

In this thesis, we use the integral equation approach to solve this problem. We define the acoustic layer potentials:

**Definition 2.1.1** *Given an integrable function  $\phi$ , we have the single-layer potential*

$$u(x) = \int_{\partial D} \Phi(x, y) \phi(y) \, ds(y), \quad x \in \mathbb{R} \setminus \partial D,$$

and the double-layer potential

$$v(x) = \int_{\partial D} \frac{\partial \Phi(x, y)}{\partial \nu(y)} \phi(y) \, ds(y), \quad x \in \mathbb{R} \setminus \partial D,$$

where

$$\Phi(x, y) = \frac{i}{4} H_0^1(k|x - y|)$$

is the fundamental solution of the Helmholtz equation in  $\mathbb{R}^2$ , and  $H_0^1(k|x - y|)$  is the 0<sup>th</sup> order Hankel function of the first kind, and  $\nu(y)$  is the outward-pointing vector normal to  $\partial D$  at the point  $y$ .

The acoustic layer potentials are solutions to the Helmholtz equation in  $D$  and in  $\mathbb{R}^2 \setminus D$ , and they satisfy the Sommerfeld radiation condition.

We have the following theorem regarding layer potentials, which can be found along with its proof in [35]:

**Theorem 2.1.2** *Let  $\partial D$  be of class  $C^2$  and let  $\phi$  be a continuous function. Then the single-layer potential  $u$  with density  $\phi$  is continuous throughout  $\mathbb{R}^2$  and*

$$\|u\|_{\infty, \mathbb{R}^2} \leq C_1 \|\phi\|_{\infty, \partial D}$$

for some constant  $C_1$  depending on  $\partial D$ . On the boundary we have

$$\begin{aligned} u(x) &= \int_{\partial D} \Phi(x, y) \phi(y) \, ds(y), \quad x \in \partial D, \\ \frac{\partial u_{\pm}}{\partial \nu}(x) &= \int_{\partial D} \Phi(x, y) \phi(y) \, ds(y) \mp \frac{1}{2} \phi(x), \quad x \in \partial D, \end{aligned}$$

where

$$\frac{\partial u_{\pm}}{\partial \nu}(x) := \lim_{h \rightarrow 0^+} \nu(x) \cdot \mathbf{grad} \, u(x \pm h\nu(x))$$

is to be understood in the sense of uniform convergence on  $\partial D$ , and where the integrals exist as improper integrals. The double-layer potential  $v$  with density  $\phi$  can be continuously extended from  $D$  to  $\bar{D}$  and from  $\mathbb{R}^2 \setminus \bar{D}$  to  $\mathbb{R}^2 \setminus D$  with limiting values

$$v_{\pm}(x) = \int_{\partial D} \frac{\partial \Phi(x, y)}{\partial \nu(y)} \phi(y) \, ds(y) \pm \frac{1}{2} \phi(x), \quad x \in \partial D,$$

where

$$v_{\pm}(x) := \lim_{h \rightarrow 0^+} v(x \pm h\nu(x))$$

and where the integral exists as an improper integral. Furthermore,

$$\begin{aligned} \|v\|_{\infty, \bar{D}} &\leq C_2 \|\phi\|_{\infty, \partial D}, \\ \|v\|_{\infty, \mathbb{R}^2 \setminus D} &\leq C_2 \|\phi\|_{\infty, \partial D} \end{aligned}$$

for some constant  $C_2$  depending on  $\partial D$ , and

$$\lim_{h \rightarrow 0^+} \left\{ \frac{\partial v}{\partial \nu}(x + h\nu(x)) - \frac{\partial v}{\partial \nu}(x - h\nu(x)) \right\} = 0, \quad x \in \partial D,$$

uniformly on  $\partial D$ .

Among the main tools in studying the Helmholtz equation are Green's integral theorems:

**Theorem 2.1.3 (Green's first theorem)** Let  $D$  be a bounded domain of class  $C^1$  and let  $\nu$  denote the unit normal vector to the boundary  $\partial D$  directed into the exterior of  $D$ . Then, for  $u \in C^1(\overline{D})$  and  $v \in C^2(\overline{D})$  we have

$$\int_D (u\Delta v + \mathbf{grad} u \cdot \mathbf{grad} v) \, dx = \int_{\partial D} u \frac{\partial v}{\partial \nu} \, ds.$$

**Theorem 2.1.4 (Green's second theorem)** Let  $D$  be a bounded domain of class  $C^1$  and let  $\nu$  denote the unit normal vector to the boundary  $\partial D$  directed into the exterior of  $D$ . Then, for  $u, v \in C^2(\overline{D})$  we have

$$\int_D (u\Delta v - v\Delta u) \, dx = \int_{\partial D} \left( u \frac{\partial v}{\partial \nu} - v \frac{\partial u}{\partial \nu} \right) \, ds.$$

**Theorem 2.1.5** Assume the bounded set  $D$  is the open complement of an unbounded domain of class  $C^2$  and let  $\nu$  denote the unit normal vector to the boundary  $\partial D$  directed into the exterior of  $D$ . Let  $u \in C^2(\mathbb{R}^2 \setminus \overline{D}) \cap C(\mathbb{R}^2 \setminus D)$  be a radiation solution to the Helmholtz equation

$$\Delta u(x) + k^2 u(x) = 0 \quad \text{in } \mathbb{R}^2 \setminus \overline{D}$$

that possesses a normal derivative on the boundary in the sense that the limit

$$\frac{\partial u}{\partial \nu}(x) = \lim_{h \rightarrow 0^+} \nu(x) \cdot \mathbf{grad} u(x - h\nu(x)), \quad x \in \partial D$$

exists uniformly on  $\partial D$ . Then we have Green's formula

$$u(x) = \int_{\partial D} \left[ u(y) \frac{\partial \Phi(x, y)}{\partial \nu(y)} - \frac{\partial u}{\partial \nu}(y) \Phi(x, y) \right] \, ds(y), \quad x \in D. \quad (1)$$

From Theorem 2.1.5, we deduce that the radiating solutions  $u$  to the Helmholtz equation automatically satisfy the Sommerfeld condition

$$\lim_{|x| \rightarrow \infty} |x|^{1/2} \left( \frac{\partial u}{\partial \nu} - iku \right)$$

uniformly for all directions.

Applying Green's Theorem to  $u^{\text{scat}}$  we get:

$$u^{\text{scat}}(x) = \int_{\partial D} \left[ u^{\text{scat}}(y) \frac{\partial \Phi(x, y)}{\partial \nu(y)} - \Phi(x, y) \frac{\partial u^{\text{scat}}(y)}{\partial \nu(y)} \right] \, ds(y), \quad x \in \mathbb{R}^2 \setminus \overline{D},$$

where  $\nu$  is the outward-pointing unit vector normal to  $\partial D$ . Applying Green's Second Theorem to the entire solution  $u^{\text{inc}}$  we get:

$$0 = \int_{\partial D} \left\{ u^{\text{inc}}(y) \frac{\partial \Phi(x, y)}{\partial \nu(y)} - \Phi(x, y) \frac{\partial u^{\text{inc}}(y)}{\partial \nu(y)} \right\} \, ds(y), \quad x \in \mathbb{R}^2 \setminus \overline{D}.$$

Putting these two equations together and using the homogeneous Dirichlet boundary condition, we obtain:

$$u^{\text{inc}}(x) = \int_{\partial D} \Phi(x, y) \frac{\partial u}{\partial \nu}(y) \, ds(y), \quad x \in \partial \bar{D}. \quad (2)$$

We define the single layer operator  $S_{\partial D} : C(\partial D) \rightarrow C(\partial D)$  as follows:

$$S_{\partial D} \psi(x) := \frac{i}{4} \int_{\partial D} H_0^{(1)}(k|x-y|) \psi(y) \, ds(y).$$

**Theorem 2.1.6** *The integral operator  $S_{\partial D} : C(\partial D) \rightarrow C(\partial D)$ , where  $S_{\partial D}$  maps  $C(\partial D)$  into  $C^{0,\alpha}(\partial D)$  and  $C^{0,\alpha}(\partial D)$  into  $C^{1,\alpha}(\partial D)$ , is a self-adjoint operator and is a compact operator in  $C(\partial D)$  and  $C^{0,\alpha}(\partial D)$  for  $0 < \alpha < 1$ .*

**Proof:** The proof is on page 62 of [35]. □

Now, if we use a parameterization for  $\partial D$  as  $x : [0, 2\pi] \rightarrow \mathbb{R}^2$ , the operator  $S_{\partial D}$  becomes

$$S_{\partial D} \psi(t) := \frac{i}{4} \int_0^{2\pi} H_0^{(1)}(k|x(t) - x(\tau)|) \psi(\tau) \, d\tau,$$

where we write for the sake of simplicity  $\psi(\tau) := \psi(x(\tau))|x'(\tau)|$ .

We may thus rewrite (2) as

$$u^{\text{inc}}(x(t)) = \left( S_{\partial D} \frac{\partial u}{\partial \nu} \right) (x(t)), \quad \forall x(t) \in \partial D. \quad (3)$$

This is a boundary integral equation of the first kind, which allows us to find  $\frac{\partial u}{\partial \nu}$  using only the boundary condition  $u(x) = 0$  for  $x \in \partial D$ . We have the following theorem concerning the solution of Equation (3).

**Theorem 2.1.7** *The integral equation of the first kind for the Dirichlet problem*

$$u^{\text{inc}}(x(t)) = \left( S_{\partial D} \frac{\partial u}{\partial \nu} \right) (x(t)), \quad \forall x(t) \in \partial D$$

*has a unique solution provided  $k^2$  is not an interior Dirichlet eigenvalue. If  $k^2$  is an eigenvalue, then the solution exists but may not be unique.*

**Proof:** The proof of a general theorem for first kind integral equations is on page 88 of [35]. It suffices to apply this to the left hand side  $u^{\text{inc}}(x)$ . □

**Remark 2.1.1** *To avoid the problem of non-uniqueness of the solution when  $k^2$  is an eigenvalue of the interior Dirichlet problem, Leis [36] and Brakhage [37] independently presented a combined layer approach. We do not present this approach in this thesis. The likelihood that a wavenumber is exactly an eigenvalue for the interior Dirichlet problem is very small. However, all of the techniques presented in this thesis can be extended to be used with the combined layer approach. We are not going to address this approach in this thesis. For more detail in the combined layer approach, we direct the reader to the book of Colton and Kress [3].*

Later in this thesis, we will be interested in solving inverse problems that have as given data the far field pattern of the object  $D$ . We define the far field pattern or scattering amplitude in the following theorem.

**Theorem 2.1.8** *Every radiating solution  $u$  to the Helmholtz equation has the asymptotic behavior of an outgoing spherical wave*

$$u(x) = \frac{e^{ik|x|}}{|x|^{1/2}} \left\{ u_\infty(\hat{x}) + \mathcal{O}\left(\frac{1}{|x|^{3/2}}\right) \right\}, \quad |x| \rightarrow \infty,$$

*uniformly in all directions  $\hat{x} = x/|x|$  where the function  $u_\infty$  defined on the unit circle  $\Omega$  is known as the far field pattern of  $u$ . Under the assumptions of Theorem (2.1.5), we have*

$$u_\infty(\hat{x}) = \frac{e^{-i\frac{\pi}{4}}}{\sqrt{8\pi k}} \int_{\partial D} \left[ u(y) \frac{\partial e^{-ik\hat{x}\cdot y}}{\partial \nu(y)} - \frac{\partial u}{\partial \nu}(y) e^{-ik\hat{x}\cdot y} \right] ds(y), \quad \hat{x} \in \Omega.$$

**Proof:** We use (1), the asymptotic behavior of the Hankel function as  $t \rightarrow \infty$

$$H_n^{(1)}(t) = \sqrt{\frac{2}{\pi t}} e^{\pm i(t - \frac{n\pi}{2} - \frac{\pi}{4})} \left\{ 1 + \mathcal{O}\left(\frac{1}{t}\right) \right\},$$

and the approximation

$$|x - y| = |x| - \hat{x} \cdot y + \mathcal{O}\left(\frac{1}{|x|}\right).$$

For details, see page 21 of [3]. □

Using the homogeneous Dirichlet boundary condition again, we obtain:

$$u_\infty(\hat{x}) = -\frac{e^{i\pi/4}}{\sqrt{8\pi k}} \int_{\partial D} \frac{\partial u}{\partial \nu}(y) e^{-ik\hat{x}\cdot(y)} ds(y). \quad (4)$$

Using the parameterization  $x(t)$  of  $\partial D$  again, we obtain

$$u_\infty(\hat{x}) = -\frac{e^{i\pi/4}}{\sqrt{8\pi k}} \int_0^{2\pi} \frac{\partial u}{\partial \nu}(y(\tau)) e^{-ik\hat{x}\cdot(y(\tau))} |y'(\tau)| d\tau. \quad (5)$$

We define the operator  $S_{\partial D, \infty} : L^2([0, 2\pi]) \rightarrow L^2([0, 2\pi])$  by

$$(S_{\partial D, \infty} \psi)(\hat{x}) = -\frac{e^{i\pi/4}}{\sqrt{8\pi k}} \int_0^{2\pi} e^{-ik\hat{x}\cdot y(\tau)} \psi(\tau) d\tau,$$

where  $\psi(\tau) = \frac{\partial u}{\partial \nu}(y(\tau))|y'(\tau)|$ .

In short, we write (5) as

$$u_\infty(\hat{x}) = \left( S_{\partial D, \infty} \frac{\partial u}{\partial \nu} \right) (\hat{x}), \quad \forall \hat{x} \in \Omega, \quad (6)$$

and this equation provides us with the far field pattern of  $D$ .

It is worth noting that the kernel of the operator is analytic. If we were to solve Equation (6) to obtain the normal derivative  $\frac{\partial u}{\partial \nu}$  of the field in the presence of the object  $D$  from the far field pattern data provided, this problem would be ill-posed.

### 2.1.2 Direct scattering problem with multiple objects

We briefly present a way of adapting the previous procedure to obtain the normal derivative of the field and the far field pattern of a configuration with multiple objects.

Consider our scatterer domain  $D$  as the union of  $N_D$  many scatterers  $D_s$ ,  $s \in \{1, \dots, N_D\}$  (that is,  $D = \bigcup_{s=1}^{N_D} D_s$ ), where the  $D_s$  are connected sets and  $D_s \cap D_w = \emptyset$  for  $s \neq w$ . Our equations for the direct problem become:

$$\begin{aligned} u^{\text{inc}}(x) &= \int_{\partial D} \Phi(x, y) \frac{\partial u(y)}{\partial \nu(y)} \, ds(y) \\ &= \sum_{s=1}^{N_D} \int_{\partial D_s} \Phi(x, y) \frac{\partial u(y)}{\partial \nu(y)} \, ds(y). \end{aligned} \quad (7)$$

Let us define the operators

$$\begin{aligned} (S_{\partial D_s, \partial D_w} \phi)(x^{(w)}) &= \int_{\partial D_s} \Phi(x^{(w)}, y) \phi(y) \, ds(y) \\ (S_{\partial D_s, \partial D_s} \phi)(x^{(s)}) &= \int_{\partial D_s} \Phi(x^{(s)}, y) \phi(y) \, ds(y), \end{aligned}$$

where  $x^{(s)} \in \partial D_s$  and  $x^{(w)} \in \partial D_w$ . Choosing  $x = x^{(w)} \in \partial D_w$ , (7) becomes

$$u^{\text{inc}}(x^{(w)}) = \sum_{s=1}^{N_D} \left[ \left( S_{\partial D_s, \partial D_w} \frac{\partial u}{\partial \nu} \right) (x^{(w)}) \right]. \quad (8)$$

We use Equation (8) to obtain the value of the normal derivative of the field on the boundary of the objects  $D_s$ . Using the normal derivative, we find the far field for the configuration using the operators:

$$(S_{\partial D_s, \infty} \phi)(\hat{x}) = \frac{e^{i\pi/4}}{\sqrt{8\pi k}} \int_{\partial D_s} e^{-ik\hat{x} \cdot y} \phi(y) \, ds(y),$$

for each domain  $D_s$ .

Finally, to find the far field pattern at  $\hat{x}$  we must solve:

$$u_\infty(\hat{x}) = \sum_{s=1}^{N_D} \left[ \left( S_{\partial D_s, \infty} \frac{\partial u}{\partial \nu} \right) (\hat{x}) \right]. \quad (9)$$

## 2.2 Inverse scattering problem

### 2.2.1 Introduction to the inverse scattering problem

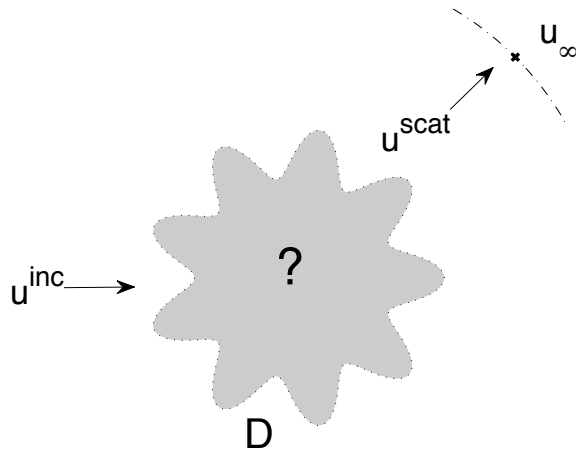


Figure 2.2: The inverse scattering problem of reconstructing an impenetrable object from measures of the far field pattern.

In the previous section we introduced the direct acoustic scattering problem for an impenetrable object with Dirichlet boundary condition, where we find the scattered wave and its behavior at long distances from the object (*i.e.*, its far field) given information on the boundary of the scatterer and the nature of the boundary condition. In this section, we focus on the solution of the inverse scattering problem for impenetrable objects. In this problem, we have the far field pattern of an impenetrable object and we find properties of the nature of the object—more specifically, we are interested in its shape.

There are several different iterative methods that can be used to obtain approximate solutions to this inverse problem, and these methods can be characterized in the following ways:

- **Methods for recovering the object from a far field pattern generated by only one incoming wave**
  - One group of methods for iteratively solving the inverse problem in this scenario divides the problem into two parts: an ill-posed linear equation, which is used to find the scattered field using the far field pattern data, and a well-posed non-linear part to find the boundary using the boundary condition, see [38–41].
  - Alternative approaches which avoid solving the direct problem have been considered in [42] and [43].
- **Methods for recovering the object from a far field pattern generated by multiple incoming waves**
  - Some methods for solving this problem include the linear sampling method [9], the point-source method [41], the factorization method [44], and the probe method [45].

We are interested in solving the inverse problem where we know the kind of boundary condition of the object—in our case, the Dirichlet condition—and measurements of the far field pattern (its real and complex parts) generated when the incoming incident waves—which we suppose to have one fixed incidence direction at one or several frequencies—deflect from the object  $D$ .

An inverse problem of this type is ill-posed and nonlinear. In the next section, we present the concept of ill-posedness and present the techniques to solve this problem.

## 2.2.2 Ill-posed problems and regularization

In mathematical physics, Hadamard [46] postulated three main requirements in order for a problem to be considered well-posed: the existence of the solution, the uniqueness of the solution, and the continuous dependence of the solution on the input data. The continuity requirement ensures that small errors in the data will yield only commensurately small errors in the solution. The following is a more rigorous definition of posedness in the sense of Hadamard.

**Definition 2.2.1** *Let  $A : X \supset U \rightarrow V \subset Y$  be an operator from a subset  $U$  of a normed space  $X$  into a subset  $V$  of a normed space  $Y$ . The equation*

$$A\phi = f$$

*is called well-posed or properly posed if  $A : U \rightarrow V$  is bijective and the inverse operator  $A^{-1} : V \rightarrow U$  is continuous. Otherwise, the equation is called ill-posed or improperly posed.*

The ill-posedness of an equation influences its numerical treatment. To produce stable solutions of an ill-posed problem we use so-called regularization methods.

**Definition 2.2.2** *Let  $X$  and  $Y$  be normed spaces and let  $A : X \rightarrow Y$  be an injective bounded linear operator. Then a family of bounded linear operators  $R_\lambda : Y \rightarrow X$ ,  $\lambda > 0$ , with the property of pointwise convergence*

$$\lim_{\lambda \rightarrow 0} R_\lambda A\psi = \psi \quad (10)$$

*for all  $\psi \in X$  is called a regularization scheme for the operator  $A$ . The parameter  $\lambda$  is called the regularization parameter.*

The regularization scheme allows the solution  $\psi$  of  $A\psi = f$  to be approximated by the regularized solution

$$\psi_\lambda^\delta := R_\lambda f^\delta.$$

We have for the approximation error,

$$\psi_\lambda^\delta - \psi = R_\lambda f^\delta - R_\lambda f + R_\lambda A\psi - \psi.$$

By the triangle inequality, we obtain the estimate

$$\|\psi_\lambda^\delta - \psi\| \leq \delta \|R_\lambda\| + \|R_\lambda A\psi - \psi\|, \quad (11)$$

where  $\delta > 0$  is a constant such that

$$\|f - f^\delta\| \leq \delta.$$

In practice, we will use an *a posteriori* choice of the regularization parameter  $\lambda$  based on [47].

We will use Tikhonov's regularization scheme [48; 49], which can also be understood as a penalized residual minimization.

**Theorem 2.2.1** *Let  $A : X \rightarrow Y$  be a compact linear operator. Then for each  $\lambda > 0$ , the operator  $(\lambda I + A^*A) : X \rightarrow X$  is bijective and has a bounded inverse. Furthermore, if  $A$  is injective then*

$$R_\lambda := (\lambda I + A^*A)^{-1} A^*$$

*describes a regularization scheme with  $\|R_\lambda\| \leq 1/2\sqrt{\lambda}$ .*

**Proof:** The proof can be found on page 97 of [3]. □

We have the following theorem relating Tikhonov regularization to the penalized residual minimization.

**Theorem 2.2.2** *Let  $A : X \rightarrow Y$  be a compact linear operator and let  $\lambda > 0$ . Then for each  $f \in Y$ , there exists a unique  $\psi_\lambda$  such that*

$$\|A\psi_\lambda - f\|^2 + \lambda\|\psi_\lambda\|^2 = \inf_{\psi \in X} \{\|A\psi - f\|^2 + \lambda\|\psi\|^2\}.$$

*The minimizer  $\psi_\lambda$  is given by the unique solution of*

$$(\lambda I + A^*A)\psi_\lambda = A^*f \tag{12}$$

*and depends continuously on  $f$ .*

**Proof:** The proof can be found on page 98 of [3]. □

### 2.2.3 Newton method for a single frequency

We consider in this section the case when we have an incident wave with direction  $d$  and wavenumber  $k$ . We have the problem

**Problem 1** *Given the far field pattern generated by the scattering of the incident plane waves  $u^{inc}(x) = e^{ikx \cdot d}$  with direction  $d$  and wavenumber  $k$  off of an unknown object  $D$  with homogeneous Dirichlet boundary condition, reconstruct the shape of the object  $D$ .*

The solution of the direct Dirichlet scattering problem with a fixed incident plane wave  $u^{inc}$  defines an operator  $F : \mathbb{X} \rightarrow L^2(\Omega)$  that maps the boundary curve  $\partial D \in \mathbb{X}$  of the scatterer, where  $\mathbb{X}$  is a selected space of curves, to the far field pattern  $u_\infty$  of the scattered wave.

Applying the operator  $F$  to the curve  $\partial D$  is equivalent to solving the following equation for  $\frac{\partial u}{\partial \nu}$ :

$$S_{\partial D} \frac{\partial u}{\partial \nu} = u^{inc},$$

and applying the operator  $S_{\partial D, \infty}$  to the solution  $\frac{\partial u}{\partial \nu}$  to find the far field pattern  $u_\infty$  as in the equation

$$u_\infty = S_{\partial D, \infty} \frac{\partial u}{\partial \nu}.$$

In terms of this operator, given a far field pattern  $u_\infty$ , the inverse problem consists of solving the equation

$$F(\partial D) = u_\infty, \tag{13}$$

for the unknown surface  $\partial D$ .

Regarding this problem, when we have only one incident wave with wavenumber  $k$ , we have the following uniqueness theorem related to the inverse Dirichlet scattering problem, which can be found with its proof in [50]. The theorem tells us that the object can be uniquely determined by the far field pattern generated by an incident plane wave, given that the size of the object is known.

**Theorem 2.2.3** *Let  $D_1$  and  $D_2$  be two impenetrable objects which are contained in a ball of radius  $R$ , such that  $R < C/k$ , where  $C \approx 2.40482556$  is the smallest positive root of the Bessel function  $J_0$  [51], and assume that the far field patterns coincide for one incident plane wave with wavenumber  $k$ . Then  $D_1 = D_2$ .*

So far, we have not defined the solution space for  $\partial D$ . We consider the solution space  $\mathbb{X}$  to be the space of starlike domains with respect to the origin, *i.e.*, we assume that  $\partial D$  is represented by a parameterization  $x$  of the form

$$x(\hat{x}) = x_r(\hat{x})\hat{x}, \quad \hat{x} \in \Omega, \quad (14)$$

where the radius function  $x_r$  is positive and is in  $C^1(\Omega)$ . Considering  $\hat{x}(t) = (\cos(t), \sin(t))$  for  $t \in [0, 2\pi]$ , we may slightly abuse notation by writing for short  $x(t) = x_r(t)(\cos(t), \sin(t))$ .

We thus define the solution space  $\mathbb{X}$  as

$$\mathbb{X} = \left\{ x : [0, 2\pi] \rightarrow \mathbb{R}^2 \mid x(t) = x_r(t)(\cos(t), \sin(t)), \ x_r(t) > 0, \ x_r(0) = x_r(2\pi), \right. \\ \left. x'_r(0) = x'_r(2\pi) \text{ and } x_r(t) \in C^1(\Omega) \right\}.$$

Using (13) in (14), we obtain the mapping  $\hat{F} : C^1(\Omega) \rightarrow L^2(\Omega)$ , defined by

$$\hat{F}(x_r) = u_\infty. \quad (15)$$

Note that  $\hat{F}(x_r(\hat{x})) = F(x_r(\hat{x})\hat{x}) = F(x)$ .

The main questions that we wish to address are those of continuity, differentiability and compactness of the operator  $F$ . With respect to the continuity and differentiability, we have the following theorems:

**Theorem 2.2.4** *For a fixed incident plane wave  $u^{inc}$ , the operator  $\hat{F} : C^1(\Omega) \rightarrow u_\infty$  that maps the boundary  $\partial D$  to the far field pattern  $u_\infty$  of the scattered wave  $u^{scat}$  is continuous from  $C^1(\Omega)$  to  $L^2(\Omega)$ .*

**Proof:** See page 115 of [3]. □

Due to the non-linearity of the problem, we need to study the differentiability of the operator  $F$ . Next, we define the concept of the Fréchet derivative of an operator.

**Definition 2.2.3** Let  $X$  and  $Y$  be normed spaces, and  $U \subset X$  be an open subset of  $X$ . A mapping  $A : X \rightarrow Y$  is called Fréchet differentiable at  $\psi \in U$  if there exists a bounded linear operator  $A' : X \rightarrow Y$  such that

$$\|A(\psi + h) - A(\psi) - A'(\psi)h\| = o(\|h\|)$$

uniformly as  $\|h\| \rightarrow 0$ .  $A'(\psi)$  is called the Fréchet derivative of  $A$  at  $\psi$ .  $A$  is called Fréchet differentiable if it is Fréchet differentiable at every point  $\psi \in U$ .

Regarding the Fréchet derivative of the mapping  $\hat{F}$ , we have the following theorems:

**Theorem 2.2.5** The far field mapping  $\hat{F} : C^1(\Omega) \rightarrow L^2(\Omega)$  is Fréchet differentiable from  $C^2(\Omega)$  to  $L^2(\Omega)$ . The derivative  $\hat{F}'_{x_r} : C^2(\Omega) \rightarrow L^2(\Omega)$  is given by

$$\hat{F}'_{x_r} h = v_\infty, \tag{16}$$

where  $v_\infty$  denotes the far field pattern of the solution  $v$  to the Helmholtz equation in  $\mathbb{R}^2 \setminus \bar{D}$  satisfying the Sommerfeld radiation condition and the boundary condition

$$v = -\nu \cdot x_h \frac{\partial u}{\partial \nu} \quad \text{on} \quad \partial D,$$

where  $x_h = h(\hat{x})\hat{x}$  and  $u$  is the solution of the direct problem used to obtain  $u_\infty$ .

**Proof:** See the paper of Kirsch [52]. □

**Theorem 2.2.6** The linear operator  $\hat{F}'_{x_r}$  is injective in  $C^2(\Omega)$ .

**Proof:** See page 129 of [3]. □

In addition, the operator  $\hat{F}$  is ill-posed according to the next theorem, which is proven on page 121 of [3].

**Theorem 2.2.7** The mapping  $\hat{F} : C^1(\Omega) \rightarrow L^2(\Omega)$  is locally compact from  $C^1(\Omega)$  into  $L^2(\Omega)$ ; that is, for each  $x_r \in C^1(\Omega)$  there exists a neighborhood  $U$  of  $x_r$  such that  $\hat{F} : U \rightarrow L^2(\Omega)$  is compact.

The next theorem of [3] states that the Fréchet derivative of an ill-posed nonlinear operator inherits the operator's ill-posedness.

**Theorem 2.2.8** Let  $A : U \subset X \rightarrow Y$  be a compact operator from an open subset  $U$  of a normed space  $X$  into a Banach space  $Y$  and assume  $A$  to be Fréchet differentiable at  $\psi \in U$ . Then the derivative  $A'(\psi)$  is compact.

**Proof:** For the proof, see page 102 of [3]. □

Using the last theorem with  $\hat{F}$  as  $A$ ,  $C^1(\Omega)$  as  $X$  and  $L^2(\Omega)$  as  $Y$ , and the fact that  $\hat{F}$  is completely continuous by Theorem 2.2.3, we have that the operator  $\hat{F}'_{x_r}$  inherits the ill-posedness of the operator  $\hat{F}$ .

These theorems are the theoretical foundation for the application of Newton's method and related methods of solving the inverse scattering problem. In Newton's method, given the far field pattern  $u_\infty$  of an object  $D$ , instead of solving the ill-posed nonlinear equation (15), we solve for  $h$ , its linearized version, using the equation

$$\hat{F}(x_r) + \hat{F}'_{x_r} h = u_\infty. \quad (17)$$

With the solution  $h$ , we update the boundary condition according to  $x_r := x_r + h$ . The idea behind Newton's method is to iterate this procedure until we reach a stopping criterion. The question of uniqueness of the solution of (17) is answered by the injectivity of  $\hat{F}'_{x_r}$  [3]. With respect to the ill-posedness, we have to apply a regularization technique.

**Algorithm 2.2.1** *Newton's method for the inverse scattering problem*

1. Chose an initial guess  $x_r^{(0)}$  and set  $j = 0$ .
2. Repeat until a stopping criterion is reached
  - (a) Solve (17) for  $h$ ;
  - (b) Update  $x_r^{(j+1)} := x_r^{(j)} + h$ ;
  - (c) Set  $j=j+1$ .

Figure 2.3: Summary of Newton's method for solving the inverse scattering problem.

We look for the functions  $x_r(t)$  in two types of spaces  $\mathbb{X}_{N_r}$ :

- The space of trigonometric polynomials

$$\mathbb{X}_{N_r} = \left\{ x_r : [0, 2\pi] \rightarrow \mathbb{R}^+ \mid x_r(t) = a_0 + \sum_{m=1}^{N_r} (a_m \cos(mt) + b_m \sin(mt)), a_0, a_m, b_m \in \mathbb{R}, \right. \\ \left. m = 1, \dots, N_r \right\},$$

where  $2N_r + 1$  is the number of degrees of freedom of the polynomial  $x_r(t)$ ; and

- The space of B-splines

$$\mathbb{X}_{N_r} = \left\{ x_r : [0, 2\pi] \rightarrow \mathbb{R}^+ \mid x_r(0) = x_r(2\pi), \quad x_r(t) = \sum_{m=1}^{N_r} c_m N_m^q(t), c_m \in \mathbb{R}, \right. \\ \left. m = 1, \dots, N_r \right\},$$

where  $N_r$  is the number of degrees of freedom of the polynomial  $x_r(t)$ , and  $N_m^q$  is the B-spline function of order  $q$  relative to the coefficient  $c_m$ . For details on the implementation of B-splines we refer the reader to [53].

Each choice for the space  $\mathbb{X}_{N_r}$  has its advantages. The implementation of trigonometric functions is simpler and faster than using B-splines. The advantage of B-splines is that they are local functions, while the trigonometric functions are global, and so with B-splines, we may choose to update the function only locally, instead of globally. We present examples using both implementations.

For practical computations, we choose  $h$  in the solution space  $\mathbb{X}_{N_r}$ , and write it

$$h = \sum_{j=1}^N w_j W_j, \quad (18)$$

where  $\{W_1, \dots, W_{N_r}\}$  is a basis for  $\mathbb{X}_{N_r}$  and  $w_1, \dots, w_{N_r}$  are the coordinates of  $h$  with respect to this basis. Using (18) in (17), we obtain

$$\sum_{j=1}^{N_r} w_j (\hat{F}'_{x_r} W_j) = u_\infty - \hat{F}(x_r).$$

For each basis function  $W_j$ ,  $j = 1, \dots, N_r$ , we must solve the direct problem for  $(\hat{F}'_{x_r} W_j)$ , as in Theorem 2.2.3. According to Theorem 2.2.3, in order to obtain the value of  $v_\infty = (\hat{F}'_{x_r} W_j)$ , we must find  $v$  that solves the Helmholtz equation in  $\mathbb{R}^2 \setminus \overline{D}$ , and satisfies the Sommerfeld radiation condition together with the boundary condition

$$v = -\nu \cdot W_j \frac{\partial u}{\partial \nu} \quad \text{on } \partial D.$$

We can use the integral equation approach presented in the last section to find the value of  $v_\infty$ . First, we solve for  $\frac{\partial v}{\partial \nu}$  the equation

$$\int_{\partial D} \Phi(x, y) \frac{\partial v}{\partial \nu}(y) ds(y) = e^{ikx \cdot d} + \nu(x) \cdot W_j \frac{\partial u}{\partial \nu}(x) - \int_{\partial D} \frac{\partial \Phi(x, y)}{\partial \nu(y)} \nu \cdot W_j \frac{\partial u}{\partial \nu}(y) ds(y), \quad (19)$$

where  $x \in \partial D$ .

After obtaining the solution  $\frac{\partial v}{\partial \nu}$  to Equation (19), we calculate the far field pattern  $v_\infty$  using the asymptotic behavior of the fundamental solution  $\Phi(x, y)$

$$v_\infty(\hat{x}) = \int_{\partial D} \left\{ -\frac{\partial e^{-ik\hat{x}\cdot y}}{\partial \nu(y)} \nu \cdot W_j \frac{\partial u}{\partial \nu}(y) - e^{-ik\hat{x}\cdot y} \frac{\partial v}{\partial \nu}(y) \right\} ds(y). \quad (20)$$

For each basis function  $W_j$  of the space  $\mathbb{X}_{N_r}$ ,  $j = 1, \dots, N_r$ , we need to solve a direct scattering problem. In total, for each step of the Newton method, we solve  $N_r$  direct problems. This is computationally expensive. Because of the computational cost, in this thesis we do not use Newton's method. It was introduced only because of its relation to the numerical method that we use in our problem.

## 2.2.4 The variation of the Method of Johansson and Sleeman–Method B

In the last section we showed the approach of Newton's method as seen in [3]. Since Newton's method is computationally expensive, we instead use the algorithm introduced independently in [16] and [54] (and later extended in [18]) to recover the object. This algorithm is based on a two-step iterative procedure directly related to Equations (3) and (6).

We start with a motivation for the method. Considering the process of obtaining the far field pattern from the domain  $\partial D$ , we can write the operator  $\hat{F} : C^1(\Omega) \rightarrow L^2(\Omega)$  as

$$\hat{F}(x_r) = S_{x_r, \infty} \frac{\partial u}{\partial \nu}, \quad (21)$$

where  $x(t) = x_r(t)(\cos(t), \sin(t))$  is the parameterization of the domain  $\partial D$ , the operator  $S_{x_r, \infty}$  is the far field operator for this parameterization, and  $\frac{\partial u}{\partial \nu}$  is the solution of

$$S_{x_r} \frac{\partial u}{\partial \nu} = u^{\text{inc}} \quad \text{on} \quad \partial D,$$

where  $S_{x_r}$  is the acoustic single-layer potential for the same parameterization  $x(t)$  of  $\partial D$ . We can write

$$\frac{\partial u}{\partial \nu} = S_{x_r}^{-1} u^{\text{inc}} \quad \text{on} \quad \partial D,$$

where the operator  $S_{x_r}^{-1}$  is the inverse operator of  $S_{x_r}$ .

Finally, we have the operator  $\hat{F}$  as

$$\hat{F}(x_r) = S_{x_r, \infty} (S_{x_r}^{-1} u^{\text{inc}}) \quad \text{on} \quad \partial D. \quad (22)$$

In the Newton method, we calculate the Fréchet derivative of the operator  $\hat{F}$  with respect to the domain in Theorem 2.2.3. An alternative way to write (16) in Theorem 2.2.5 is:

$$\hat{F}'_{x_r} h = S'_{x_r, \infty}(S_{x_r}^{-1} u^{\text{inc}})h + S_{x_r, \infty}(S_{x_r}^{-1} u^{\text{inc}})'h. \quad (23)$$

Assuming that  $\frac{\partial u}{\partial \nu} = S_{x_r}^{-1} u^{\text{inc}}$  depends very weakly on the change of the curve  $x_r$ , *i.e.*,

$$\left(\frac{\partial u}{\partial \nu}\right)' = (S_{x_r}^{-1} u^{\text{inc}})' \approx 0,$$

we discard the second term of (23) and obtain an approximation given by

$$\hat{F}'_{x_r} h \approx S'_{x_r, \infty} \left(\frac{\partial u}{\partial \nu}\right) h.$$

This approach is computationally less expensive than each step of Newton's method.

It is important to emphasize the fact that in this method, we do not need to solve several direct problems in each step. On the other hand, instead of linearizing the entire operator  $F$ , we only linearize the part regarding the far field pattern—that is, the operator  $S_{x_r, \infty}$ . This method can be considered a quasi-Newton method for approximating the Fréchet derivative of the operator  $\hat{F}$  by  $S'_{x_r, \infty}$ . After showing the motivation, we now present Johansson and Sleeman's method in detail.

The iterative method introduced by Johansson and Sleeman for solving the inverse scattering problem can be described in the following way:

1. Choose an initial guess  $x^{(0)}(t) = x_r^{(0)}(t)(\cos(t), \sin(t))$  in  $\mathbb{X}$ .
2. Repeat until the stopping criterion is reached:
  - (a) Use the two-step procedure with the parameterization  $x^{(j)}(t) = x_r^{(j)}(t)(\cos(t), \sin(t))$ ,  $j \in \{1, 2, \dots\}$ , to obtain a new approximation of the domain  $x^{(j+1)}$  updating  $x^{(j)}$ .

We present the two-step procedure that is used in the method.

1. Suppose we have a parameterization  $x^{(j)}$  approximating the object. We solve for  $\psi(x^{(j)}) = \frac{\partial u}{\partial \nu}(x^{(j)})|(x^{(j)})'|$  the integral equation of the first kind

$$S_{x_r^{(j)}} \psi = u^{\text{inc}} \quad \text{on} \quad \partial D^{(j)}, \quad (24)$$

where  $S_{x_r^{(j)}}$  is the acoustic single-layer operator for the domain  $\partial D^{(j)}$  with parameterization  $x^{(j)}(t) = x_r^{(j)}(t)(\cos(t), \sin(t))$ , for  $t \in [0, 2\pi]$ .

2. In the next step, we define the residual function

$$r(x_r) = S_{x_r, \infty} \psi - u_\infty.$$

We define the functional

$$f(x_r) = \frac{1}{2} \|r(x_r)\|_{L^2(\Omega)}^2$$

and solve the following minimization problem:

$$\min_{x_r \in \mathbb{X}_{N_r}} f(x_r). \quad (25)$$

This problem is nonlinear, so instead of minimizing the function  $f(x_r)$ , we minimize the first order approximation around  $x_r^{(j)}$ ,

$$M^{(j)}(x_r) = r(x_r^{(j)}) + J(x_r^{(j)})(x_r - x_r^{(j)}),$$

where  $M^{(j)} : C^1(\Omega) \rightarrow L^2(\Omega)$  is the first-order model approximation of  $f$ , and  $J(x_r^{(j)}) = \left( S_{x_r^{(j)}, \infty} \frac{\partial u}{\partial \nu} \right)'$  is the Fréchet derivative of  $r(x_r)$  (actually of  $S_{x_r}$ ) at the domain parameterization  $x^{(j)}$  given in the next theorem, which can be found together with its proof in [52].

**Theorem 2.2.9** *Given a density  $\psi(\tau)$ , the Fréchet derivative of the operator  $S'_{x^{(j)}, \infty} : \mathbb{X} \rightarrow L^2[0, 2\pi]$  is the operator  $\left[ \left( S_{x^{(j)}, \infty} \frac{\partial u}{\partial \nu} \right)' h \right] (\hat{x})$  defined as*

$$\left[ \left( S_{x_r^{(j)}, \infty} \frac{\partial u}{\partial \nu} \right)' h \right] (\hat{x}) = ik \frac{e^{i\pi/4}}{\sqrt{8\pi k}} \int_0^{2\pi} e^{-ik\hat{x} \cdot x^{(j)}(\tau)} \psi(\tau) \hat{x} \cdot h(\tau) d\tau, \quad (26)$$

with  $\psi(\tau) = \frac{\partial u}{\partial \nu}(x^{(j)}(\tau)) \left| x^{(j)'(\tau)} \right|$  and  $h \in \mathbb{X}$ , where

$$\mathbb{X} = \{h(t) = h_r(t)(\cos(t), \sin(t)) \mid h_r(t) > 0 \text{ and } h_r(t) \in \mathbb{X}_{N_r}\},$$

the space of star-shaped parameterizations of the domain with positive radius function.

Note that in the derivative (26), we consider that the density function  $\psi$  is given by solving (24), and we do not consider its dependence on the domain.

Instead of solving problem (25), we solve

$$\min_{x_r \in \mathbb{X}_{N_r}} \frac{1}{2} \|M^{(j)}(x_r)\|_{L^2(\Omega)}^2 \quad (27)$$

using an iterative method. At each step we solve an equation of the form

$$x_r^{(j+1)} = x_r^{(j)} - \left( J(x_r^{(j)}) * J(x_r^{(j)}) \right)^{-1} J(x_r^{(j)}) * r(x_r^{(j)}). \quad (28)$$

Due to the ill-posedness of the operator  $S'_{x_r^{(j)}, \infty}$ , we must use a regularization technique such as Tikhonov regularization to solve Equation (25). Instead of solving Equation (25), we define the Tikhonov functional  $\tilde{f}(x_r) = \frac{1}{2} \|M^{(j)}(x_r^{(j)})\|_{L^2(\Omega)}^2 + \frac{1}{2} \lambda^{(j)} \|x - x^{(j)}\|_{H^1(\Omega)}^2$ , where  $x^{(j)}(t) = x_r^{(j)}(t)(\cos(t), \sin(t))$ ,  $x(t) = x_r(t)(\cos(t), \sin(t))$ , and we solve the following problem:

$$\min_{x_r \in \mathbb{X}_{N_r}} \tilde{f}(x_r), \quad (29)$$

where  $\lambda^{(j)} > 0$  is a regularization parameter chosen such that the problem is not ill-posed. We will discuss the regularization parameter further in Section 2.2.5.

To solve (29) we use a Gauss-Newton method and obtain the update for each step

$$x_r^{(j+1)} = x_r^{(j)} - (J(x_r^{(j)})^* J(x_r^{(j)}) + \lambda^{(j)} I^p)^{-1} J(x_r^{(j)})^* r(x_r^{(j)}), \quad (30)$$

where  $I^p$  is the identity operator for the  $H^p$ -norm.

To justify the use of Tikhonov regularization, we have the following theorems:

**Theorem 2.2.10** *The operator  $S_{x_r, \infty} : C(\partial D) \rightarrow L^2(\Omega)$  is compact.*

**Proof:** The operator  $S_{x_r, \infty}$  has a continuous kernel, then it is compact. □

**Theorem 2.2.11** *The operator  $(S_{x_r, \infty} \psi)' : C(\partial D) \rightarrow L^2(\Omega)$  is compact.*

**Proof:** The result follows from Theorem 2.2.3. □

**Theorem 2.2.12** *Assume that  $k^2$  is not an interior Neumann eigenvalue for the negative Laplacian in  $D$ . Moreover, let  $x_r$  be a parameterization of the boundary  $\partial D$  and let  $\frac{\partial u}{\partial \nu}$  be given by the solution of Equation (24). Then  $h(t) = 0$  is the only sufficiently small twice differentiable and  $2\pi$  periodic function that solves*

$$\left( S_{x_r, \infty} \frac{\partial u}{\partial \nu} \right)' h = 0 \quad (31)$$

for  $t \in [0, 2\pi]$ .

**Proof:** On page 61 of [15]. □

Using these three theorems, and taking  $(S_{x_r, \infty} \frac{\partial u}{\partial \nu})'$  as  $A$  in Theorem 2.2.2, the Tikhonov regularization to the equation in the second step is a regularization scheme.

We write from now on  $S'_{x_r^{(j)}, \infty} = (S_{x_r^{(j)}, \infty} \frac{\partial u}{\partial \nu})'$ . We use the Fréchet derivative (26) to obtain the update  $h$  solving

$$(\lambda^{(j)} I^p + (S'_{x_r^{(j)}, \infty})^* S'_{x_r^{(j)}, \infty}) h = (S'_{x_r^{(j)}, \infty})^* \left( S_{x_r^{(j)}, \infty} \frac{\partial u}{\partial \nu} - u_\infty \right), \quad (32)$$

where  $\left(S'_{x_r^{(j)}, \infty}\right)^*$  is the  $L^2$  adjoint of  $S'_{x_r^{(j)}, \infty}$ , and  $I^p$  is the identity operator with respect to the norm  $H^p$  for the solution space  $\mathbb{X}$ . This operator is related to the  $H^p$  norm of the solution, which in this case for a function  $f \in H^p(\Omega)$  is

$$\begin{aligned} \|f\|_{H^p(\Omega)}^2 &= \sum_{j=0}^p \|D^j f\|_{L^2(\Omega)}^2 \\ &= \sum_{j=0}^p \left[ \int_0^{2\pi} \left( \frac{d^j f(\tau)}{d\tau^j} \cdot \frac{d^j f(\tau)}{d\tau^j} \right) d\tau \right]. \end{aligned}$$

Equation (32) represents a Gauss–Newton method step for minimizing

$$\left\| S_{x_r^{(j)}, \infty} \frac{\partial u}{\partial \nu} - u_\infty \right\|_{L^2(\Omega)}^2 + \lambda^{(j)} \|x - x^{(j)}\|_{H^1([0, 2\pi])}^2$$

with respect to the domain  $x^{(j)}$ . To implement the constraint that  $x_r^{(j)} + h_r \in \mathbb{X}_{N_r}$ , we must use a projection method and project into  $\mathbb{X}_{N_r}$ . We define the projection operator  $P_{\mathbb{X}_{N_r}} : \mathbb{S} \rightarrow \mathbb{X}$ , such that  $P_{\mathbb{X}_{N_r}}(x_r^{(j)} + h_r) \in \mathbb{X}_{N_r}$ , where  $\mathbb{S}$  is the space of all possible solutions of Equation (32).

There are different ways to implement the second step in the procedure to solve problem (29). We mention two ways in particular:

#### Method A:

1. After solving Equation (24) for  $\psi$  using  $x^{(j)}$ , we set a value for  $\lambda^{(j)}$ . We present in the next section how to choose  $\lambda^{(j)}$ .
2. Solve Equation (32) to obtain  $h_r$ . We make the update  $x_r^{(j+1)} = P_{\mathbb{X}_{N_r}}(x_r^{(j)} + h_r)$ .
3. After obtaining  $x_r^{(j+1)}$  we go back to the first step of the method.

This implementation was used in [16; 18].

## Method B:

1. Solve Equation (24) for  $\psi$  using  $x^{(j)}$ .
2. Repeat until a stopping criterion is reached:
  - (a) Choose  $\lambda^{(j,l)}$  and solve Equation (32) for  $h$ . We make  $x_r^{(j,l+1)} = P_{\mathbb{X}_{N_r}} \left( x_r^{(j,l)} + h_r \right)$  for  $l \in \{0, 1, \dots, N_f\}$ , where  $N_f$  is the final iteration.
  - (b) Set  $x^{(j+1)} = x^{(j, N_f)}$  and start the procedure over again.

We call this implementation of Method B from now on in this thesis.

In this thesis, we present a comparison of results for both methods in the Chapter 4, and we show that Method B is more efficient. Although the methods have very similar implementations, they present a big difference in their computational cost.

We define the following computational costs:

- Assembling matrix  $S_{x_r^{(j)}}: A_1(k)$
- Solution of Equation (24):  $C_1 k^3$
- Assembling matrix  $S_{x_r^{(j)}, \infty}: A_2(k, N_{ff})$
- Assembling matrix  $(S_{x_r^{(j)}, \infty} \frac{\partial u}{\partial \nu})': A_3(k, N_{ff}, N_r)$
- Solution of Equation (32):  $C_2 N_r^3$

The two-step procedure cost for Method A is

$$A_1(k) + C_1 k^3 + A_2(k, N_{ff}) + A_3(k, N_{ff}, N_r) + C_2 N_r^3.$$

As for Method B, the cost of the two-step procedure is

$$A_1(k) + C_1 k^3 + N_{\text{int}} [A_2(k, N_{ff}) + A_3(k, N_{ff}, N_r) + C_2 N_r^3],$$

where  $N_{\text{int}} \geq 1$  is the number of iterations solving Equation (32).

It appears that the two-step procedure is more computationally expensive for Method B than for Method A, because of the multiplying factor related to the number of iterations inside of the two-step procedure. However, we can expect that our approximation of the domain is better after the two-step procedure of Method B than it is after that of Method A because  $\lambda^{(j,l)}$  is updated more frequently, and therefore, fewer iterations are needed.

Overall, we can expect that Method B will have fewer iterations of the two-step procedure than will Method A. The advantage of using Method B in place of Method A is that it minimizes the number of times that we have to solve Equation (24). Of the two systems

that we solve, system in Equation (24) is generally more expensive to solve than the system in Equation (32), because to solve Equation (24) the number of operations is proportional to the cube of the wavenumber while for Equation (32), the number of operations necessary to find the solution is proportional to the number of degrees of freedom chosen for the solution space  $\mathbb{X}_{N_r}$ . Although the performance of the methods does not seem too different for low wavenumbers, it is more pronounced at higher wavenumbers. We present results comparing the results of Methods A and B in Chapter 4.

### 2.2.5 Globalization techniques

To improve the convergence of the methods, we make use of globalization techniques that can be found in [19; 20; 47], and [55]. There are several different ways to implement globalization techniques to ensure the convergence of our methods. We focus specifically on the choice of the regularization parameter  $\lambda$  and the choice of a scaling factor that will shorten the size  $h$  of the step, in order to ensure the convergence of the method.

To find an appropriate the value for the regularization parameter  $\lambda$  we use the Levenberg–Marquardt hook-step approach [56; 57]. In this approach, we solve the following equation instead of Equation (32):

$$(\lambda^{(j)}I^p + (S'_{x_r^{(j)},\infty})^* S'_{x_r^{(j)},\infty})h = (S'_{x_r^{(j)},\infty})^* \left( S_{x_r^{(j)},\infty} \frac{\partial u}{\partial \nu} - u_\infty \right). \quad (33)$$

Note that we use a different value for  $\lambda^{(j)}$  to calculate  $h$  at each step. There are different ways of choosing the value of  $\lambda^{(j)}$ , and we choose two values

$$\lambda^{(j)} = \|S_{x_r^{(j)},\infty} \frac{\partial u}{\partial \nu} - u_\infty\|$$

as in [58], and

$$\lambda^{(j)} = \|S_{x_r^{(j)},\infty} \frac{\partial u}{\partial \nu} - u_\infty\|^2$$

as in [47].

**Remark 2.2.1** *There are other choices; for example, one could choose a constant value [23], or an integer power of the norm of the residue as in [18].*

Finally, we deal with the problem of finding an acceptable length for the step  $h$  in a given direction of search. Sometimes, the step size  $h$  is too big and we need to apply a globalization technique. In this case, a scaling factor is used to control the size of the step, and we update the domain by setting

$$x_r^{(j,l+1)} = P_{\mathbb{X}_{N_r}}(x_r^{(j,l)} + \rho h_r),$$

where  $P_{\mathbb{X}_{N_r}}$  is the projection operator on the space  $\mathbb{X}_{N_r}$  and the parameter  $\rho$  is the scaling factor.

One way of implementing this scaling factor is to use the backtracking line-search framework with the Armijo rule [59]:

**Armijo rule:**

We pick an  $\alpha \in (0, 1)$  and choose a  $\rho_j$  from among those  $\rho > 0$  that satisfies

$$f(x_r^{(j)} + \rho h_r) \leq f(x_r^{(j)}) + \alpha \rho \operatorname{grad} f(x_r^{(j)})^* h_r.$$

We have this algorithm in Figure (2.4).

**Algorithm 2.2.2** *Backtracking line-search*

1. Given  $\alpha \in (0, 1/2)$ ,  $0 < l < u < 1$
2. Set  $\rho_k = 1$ ;
3. Repeat until the Armijo rule is satisfied
  - (a)  $\rho_k = \theta \rho_k$  for some  $\theta \in [l, u]$ , where  $\theta$  is newly chosen each time by the line search;
4. Set  $x_r^{(j+1)} := P_{\mathbb{X}_{N_r}}(x_r^{(j)} + \rho_k h_r)$ .

Figure 2.4: Backtracking line-search framework

In practice, the chosen  $\alpha$  is very small. There are several different ways to choose the parameter  $\theta$ , and we choose a constant  $\theta \in [l, u]$ .

Another way to implement the scaling factor that is simpler than the backtracking procedure implemented above is to choose it to be constant over all the steps. We can see numerical results for this approach in [18].

We present a summary of the algorithm for solving the acoustic inverse scattering problem for a single frequency with Levenberg–Marquardt using line-search with the Armijo rule in Figure (2.6).

## 2.2.6 The use of multiple frequencies

We have so far presented techniques for solving inverse scattering problem: that is, given the far field pattern generated by the reflection of one incident wave, we have shown how

**Algorithm 2.2.3** *Given the measured far-field pattern  $u_\infty$ .*

1. Choose an initial guess  $x^{(0)}$ .

2. Repeat while the stopping criteria are not reached:

(a) Set the domain  $\partial D^{(j)}$  with parameterization  $x^{(j)}$  and solve

$$S_{x_r^{(j)}} \frac{\partial u}{\partial \nu} = u^{inc}$$

for  $\frac{\partial u}{\partial \nu}$ .

(b) Set  $x^{(j,0)} = x^{(j)}$ .

(c) Repeat while the stopping criteria are not reached:

i. Set the regularization parameter  $\lambda^{(j,l)}$  and solve the equation

$$h_r = L \left( u_\infty - S_{x_r^{(j,l)}, \infty} \frac{\partial u}{\partial \nu} \right).$$

with

$$L = \left( \lambda^{(j,l)} H^p + \left( S'_{x_r^{(j,l)}, \infty} \right)^* \left( S'_{x_r^{(j,l)}, \infty} \right) \right)^{-1} \left( S'_{x_r^{(j,l)}, \infty} \right)^*$$

ii. Use the line-search algorithm with the Armijo rule to update  $x_r^{(j,l+1)} = P_{\mathbb{X}_{N_r}} \left( x_r^{(j,l)} + \rho h_r \right)$ .

(d) Update  $x^{(j+1)} = x^{(j, N_f)}$ , where  $N_f$  is the total number of iterations to reach the stopping criteria.

Figure 2.5: The heuristic Method B based on Johansson and Sleeman's method to solve the inverse scattering problem.

to reconstruct the shape of an object. With respect to the solution of the inverse problem (2.2.3), we have that there is a relation between the solution and the wavenumber  $k$ . In practice, the coarse scale of an object can be recovered from the far field pattern generated by one incident plane wave with a slow frequency. Chen discussed the following remark in [21]:

**Remark 2.2.2** *Given the far-field measurements of the scatterer  $D$ , we cannot determine features of the scatterer  $D$  that are less than half a wavelength.*

In general, at low frequencies, the reconstruction problem is uniquely solvable [50], but its stability is poor [60; 61]. This means that we do not need an initial guess very close to the

object to solve the problem, but it is difficult to reconstruct small details of the object. On the other hand, at higher frequencies the inverse problem may not be uniquely solvable, but it is more stable—so we can reconstruct details of the object but we need a better initial guess to use with our algorithms. This relation between the wavenumber  $k$  and the initial guess motivates the use of multifrequency data.

We have the following problem:

**Problem 2** *Given the far field pattern patterns  $u_\infty^{k_j}$  at  $\hat{x}_l \in \Omega$ , for  $j \in \{1, \dots, N_{\text{inc}}\}$  and where  $\Omega$  is the unit circle, generated by the scattering of the  $N_{\text{inc}}$  incident plane waves  $u_j^{\text{inc}}(x) = e^{ik_j x \cdot d}$  with fixed direction  $d$  and varying wavenumbers  $k_j \in [k_l, k_h]$ , such that  $0 < k_l < k_j < k_h$ , off of an unknown object  $D$  with homogeneous Dirichlet boundary condition, reconstruct the shape of  $D$ .*

We previously cited the result of uniqueness for each frequency. In the case of a band of wavenumbers  $[k_l, k_h]$ , the uniqueness of this inverse problem was proved in [62]. For finitely many wavenumbers, we have uniqueness of the solution if the lowest frequency is small enough [50; 63].

One way to solve Problem 2 is to use the recursive linearization algorithm (RLA) proposed first in [21], and later analyzed in [22] for the inhomogeneous medium problem, and analyzed in [23] for impenetrable obstacles and far field measures with noise.

Having chosen an initial guess for the domain  $\partial D$  at the frequency  $k_0$ , say  $x^{(k_0)}$ , the idea of this algorithm is to solve the inverse scattering problem using the Newton method for each frequency  $k_j$ ,  $j = 1, \dots, N_{\text{inc}}$  using the solution of the problem for the previous frequency.

The linear convergence of this algorithm was proved for the case of the inhomogeneous medium with noiseless data in [22] and for the Dirichlet boundary condition case in [23].

There are other recursive algorithms that can be used, such as the second order approximation or the fully nonlinear recursive algorithm, see, *e.g.*, [64; 65]. This algorithm is equivalent to solving the Newton method for the far field pattern generated by the plane wave with wavenumber  $k_j$ , and then using this solution as the initial guess for the Newton method for the far field pattern data generated by the plane wave with wavenumber  $k_{j+1}$ .

Instead of applying the Newton method that uses the expensive Fréchet derivative of the operator  $F(x_r)$  for each frequency, we will solve the problem using Method B. In our alternative to the RLA, we solve the problem for each frequency using Method B presented for the solution of the single frequency problem. We call this procedure Method RLA-B.

First, we use Algorithm 2.2.2 with the data at the lowest wavenumber  $k_1$  to obtain a rough approximation of the object's shape using a initial guess not necessarily very close to the solution. Once we obtain the approximate solution for the problem at the lowest frequency, we use this approximate solution as the initial guess for the next wavenumber  $k_2$ .

**Algorithm 2.2.4 Recursive Linearization Algorithm**

Given  $u_\infty^{k_j}$  for  $k_j = k_0, \dots, k_N$  and the parameters  $\lambda > 0$ ,  $\gamma > 0$ .

1. Find an approximation  $x^{(k_0)}$  of the shape  $x = \partial D$  at the lowest frequency  $k_0$  by minimizing the functional

$$f(x_r) = \frac{1}{2} \|M^{(i)}(x_r) - u_\infty^{k_0}\|_{L^2([0,2\pi])}^2 + \frac{1}{2} \gamma \|x - x^{(i)}\|_{L^2([0,2\pi])}^2 \quad (34)$$

2. For  $j = 1, \dots, N$  do

- (a) Set the solution  $x^{(k_{j-1})}$  as the initial guess for the Newton method.
- (b) Use the Newton method to find the approximation  $x^{(k_j)}$  of the object at the frequency  $k_j$ .

Figure 2.6: The Recursive Linearization Algorithm.

We repeat this process until we reach a desired result or use the entire set of data up to the highest wavenumber  $k_{N_{\text{inc}}}$ .

Suppose that our data set contains measures of the far field pattern for an object  $D$  at the points  $\hat{x}_l$ ,  $l \in \{1, \dots, N_{ff}\}$  for different wavenumbers  $k_j$ ,  $j \in \{1, \dots, N_{\text{inc}}\}$ , ordered from the lowest to the highest wavenumber. The following is a summary of the algorithm:

**Algorithm 2.2.5** Given the far field pattern  $u_\infty^{k_j}$  for  $j \in \{1, \dots, N_{\text{inc}}\}$  and an initial guess  $x^{(0)}$  for the approximation of the domain

1. For  $j \in \{1, \dots, N_{\text{inc}}\}$ :

- (a) Set the initial guess  $x^{(j,0)} = x^{(j-1)}$ ;
- (b) Use Algorithm 2.2.2 with the far field pattern measurements  $u_\infty^{k_j}$  and the initial guess  $x^{(j,0)}$ . Call the approximation obtained  $x^{(j)}$ .

Figure 2.7: Iterative method for solving the inverse problem for an object  $D$  with Dirichlet boundary conditions using multiple frequencies far field pattern measures.

This approach enables us to obtain an accurate reconstruction of the part of the obstacle boundary illuminated by the incident plane waves without requiring a good initial guess.

We should not expect to obtain a good approximation in the shadowed part of the object, since for higher frequencies, the scattered field of the object goes to zero in that region. In fact, it was shown in [23] that the reconstruction is stable in the illuminated convex part of the object.

### 2.2.7 Inverse scattering of a single object in the presence of multiple scatterers

In the last section, we presented our alternative version of the RLA. We are able to reconstruct details of the object in the illuminated part, however, our approximation of the shadow part of the object is very poor. To improve our reconstruction of the shadow part, we insert obstacles of known shape, so that the incident waves will reflect from those objects and illuminate the shadow part of the object.

We want to adapt our iterative method to a configuration with multiple scatterers. In this case, we will assume that the shape of the scatterers  $D_s$ ,  $s = 2, \dots, N_D$  is known, and that we want to reconstruct the shape of the object  $D_1$ . The first part of the algorithm is similar to the direct problem previously presented. We must change the second part of the problem, in which we solve the linearized version of Equation (9).

The Fréchet derivative with respect to the domain  $D_1$  is:

$$(S'_{\partial D_1, \infty}[y, \phi]h)(\hat{x}) = ik \frac{e^{i\pi/4}}{\sqrt{8\pi k}} \int_{\partial D_1} e^{-ik\hat{x}(\theta) \cdot y} \phi(y) \hat{x} \cdot h \, ds(y).$$

Since the other objects remain the same, we have  $(S'_{\partial D_s, \infty}[y, \phi]h)(\hat{x}) = 0$  for all  $s = 2, \dots, N_D$ . The linearized equation becomes

$$(S'_{\partial D_1, \infty}[y, \phi]) h(\hat{x}) = u_\infty(\hat{x}) - \sum_{s=1}^{N_D} (S_{\partial D_s, \infty} \phi)(\hat{x}),$$

where  $\phi = \frac{\partial u}{\partial \nu}$ .

# Chapter 3

## Numerical solution of the direct problem at low frequencies

### 3.1 The case of a single scatterer

#### 3.1.1 Numerical implementation

There are several different ways to discretize Equations (3) and (6). Amongst those choices we have the collocation method, the Galerkin method, and the Nyström method. For this problem, the Nyström method was recommended by Colton and Kress in [3]. It is clear that the Nyström method and the collocation method require less computational effort than the Galerkin method, because the former methods require numerical integration to solve only one integral, while the Galerkin method requires two numerical integrations of a double integral.

We note that the collocation method requires that we choose a basis and sometimes this choice of basis can generate an unstable discrete operator. This is the reason that we prefer the Nyström method over the collocation method.

Parameterizing the domain  $\partial D$  by  $x : [0, 2\pi] \rightarrow \mathbb{R}^2$ , with  $x(t) = (x_1(t), x_2(t))$ , Equation (3) becomes

$$\int_0^{2\pi} \frac{i}{4} H_0^{(1)}(k|x(t) - x(\tau)|) \frac{\partial u}{\partial \nu}(x(\tau)) |x'(\tau)| d\tau = u^{\text{inc}}(x(t)), \quad (35)$$

where  $H_n^{(1)} = J_n + iY_n$  is the Hankel function of first kind of order  $n$ ,  $J_n$  is the Bessel function of order  $n$ , and  $Y_n$  is the Neumann function of order  $n$ . The Bessel function of order  $n$  is an analytic function given by the formula

$$J_\nu(t) = \left(\frac{1}{2}t\right)^\nu \sum_{p=0}^{\infty} \frac{(-\frac{1}{4}z^2)^p}{p! \Gamma(\nu + p + 1)}.$$

As for the Neumann function of order  $n$ , we have the formula

$$Y_\nu(t) = \frac{J_\nu(t) \cos(\nu\pi) - J_{-\nu}(t)}{\sin(\nu\pi)},$$

see [66].

For  $n = 0, 1, 2, \dots$  the Bessel function of order  $n$  can be written as

$$J_n(t) = \sum_{p=0}^{\infty} \frac{(-1)^p}{p!(n+p)!} \left(\frac{t}{2}\right)^{n+2p},$$

and the Neumann function can be written as

$$\begin{aligned} Y_n(t) &= \frac{2}{\pi} \left\{ \ln \left( \frac{t}{2} + C \right) \right\} J_n(t) - \frac{1}{\pi} \sum_{p=0}^{n-1} \frac{(n-1-p)!}{p!} \left(\frac{2}{t}\right)^{n-2p} \\ &\quad - \frac{1}{\pi} \sum_{p=0}^{\infty} \frac{(-1)^p}{p!(n+p)!} \left(\frac{t}{2}\right)^{n+2p} \{ \phi(p+n) + \phi(p) \}, \end{aligned}$$

where  $C$  is Euler's constant. For the case  $n = 0$ , the second term of the Neumann function is set to zero, and we define  $\phi(0) := 0$ ,

$$\phi(p) := \sum_{m=1}^p \frac{1}{m}, \quad p = 1, 2, \dots$$

We notice the singularity in the Neumann function of order 1. We have a logarithmic singularity in the kernel of Equation (52). We will follow the approach of [3; 33; 34], in which the authors divide the kernel of the single layer operator into two parts: an analytic part  $K_1(t, \tau)$ , and a singular part  $K_2(t, \tau)$ . We have the following equation:

$$\int_0^{2\pi} \left( K_1(t, \tau) \ln \left( 4 \sin^2 \left( \frac{t-\tau}{2} \right) \right) + K_2(t, \tau) \right) \frac{\partial u}{\partial \eta}(x(\tau)) |x'(\tau)| d\tau = u^{\text{inc}}(x(t))$$

where

$$\begin{aligned} K_1(t, \tau) &= -\frac{1}{2\pi} J_0(k|x(t) - x(\tau)|), \\ K_2(t, \tau) &= H_0^{(1)}(t, \tau) - K_1(t, \tau) \ln \left( 4 \sin^2 \left( \frac{t-\tau}{2} \right) \right), \end{aligned}$$

and at the singular point, we have:

$$\begin{aligned} K_1(t, t) &= 0, \\ K_2(t, t) &= \frac{i}{2} - \frac{C}{\pi} - \frac{1}{2\pi} \ln \left( \frac{k^2}{4} |x'(t)| \right). \end{aligned}$$

To solve this problem numerically we discretize the domain  $[0, 2\pi]$  uniformly with the points  $t_m = m\pi/N_m$ , where  $2N_m$  is the number of points (and it must increase linearly with respect to the wavenumber  $k$ ), and  $m = 0, \dots, 2N_m - 1$ . We evaluate the integral

$$I_1(t) = \int_0^{2\pi} K_1(t, \tau) f(\tau) d\tau,$$

where  $f(\tau) = \frac{\partial u}{\partial \eta}(x(\tau))|x'(\tau)|$ , using the finite Fourier series approximation of the function  $f(\tau)$ . We have the following finite Fourier series approximation:

$$f(t) \approx f_{N_m} = \frac{a_0}{2} + \sum_{j=1}^{N_m-1} (a_j \cos(jt) + b_j \sin(jt)) + a_{N_m} \cos(N_m t),$$

where

$$a_j = \frac{1}{N_m} \sum_{m=0}^{2N_m-1} f(t_m) \cos\left(\frac{\pi j m}{N_m}\right),$$

$$b_j = \frac{1}{N_m} \sum_{m=0}^{2N_m-1} f(t_m) \sin\left(\frac{\pi j m}{N_m}\right).$$

We say that  $f_{N_m}$  is in the space  $\mathcal{T}_{N_m}$  of trigonometric polynomials

$$p_{N_m}(t) = \frac{a_0}{2} + \sum_{j=1}^{N_m-1} (a_j \cos(jt) + b_j \sin(jt)) + a_{N_m} \cos(N_m t),$$

where  $a_0, a_{N_m}, a_j, b_j \in \mathbb{R}$ , for  $j = 1, \dots, N_m - 1$ .

To obtain the numerical approximation for the integral  $I_1$ , we use the following lemma:

**Lemma 3.1.1**

$$\int_0^{2\pi} \ln\left(4 \sin^2\left(\frac{t-\tau}{2}\right)\right) \cos(m\tau) d\tau = \begin{cases} 0, & m = 0 \\ -\frac{2\pi}{|m|}, & m \in \mathbb{Z} - \{0\} \end{cases}$$

$$\int_0^{2\pi} \ln\left(4 \sin^2\left(\frac{t-\tau}{2}\right)\right) \sin(m\tau) d\tau = 0, m \in \mathbb{Z}.$$

**Proof:** We consider an adaptation of the procedure shown in [67]. □

To simplify the notation, we set for the rest of this section  $\psi(\tau) = \frac{\partial u}{\partial \eta}(x(\tau))|x'(\tau)|$ . Using the series representation of  $a_j$  and  $b_j$  together with the lemma we obtain the following numerical approximation for  $I_1$ :

$$I_1(t) \approx \sum_{m=0}^{2N_m-1} R(t, t_m) \psi(t_m), \tag{36}$$

where we have the quadrature terms

$$R(t, t_m) \approx -\frac{2\pi}{N_m} \sum_{m=0}^{2N_m-1} \frac{1}{m} \cos(m(t - t_m)) - \frac{\pi}{N_m^2} \cos(N_m(t - t_{N_m})).$$

For the integral  $I_2(t)$ , since the kernel is analytic, we apply a quadrature midpoint rule (trapezoidal rule). We obtain:

$$I_2(t) \approx \frac{\pi}{N_m} \sum_{m=0}^{2N_m-1} K_2(t, t_m) \psi(t_m). \quad (37)$$

Putting the approximations in Equations (36) and (37) together, we obtain

$$\left( R(t, t_m) K_1(t, t_m) + \frac{\pi}{N_m} K_2(t, t_m) \right) \psi(t_m) = u^{\text{inc}}(x(t)). \quad (38)$$

Choosing  $t = t_m$  for  $m = 0, \dots, 2N_m - 1$  in Equation (38), we obtain a linear system of equations with  $2N_m - 1$  equations and  $2N_m - 1$  unknowns. We write the system

$$\mathbf{S}_{\partial D} \psi = \mathbf{u}^{\text{inc}}(\mathbf{x}), \quad (39)$$

where  $\mathbf{S}_{\partial D}$  is the matrix equivalent to the discretization of the operator  $S_{\partial D}$ ,  $\mathbf{x} = (x(t_1), \dots, x(t_{N_m-1}))$  is the vector of the points  $x(t_m)$  on the boundary of  $D$ , and  $\psi$  and  $\mathbf{u}^{\text{inc}}(\mathbf{x})$  are respectively the value of  $\psi(t)$  and the values of the incident wave at the points  $x(t_m)$  on the boundary of  $D$ . The elements  $s_{jm}^{(\partial D)}$  of the matrix  $\mathbf{S}_{\partial D}$  are

$$s_{jm}^{(\partial D)} = R(t_j, t_m) K_1(t_j, t_m) + \frac{\pi}{N_m} K_2(t_j, t_m), \text{ for } j, m = 0, \dots, 2N_m - 1,$$

and the components  $u_j^{(\partial D)}$  of the vector  $\mathbf{u}^{\text{inc}}(\mathbf{x})$  are

$$u_j^{(\partial D)} = e^{ikx(t_j) \cdot d}, \text{ for } j = 0, \dots, 2N_m - 1.$$

After solving the system in Equation (39) and obtaining the values for  $\psi(t)$  at the points  $t_m = \frac{m\pi}{N_m}$  for  $m = 0, \dots, 2N_m - 1$ , we use these values to obtain the far field pattern generated by the object  $D$  from the scattering of the incident plane wave  $u^{\text{inc}}$ . We need to solve Equation (6) numerically to obtain the far field pattern for the object  $D$  at  $N_{ff}$  points  $\hat{x}_l \in [0, 2\pi]$ ,  $l = 1, \dots, N_{ff}$ . Using the trapezoid rule, we obtain the discrete equivalent of the operator  $S_{\partial D, \infty}$ ,  $\mathbf{S}_{\partial D, \infty}$ , with elements

$$s_{lm}^{(\partial D, \infty)} = \frac{\pi}{N_m} e^{-ik\hat{x}_j \cdot x(t_m)},$$

for  $m = 0, \dots, 2N_m - 1$ , and  $l = 1 \dots, N_{ff}$ .

To find the far field at the points  $\hat{x}_l$ , we multiply the  $N_{ff} \times (2N_m - 1)$  matrix  $\mathbf{S}_{\partial\mathbf{D},\infty}$  by the solution  $\psi$  of (39), obtaining

$$\mathbf{u}_\infty(\hat{\mathbf{x}}) = \mathbf{S}_{\partial\mathbf{D},\infty}\psi,$$

where  $\mathbf{u}_\infty(\hat{\mathbf{x}}) = (u_\infty(\hat{x}_1), \dots, u_\infty(\hat{x}_{N_{ff}}))$  is the vector with the value of the far field pattern at the points  $\hat{x}_l$ .

### 3.1.2 Numerical analysis

We present some numerical results for the direct scattering problem, using the Nyström method that can be found in [68]. We start by presenting the following definition, and noting that more details can be found in [69].

**Definition 3.1.1** *Let  $H^p([0, 2\pi])$  for  $p \geq 1$  be the Sobolev space of  $2\pi$ -periodic functions on the interval  $[0, 2\pi]$ , i.e., the space of  $2\pi$ -periodic functions  $\phi$  with the property*

$$\sum_{m=-\infty}^{\infty} (1 + m^2)^p |c_m|^2 < \infty, \quad (40)$$

where the  $c_m$  are the Fourier coefficients of  $\phi$ .

We define the trigonometric interpolation operator  $P_{N_m} : C([0, 2\pi]) \rightarrow \mathbb{R}$  that interpolates the function  $\phi$  with the formula

$$P_{N_m}(\phi) = \sum_{j=0}^{2N_m-1} \phi(t_j) L_j^{(N_m)}, \quad (41)$$

where  $L_j^{(N_m)}$  is the Lagrange trigonometric polynomial given by

$$L_j^{(N_m)} = \frac{1}{2} \left\{ 1 + 2 \sum_{j=1}^{2N_m-1} \cos(m(t - t_j)) + \cos(N_m(t - t_j)) \right\}. \quad (42)$$

We obtain the following result with respect to the trigonometric interpolation of polynomials:

**Theorem 3.1.1** *For the trigonometric interpolation operator we have the error estimate*

$$\|P_n\psi - \psi\|_{H^q([0, 2\pi])} \leq c \left( \frac{\pi}{N_m} \right)^{p-q} \|\psi\|_{H^p([0, 2\pi])}, \quad 0 \leq q \leq p, \quad \frac{1}{2} < p, \quad (43)$$

for all  $\psi \in H^p([0, 2\pi])$  and some constant  $c$  (depending on  $p$  and  $q$ ).

**Proof:** See [68].

Using the last theorem, we can prove the following result with respect to the approximate solution of the Equation (6):

**Theorem 3.1.2** *Let  $\psi \in H^p([0, 2\pi])$ , where  $p > 3/2$ , be the solution to Equation (3). The approximate solution  $\psi_{N_m}$  to Equation (3) obtained using the Nyström method with  $N_m$  modes is unique and we have the following estimate:*

$$\|\psi - \tilde{\psi}\|_{H^{q+1}([0, 2\pi])} \leq c \left( \frac{\pi}{N_m} \right)^{p-q} \|\psi\|_{H^{p-1}([0, 2\pi])}, \quad 1 \leq q \leq p. \quad (44)$$

**Proof:** See [68].

If the domain boundary  $\partial D$  is infinitely differentiable, the convergence rate is faster than any polynomial power of the discrete step  $\pi/N_m$ , as we can see in the numerical results given in the next section.

### 3.1.3 Numerical results

We present some examples of the calculation of the normal derivative of the field on  $\partial D$  and the far field generated by the scattering of a plane wave off of the object  $D$ .

#### Example 3.1.1

Consider the object  $D$  to be the circle with radius 1, centered at the origin. We consider the acoustic scattering problem for the plane wave with direction  $d = (1, 0)$  and wavenumbers  $k = 1$  and 5. The normal derivative of the field on  $\partial D$  was calculated at points uniformly distributed over the interval  $[0, 2\pi]$ ,  $x(t_m)$ , for  $t_m = \pi m/N_m$ ,  $m = 0, \dots, 2N_m - 1$ , with varying  $N_m$ . We calculate the real and complex part of the far field pattern  $u_\infty$  at the points  $\hat{x}_1 = (1, 0)$  and  $\hat{x}_2 = (-1, 0)$  using the values of the normal derivative of the field calculated with different  $N_m$ . The result is presented in Table 3.1.

#### Example 3.1.2

Consider the object  $D$  that has parameterization  $x : [0, 2\pi] \rightarrow \mathbb{R}^2$ , such that  $x(t) = (\cos(t) + 0.65 \cos(2t) - 0.65, 1.5 \sin(t))$ . We consider the acoustic scattering problem for the plane wave with direction  $d = (1, 0)$  and wavenumbers  $k = 1$  and 5. The normal derivative of the field on  $\partial D$  was calculated at points uniformly distributed over the interval  $[0, 2\pi]$ ,  $x(t_m)$ , for  $t_m = \pi m/N_m$ ,  $m = 0, \dots, 2N_m - 1$ , with varying  $N_m$ . We calculate the real and complex part of the far field pattern  $u_\infty$  at the points  $\hat{x}_1 = (1, 0)$  and  $\hat{x}_2 = (-1, 0)$  using the values of the normal derivative of the field calculated with different  $N_m$ . The result is presented in Table 3.2.

$k$	$N_m$	$\text{Re}(u_\infty(\hat{x}_1))$	$\text{Im}(u_\infty(\hat{x}_1))$	$\text{Re}(u_\infty(\hat{x}_2))$	$\text{Im}(u_\infty(\hat{x}_2))$
k=1	8	- 1.334329188063	0.333726766344	0.181637801094	0.762482655016
	16	- 1.334362929767	0.333695654409	0.181849734687	0.762686731981
	32	- 1.334362929769	0.333695654407	0.181849734688	0.762686731982
	64	- 1.334362929769	0.333695654407	0.181849734688	0.762686731982
	128	- 1.334362929769	0.333695654407	0.181849734688	0.762686731982
k=5	8	- 1.986831402118	0.485295285649	- 0.422300542958	0.095732670775
	16	- 1.826278487306	1.101243955268	0.610309598972	- 0.359816840301
	32	- 1.849386998826	1.098974319078	0.620998659379	- 0.352399089264
	64	- 1.849387027437	1.098974291243	0.620998659384	- 0.352399089277
	128	- 1.849387027437	1.098974291243	0.620998659384	- 0.352399089277

Table 3.1: Far field pattern for Example 3.1.1. The object  $D$  is the circle with radius 1, centered at the origin. We vary the discretization step increasing the value of  $N_m$ .

$k$	$N_m$	$\text{Re}(u_\infty(\hat{x}_1))$	$\text{Im}(u_\infty(\hat{x}_1))$	$\text{Re}(u_\infty(\hat{x}_2))$	$\text{Im}(u_\infty(\hat{x}_2))$
k=1	8	- 1.618381695675	0.606752164102	1.416909410769	0.080109038586
	16	- 1.627476854614	0.602315684865	1.397221837801	0.094476191840
	32	- 1.627457445405	0.602225838875	1.396944648697	0.094997221929
	64	- 1.627457503695	0.602225912525	1.396944882313	0.094996358536
	128	- 1.627457503694	0.602225912524	1.396944882311	0.094996358533
k=5	8	- 1.377090397189	2.127972815671	- 0.384525312729	- 0.014674739378
	16	- 2.365174647855	1.725065657606	- 0.253616783423	0.139640857157
	32	- 2.465534936698	1.688929672563	- 0.199212087324	0.060993039836
	64	- 2.475543796632	1.687479379007	- 0.199457879732	0.060158937522
	128	- 2.475543801434	1.687479372453	- 0.199457879741	0.060158937516

Table 3.2: Far field pattern for Example 3.1.2. The object  $D$  is the Kite with parameterization  $x(t) = (\cos(t) + 0.65 \cos(2t) - 0.65, 1.5 \sin(t))$ .

From the results in Tables (3.1) and (3.2), we can verify the fast convergence of the implementation of our problem using the Nyström method. It is worth emphasizing the fact that when we increase the wavenumber  $k$ , we need to increase the number of modes used in the Nyström method. This aspect of the method is due to the oscillatory behavior of the integrals in Equations (3) and (6).

**Remark 3.1.1** *We can apply the same numerical method to solve the Neumann and the impedance problem. In this case, we will need to solve different integral equations.*

**Remark 3.1.2** *The number of discretization points  $N_m$  necessary to obtain a good approximation of the solution of (3) grows linearly with the wavenumber  $k$ . This means that the number of elements of the matrix  $\mathbf{S}_{\partial\mathbf{D}}$  is proportional to  $\mathcal{O}(k^2)$ . For small values of the parameter  $k$ , the method presented in this chapter works well, but for very high wavenumbers this method becomes computationally expensive. To overcome this setback we present a method in the following chapters based on the ideas in [26; 27].*

## 3.2 The case of multiple scatterers

The solution to the problem for multiple scatterers can be obtained in different ways; for a complete survey of the subject, see [24]. We present here the solution using all of the integral equations obtained simultaneously. This method is very easy to implement and precise; on the other hand, it becomes increasingly computationally expensive with increasing frequency (and consequently the wavenumber  $k$ ), increasing number of objects  $N_D$ , and increasing number of dimensions (from two to three). In the case that the problem becomes intractable due to computational complexity, there are other methods, such the iterative method presented in [25]. Although we do not consider this method in this thesis, we intend to work with it in the future.

The procedure of finding the far field pattern and scattered field in the presence of multiple objects is very similar to the procedure we would use in the case of a single object. To find the normal derivative of the field on the boundary of the objects  $D_s$ , we use the Nyström method. Suppose each object  $D_s$  has parameterization  $x^{(\partial D_s)} : [0, 2\pi] \rightarrow \mathbb{R}^2$ . If we choose  $2N_m$  discretization points on the domain  $[0, 2\pi]$ , we have  $t_m = m\pi/N_m$ , for  $m = 0, \dots, 2N_m - 1$ .

For the operators  $S_{\partial D_s, \partial D_w}$ , with  $\partial D_s \neq \partial D_w$ , since we have no singularities in the kernel, we use only the trapezoid rule to numerically approximate this problem. We obtain the following approximation:

$$\begin{aligned} S_{\partial D_s, \partial D_w} \phi(x^{(w)}) &= \frac{i}{4} \int_0^{2\pi} H_0^{(1)}(k|x^{(w)} - x^{(s)}(\tau)|) \phi(x^{(s)}(\tau)) \, d\tau \\ &\approx \frac{i}{4} \sum_{m=0}^{2N_m-1} H_0^{(1)}(k|x^{(w)} - x^{(s)}(t_m)|) \phi(x^{(s)}(t_m)). \end{aligned}$$

Using the discretization points  $x^{(\partial D_w)}(t_m)$  for  $m = 0, \dots, 2N_m - 1$  in the domain  $\partial D_w$ , we obtain the discrete operator  $\mathbf{S}_{\partial \mathbf{D}_s, \partial \mathbf{D}_w}$  with elements

$$s_{m,n}^{(s,w)} = \frac{i}{4} H_0^{(1)}(k|x^{(w)}(t_m) - x^{(s)}(t_n)|). \quad (45)$$

For the operators  $S_{\partial D_s, \partial D_s}$  and  $S_{\partial D_s, \infty}$ , we must note that their implementation is exactly equal to the implementation of the single layer operator and the far field operator of the previous section. We use  $\mathbf{S}_{\partial \mathbf{D}_s, \partial \mathbf{D}_s}$  and  $\mathbf{S}_{\partial \mathbf{D}_s, \infty}$  to represent the discrete versions of the single layer operator and the far field operator respectively.

Solving Equation (7) is equivalent to solving the system

$$\begin{bmatrix} \mathbf{S}_{\partial \mathbf{D}_1, \partial \mathbf{D}_1} & \mathbf{S}_{\partial \mathbf{D}_1, \partial \mathbf{D}_2} & \cdots & \mathbf{S}_{\partial \mathbf{D}_1, \partial \mathbf{D}_{N_D}} \\ \mathbf{S}_{\partial \mathbf{D}_2, \partial \mathbf{D}_1} & \mathbf{S}_{\partial \mathbf{D}_2, \partial \mathbf{D}_2} & \cdots & \mathbf{S}_{\partial \mathbf{D}_2, \partial \mathbf{D}_{N_D}} \\ \vdots & \vdots & \ddots & \vdots \\ \mathbf{S}_{\partial \mathbf{D}_{N_D}, \partial \mathbf{D}_1} & \mathbf{S}_{\partial \mathbf{D}_{N_D}, \partial \mathbf{D}_2} & \cdots & \mathbf{S}_{\partial \mathbf{D}_{N_D}, \partial \mathbf{D}_{N_D}} \end{bmatrix} \begin{pmatrix} \left(\frac{\partial \mathbf{u}}{\partial \nu}\right)^{(\partial \mathbf{D}_1)} \\ \left(\frac{\partial \mathbf{u}}{\partial \nu}\right)^{(\partial \mathbf{D}_2)} \\ \vdots \\ \left(\frac{\partial \mathbf{u}}{\partial \nu}\right)^{(\partial \mathbf{D}_{N_D})} \end{pmatrix} = \begin{pmatrix} \mathbf{u}^{\text{inc}}(\mathbf{x}^{(\partial \mathbf{D}_1)}) \\ \mathbf{u}^{\text{inc}}(\mathbf{x}^{(\partial \mathbf{D}_2)}) \\ \vdots \\ \mathbf{u}^{\text{inc}}(\mathbf{x}^{(\partial \mathbf{D}_{N_D})}) \end{pmatrix} \quad (46)$$

where  $\left(\frac{\partial \mathbf{u}}{\partial \nu}\right)^{(\partial \mathbf{D}_s)}$  and  $\mathbf{u}^{\text{inc}}(\mathbf{x}^{(\partial \mathbf{D}_s)})$ , for  $s = 0, \dots, N_D$ , represent respectively the normal derivative of the field and the incident field at  $\mathbf{x}^{(\partial \mathbf{D}_s)} = (x^{(\partial \mathbf{D}_s)}(t_0), x^{(\partial \mathbf{D}_s)}(t_1), \dots, x^{(\partial \mathbf{D}_s)}(t_{2N_m-1}))$  on the objects  $D_s$ . Solving (46), we obtain the value of the normal derivative of the field on the boundary of the objects  $D_s$  at the discretization points.

Using the value of the normal derivative at the discretization points of the objects  $D_s$ , we find the far field at the points  $\hat{x}_l$ ,  $l = 1, \dots, N_{ff}$  by solving

$$\mathbf{u}_\infty(\hat{\mathbf{x}}) = [\mathbf{S}_{\partial \mathbf{D}_1, \infty} \quad \mathbf{S}_{\partial \mathbf{D}_2, \infty} \quad \cdots \quad \mathbf{S}_{\partial \mathbf{D}_{N_D}, \infty}] \begin{pmatrix} \left(\frac{\partial \mathbf{u}}{\partial \nu}\right)^{(\partial \mathbf{D}_1)} \\ \left(\frac{\partial \mathbf{u}}{\partial \nu}\right)^{(\partial \mathbf{D}_2)} \\ \vdots \\ \left(\frac{\partial \mathbf{u}}{\partial \nu}\right)^{(\partial \mathbf{D}_{N_D})} \end{pmatrix}, \quad (47)$$

where  $\mathbf{u}_\infty(\hat{\mathbf{x}}) = (u_\infty(\hat{x}_1), u_\infty(\hat{x}_2), \dots, u_\infty(\hat{x}_{N_{ff}}))$ .

# Chapter 4

## Numerical solution of the inverse problem at low frequencies

### 4.1 Inverse scattering problem for a single frequency

After introducing the direct scattering problem, we now focus on the main topic of this thesis, which is the solution of the inverse scattering problem.

In Chapter 2, we presented the continuous inverse scattering problem of the reconstruction of the object  $\partial D$  using the far field pattern in  $\Omega$ . In real life, we do not have the far field pattern data for the entire circle  $\Omega$ , as the far field data is measured at only a finite number of points on  $\Omega$ . We use that data to construct a system of equations to approximately solve our problem of finding the shape of the object  $D$ . We rephrase our problem for a single frequency as:

**Problem 1** *Given the  $N_{ff}$  measures  $u_\infty(\hat{x}_l)$  of the far field pattern at the points  $\hat{x}_l \in \Omega$ , for  $l = 1, \dots, N_{ff}$ , where  $\Omega$  is the unit circle, obtained from a plane wave of fixed incidence direction  $d$  wavenumber  $k$  reflecting from an object  $D$ , reconstruct the shape of the object  $D$ . Homogeneous Dirichlet boundary conditions are assumed on  $\partial D$ .*

#### 4.1.1 Implementation of Method B

We use Method B in this thesis instead of Method A. As we pointed out in Section 2.2.4, Method B has better computational performance than Method A.

We point out here that in this thesis, we will use bold face to represent discrete quantities like matrices and vectors: for example, the discrete counterpart of the operator  $S_{x_r^{(j)}}$  will be the matrix  $\mathbf{S}_{x_r^{(j)}}$ . We now focus on the numerical implementation of the two-step procedure of Method B.

For the first step, where we solve Equation (3) for  $\psi$ , we discretize the domain  $[0, 2\pi]$  uniformly with the points  $t_m = m\pi/N_m$ . We calculate the single layer discrete operator,

which is the matrix  $\mathbf{S}_{\mathbf{x}_r^{(j)}}$ , and the right hand side  $\mathbf{u}^{\text{inc}}(\mathbf{x}^{(j)})$  of Equation (3) at the vector  $\mathbf{x}^{(j)} = (x^{(j)}(t_1), \dots, x^{(j)}(t_{N_m}))$  in the same way as in Chapter 2. With the matrix  $\mathbf{S}_{\mathbf{x}_r^{(j)}}$  and vector  $\mathbf{u}^{\text{inc}}(\mathbf{x}^{(j)})$ , we solve the linear system for  $\psi(\mathbf{x}^{(j)})$ :

$$\mathbf{S}_{\mathbf{x}_r^{(j)}} \psi(\mathbf{x}^{(j)}) = \mathbf{u}^{\text{inc}}(\mathbf{x}^{(j)}), \quad (48)$$

where  $\psi(\mathbf{x}^{(j)})|(\mathbf{x}^{(j)})'$  is the vector with components

$$(\psi(x^{(j)}))_m = \frac{\partial u}{\partial \nu}(x^{(j)}(t_m)) \sqrt{[(x_1^{(j)})']^2(t_m) + [(x_2^{(j)})']^2(t_m)}.$$

Summarizing, the first step in our procedure is:

**Step 1:** Solve for  $\psi(\mathbf{x}^{(j)})$  the linear system

$$\mathbf{S}_{\mathbf{x}_r^{(j)}} \psi(\mathbf{x}^{(j)}) = \mathbf{u}^{\text{inc}}(\mathbf{x}^{(j)}). \quad (49)$$

For the second step, as was described in Chapter 2, we must iteratively solve the following equation:

$$\left( \lambda^{(j)} I^p + (S'_{x_r^{(j)}, \infty})^* S'_{x_r^{(j)}, \infty} \right) h_r = (S'_{x_r^{(j)}, \infty})^* \left( S_{x_r^{(j)}, \infty} \frac{\partial u}{\partial \nu} - u_\infty \right) \quad (50)$$

to obtain the coefficients of the update polynomial  $h_r$ .

The term  $\left( S_{x_r^{(j)}, \infty} \frac{\partial u}{\partial \nu} - u_\infty \right)$  on the right hand side of (50) is calculated in the same way as shown in Chapter 3.

To implement the operator  $S'_{x_r^{(j)}, \infty}$ , we have  $N_{ff}$  equations of the same type as (50), one for each of the far field pattern measurements of the object and the object update function  $h \in \mathbb{X}_{N_r}$ . The discrete analogue of this operator is thus an  $N_{ff} \times N_r$  matrix (not necessarily square) with complex entries.

For the case when  $\mathbb{X}_{N_r}$  is the space of trigonometric polynomials, we solve for the coefficients  $a_0, \dots, a_{N_r}, b_1, \dots, b_{N_r}$  of  $h_r(t)$ . For the case when  $\mathbb{X}_{N_r}$  is the space of B-splines, we look for the coefficients  $c_0, \dots, c_{N_r}$  of  $h_r(t)$ .

To implement the operator  $\left( S_{x_r^{(j)}, \infty} \right)' h_r$  numerically, we use the same uniform discretization of the domain  $[0, 2\pi]$  as before for the single layer operator. After all the calculations, we obtain the discrete approximation

$$S'_{x_r^{(j)}, \infty} h_r \approx \mathbf{S}'_{\mathbf{x}_r^{(j)}, \infty} \mathbf{h}_r, \quad (51)$$

where  $\mathbf{S}'_{\mathbf{x}_r^{(j)}, \infty} \mathbf{h}_r$  is the discrete version of the operation  $\left[ S'_{x_r^{(j)}, \infty} h_r \right]$ , and  $\mathbf{h}_r$  is the vector of coefficients of the polynomial  $h_r(t)$ . We abuse notation by calling this discrete operator  $\mathbf{S}'_{\mathbf{x}_r^{(j)}, \infty}$ , and this does not mean that we are taking the derivative of the discrete operator. The use of this notation is to remind the reader that this operator is the discretization of the operator  $S'_{x_r^{(j)}, \infty}$ .

We have for each  $\hat{x}_l$ ,  $l = 1, \dots, N_{ff}$ , that

$$\begin{aligned} \left[ S'_{x^{(j)}, \infty} h \right] (\hat{x}_l) &\approx ik \frac{e^{i\pi/4} \pi}{N_m \sqrt{8\pi k}} \sum_{m=1}^{N_m} e^{-ik\hat{x}_l \cdot x^{(j)}(t_m)} \psi(t_m) \hat{x}_l \cdot h(t_m) \\ &= \frac{e^{i3\pi/4}}{N_m} \sqrt{\frac{k\pi}{8}} \sum_{m=1}^{N_m} S_m \hat{x}_l \cdot h(t_m), \end{aligned}$$

where  $S_m = e^{-ik\hat{x}_l \cdot x^{(j)}(t_m)} \psi(t_m)$ .

For the case when  $\mathbb{X}_{N_r}$  is the space of trigonometric polynomials, we insert the values of  $h_r(t_m)$  into the last equation and obtain

$$\begin{aligned} \left[ S'_{x_r, \infty} h_r \right] (\hat{x}_l) &\approx \frac{e^{i3\pi/4}}{N_m} \sqrt{\frac{k\pi}{8}} \sum_{m=1}^{N_m} S_m (\hat{x}_{l,1} \cos(t_m) + \hat{x}_{l,2} \sin(t_m)) \left[ a_0 + \sum_{n=1}^{N_r} (a_n \cos(nt_m) + b_n \sin(nt_m)) \right] \\ &= \frac{e^{i3\pi/4}}{N_m} \sqrt{\frac{k\pi}{8}} \left[ A_0 a_0 + \sum_{n=1}^{N_r} (A_n a_n + B_n b_n) \right], \end{aligned}$$

where  $\hat{x}_l = (\hat{x}_{l,1}, \hat{x}_{l,2})$ , and the coefficients  $A_0$ ,  $A_n$ , and  $B_n$  are:

$$\begin{aligned} A_0 &= \sum_{m=1}^{N_m} S_m (\hat{x}_{l,1} \cos(t_m) + \hat{x}_{l,2} \sin(t_m)), \\ A_n &= \sum_{m=1}^{N_m} S_m (\hat{x}_{l,1} \cos(t_m) + \hat{x}_{l,2} \sin(t_m)) \cos(nt_m), \\ B_n &= \sum_{m=1}^{N_m} S_m (\hat{x}_{l,1} \cos(t_m) + \hat{x}_{l,2} \sin(t_m)) \sin(nt_m), \end{aligned}$$

for  $n = 1, \dots, N_r$ .

For the case when  $\mathbb{X}_{N_r}$  is the space of B-splines, we insert the values of  $h(t_m)$  into the last equation, and obtain

$$\begin{aligned} \left[ S'_{x_r, \infty} h_r \right] (\hat{x}_l) &\approx \frac{e^{i3\pi/4}}{N_m} \sqrt{\frac{k\pi}{8}} \sum_{m=1}^{N_m} S_m (\hat{x}_{l,1} \cos(t_m) + \hat{x}_{l,2} \sin(t_m)) \left( \sum_{n=1}^{N_r} c_n N_n^q(t_m) \right) \\ &= \frac{e^{i3\pi/4}}{N_m} \sqrt{\frac{k\pi}{8}} \left( \sum_{n=1}^{N_r} C_n c_n \right), \end{aligned}$$

where  $\hat{x}_l = (\hat{x}_{l,1}, \hat{x}_{l,2})$  and the coefficients  $C_n$  are:

$$C_n = \sum_{m=1}^{N_m} S_m (\hat{x}_{l,1} \cos(t_m) + \hat{x}_{l,2} \sin(t_m)) N_n^q(t_m),$$

for  $n = 1, \dots, N_r$ .

Although the discrete approximation (51) is a complex matrix, the components of the vector  $\mathbf{h}_r$  must all be real. Then we must consider the real and imaginary part of this operator, and from this we conclude that in reality we have  $2N_{ff}$  rows. We obtain the matrix

$$\begin{bmatrix} \operatorname{Re} \left( \mathbf{S}'_{\mathbf{x}_r^{(j)}, \infty} \right) \\ \operatorname{Im} \left( \mathbf{S}'_{\mathbf{x}_r^{(j)}, \infty} \right) \end{bmatrix} \mathbf{h}_r,$$

where  $\operatorname{Re} \left( \mathbf{S}'_{\mathbf{x}_r^{(j)}, \infty} \right)$  and  $\operatorname{Im} \left( \mathbf{S}'_{\mathbf{x}_r^{(j)}, \infty} \right)$  are respectively the real and imaginary parts of  $\mathbf{S}'_{\mathbf{x}_r^{(j)}, \infty}$ .

The operator  $\left( \mathbf{S}'_{x_r^{(j)}, \infty} \right)^*$  is obtained by taking the conjugate of the matrix  $\mathbf{S}'_{\mathbf{x}_r^{(j)}, \infty}$ , and we separate the imaginary and real parts the same way we did with  $\mathbf{S}'_{x_r^{(j)}, \infty}$  to obtain

$$\begin{bmatrix} \operatorname{Re} \left( \mathbf{S}'_{\mathbf{x}_r^{(j)}, \infty} \right)^\top & \operatorname{Im} \left( \mathbf{S}'_{\mathbf{x}_r^{(j)}, \infty} \right)^\top \end{bmatrix}.$$

Since the operator  $\mathbf{S}'_{x_r^{(j)}, \infty}$  is ill-posed, the system is ill conditioned, and we need to apply a regularization scheme. To overcome the problem of ill-posedness, we use a penalty term  $\lambda \mathbf{I}^p$ , where  $\mathbf{I}^p$  is the matrix obtained by discretizing the norm of the solution  $h(t) = h_r(t)(\cos(t), \sin(t))$  in the Hilbert space  $H^p([0, 2\pi])$ , where  $p$  is an integer. We calculate the matrix  $\mathbf{I}^p$  as the discretization of the norm of the solution, which in this case is:

$$\begin{aligned} \|h\|_{H^p([0, 2\pi])}^2 &= \sum_{j=0}^p \|D^j h\|_{L^2([0, 2\pi])}^2 \\ &= \sum_{j=0}^p \left[ \int_0^{2\pi} \left( \frac{d^j h(\tau)}{d\tau^j} \cdot \frac{d^j h(\tau)}{d\tau^j} \right) d\tau \right]. \end{aligned}$$

The matrix  $\mathbf{I}^p$  depends on the solution space that we choose. For the special case that we choose  $p = 1$  and  $h_r(t)$  is a trigonometric polynomial, the mass matrix becomes a diagonal matrix with elements  $h_{11} = 2\pi$ ,  $h_{nn} = \pi(1 + (n-1)^2)$  for  $n = 2, \dots, N_r + 1$ , and  $h_{nn} = \pi(1 + (n - N_r - 1)^2)$  for  $n = N_r + 2, \dots, 2N_r + 1$ .

For the case that  $h_r(t)$  is represented by B-splines, the mass matrix has a different structure. The matrix is a symmetric Toeplitz matrix. The elements  $m_{ij}$  of the matrix  $\mathbf{H}^1$

are

$$m_{ij} = \int_0^{2\pi} N_i^q(\tau)N_j^q(\tau) d\tau + \int_0^{2\pi} (N_i^q(\tau))'(N_j^q(\tau))' d\tau.$$

Since the functions  $N_i^q(\tau)$  have local compact support, the configuration of the  $N_r \times N_r$  matrix  $\mathbf{I}^1$  will depend on the order of the splines  $N_i^q$  used to represent  $h_r(t)$ . If  $N_i^q$  is of order  $q$ , each row of the matrix will have  $q + 2$  nonzero elements. In particular,

$$m_{ij} = \begin{cases} 0, & \text{for } N_i^q(t)N_j^q(t) = 0 \\ \int_0^{2\pi} N_i^q(\tau)N_j^q(\tau) d\tau + \int_0^{2\pi} (N_i^q(\tau))'(N_j^q(\tau))' d\tau, & \text{otherwise.} \end{cases}$$

In Figure (4.1), we present the matrix  $\mathbf{I}^1$  for a fixed number of coefficients  $N_r = 20$  and varying order  $q$ .

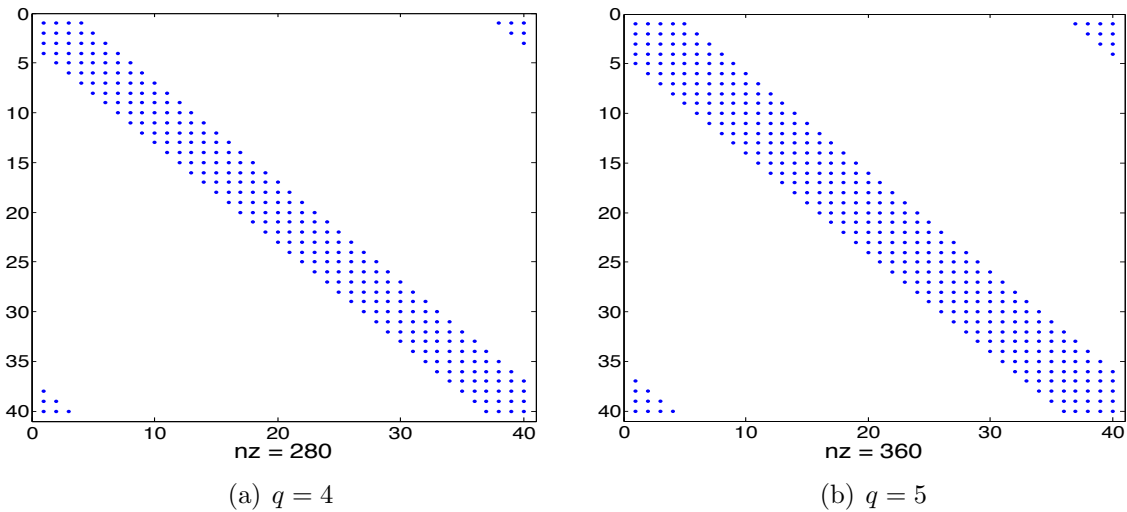


Figure 4.1: Matrix  $\mathbf{I}^1$  for a fixed number of coefficients  $N_r = 40$  and varying order  $q$ . (a)  $q = 4$ . (b)  $q = 5$ . Each dot represents a nonzero element, and where there are no dots, the matrix entries are filled by zeros.

Finally, we solve the following equation to find  $\mathbf{h}_r$ :

$$\mathbf{h}_r = \mathbf{R}\mathbf{b}, \tag{52}$$

where the regularization scheme is

$$\mathbf{R} = \left( \lambda \mathbf{I}^P + \begin{bmatrix} \text{Re} \left( \left( \mathbf{S}'_{\mathbf{x}_r^{(j)}, \infty} \right) \right)^\top & \text{Im} \left( \left( \mathbf{S}'_{\mathbf{x}_r^{(j)}, \infty} \right) \right)^\top \end{bmatrix} \begin{bmatrix} \text{Re} \left( \left( \mathbf{S}'_{\mathbf{x}_r^{(j)}, \infty} \right) \right) \\ \text{Im} \left( \left( \mathbf{S}'_{\mathbf{x}_r^{(j)}, \infty} \right) \right) \end{bmatrix} \right)^{-1},$$

and the residue  $\mathbf{b}$  is the vector

$$\mathbf{b} = \begin{bmatrix} \text{Re} \left( \left( \mathbf{S}'_{\mathbf{x}_r^{(j)}, \infty} \right) \right)^\top & \text{Im} \left( \left( \mathbf{S}'_{\mathbf{x}_r^{(j)}, \infty} \right) \right)^\top \end{bmatrix} \begin{bmatrix} \text{Re} \left( u_\infty - S_{x_r^{(j)}, \infty} \psi \right) \\ \text{Im} \left( u_\infty - S_{x_r^{(j)}, \infty} \psi \right) \end{bmatrix},$$

where  $\lambda$  is the regularization parameter and  $\mathbf{IP}$  is the semi-norm matrix of order  $p$ .

We solve Equation (52) to obtain the coefficients for  $h_r(t)$ . We then update the domain  $x_r^{(i)}(t) + \rho h_r(t)$  using a scaling factor that can be obtained as pointed out in the Section 2.2.5.

Unfortunately, there is no guarantee that the new domain obtained is in our set of possible domains  $\mathbb{X}_{N_r}$ , which in our case is the set of parameterizations of star-shaped domains. There are different ways to try to ensure that the solution lies in the solution space  $\mathbb{X}_{N_r}$ . We choose to approximately project the solution  $x_r^{(i)}(t) + \rho h_r(t)$  into the space  $\mathbb{X}_{N_r}$ . To do this we will use a quasi-projection operator  $P_{\mathbb{X}_{N_r}} : C^2(\partial D) \rightarrow \mathbb{X}_{N_r}$ . There are different ways to implement the quasi-projection operator. We present a way that is independent of the basis functions chosen for the space  $\mathbb{X}_{N_r}$  and another that is more specifically for the case when we use B-splines as a basis for the solution space. In the latter case, the quasi-projection operator is a projection operator.

Suppose  $\mathbf{x}_r$  is the vector of coefficients of the trigonometric polynomial  $x_r$  for the approximation domain.

1. Quasi-projection for trigonometric polynomials:

- (a) Choose  $N_{\text{proj}}$  points to use for the projection of the domain. It is important to choose a large value for  $N_{\text{proj}}$ , since choosing a small value may cause this algorithm to not work properly. Discretize the interval  $[0, 2\pi]$  uniformly with points  $t_\ell = 2\ell\pi/N_{\text{proj}}$ .
- (b) Using the vector  $\mathbf{x}_r^{(j)}$ , calculate the values of the function  $x_r^{(j)}(t)$  at the discretization points  $t_\ell$ , obtaining the vector  $\mathbf{x}_p$  with components  $x_{p,\ell} = x_r^{(j)}(t_\ell)$ .
- (c) If all of the components of  $\mathbf{x}_p$  exceed a threshold value  $x_{\min}$  then
  - Accept the domain with parameterization  $x(t) = x_r^{(j)}(\cos(t), \sin(t))$ .
- (d) Else
  - Take the components of the vector  $\mathbf{x}_p$  that are less than  $x_{\min}$ , make those components equal to  $x_{\min}$  and call this new vector  $\tilde{\mathbf{x}}_p$ .
  - Consider the matrix  $\mathbf{A}$  such that each element  $a_{\ell m}$  of  $\mathbf{A}$  is

$$a_{\ell m} = \begin{cases} 1 & \text{for } m = 1 \\ \cos((m-1)t_\ell) & \text{for } m = 2, \dots, N_r + 1 \\ \sin((m - (N_r + 1))t_\ell) & \text{for } m = N_r + 2, \dots, 2N_r + 1 \end{cases}$$

where  $t_\ell$  are the discretization points. We have that  $\mathbf{A}\tilde{\mathbf{x}}_p = \mathbf{x}_p$ .

- Solve for  $\tilde{\mathbf{x}}_{\mathbf{r}}$  the system

$$\mathbf{A}'\mathbf{A}\tilde{\mathbf{x}}_{\mathbf{r}} = \mathbf{A}'\mathbf{x}_{\mathbf{p}}. \quad (53)$$

- Set the vector of coefficients of the solution as the vector  $\tilde{\mathbf{x}}_{\mathbf{r}}$ . The components of this vector become the coefficients of the new trigonometric polynomial  $x_r^{(j)}$ , and we obtain the new parameterization  $x^{(j)} = x_r^{(j)}(\cos(t), \sin(t))$ .

We call this procedure trigonometric quasi-projection and will define the operator  $P_{\mathbb{X}_{N_r}, T} : C([0, 2\pi]) \rightarrow \mathbb{X}_{N_r}$  as the operator that applies this procedure to a parameterization  $x(t) = x_r(t)(\cos(t), \sin(t))$ .

**Remark 4.1.1** *We can use the quasi-projection in solution spaces with any type of basis functions, not only trigonometric polynomials. In this case, we just need to change the matrix  $\mathbf{A}$  for the chosen basis functions. For example, this procedure also works with B-spline basis functions. However, we have a better procedure to use with B-splines that we present next.*

## 2. Projection for B-splines:

- (a) If all of the components of the coefficient vector  $\mathbf{x}_{\mathbf{r}}^{(j)}$  exceed a threshold value  $x_{\min}$  then
  - Accept the domain with coefficients vector  $\mathbf{x}_{\mathbf{r}}^{(j)}$ .
- (b) Else
  - Take the components of the vector  $\mathbf{x}_{\mathbf{r}}^{(j)}$  that are less than  $x_{\min}$ , make those components equal to  $x_{\min}$  and call this new vector  $\tilde{\mathbf{x}}_{\mathbf{r}}^{(j)}$ .
  - Let  $\tilde{\mathbf{x}}_{\mathbf{r}}$  be the vector of coefficients of the solution. The components of this vector become the coefficients of the new B-spline  $x_r^{(j)}$ , and we obtain the parameterization  $x^{(j)} = x_r^{(j)}(\cos(t), \sin(t))$ .

We call this procedure projection for B-splines and will define the operator  $P_{\mathbb{X}_{N_r}, B} : C([0, 2\pi]) \rightarrow \mathbb{X}_{N_r}$  as the operator that applies this procedure to a parameterization  $x^{(j)}(t) = x_r^{(j)}(t)(\cos(t), \sin(t))$ .

Summarizing, the second step in our procedure is:

**Step 2:** Repeat until stopping criteria are reached:

- Solve for  $\mathbf{h}_r$  the linear system

$$\mathbf{h}_r = \mathbf{R}\mathbf{b},$$

where

$$\mathbf{R} = \left( \lambda \mathbf{I}^p + \begin{bmatrix} \text{Re}(\mathbf{S}'_{\mathbf{x}_r^{(j)}, \infty})^\top & \text{Im}(\mathbf{S}'_{\mathbf{x}_r^{(j)}, \infty})^\top \end{bmatrix} \begin{bmatrix} \text{Re}(\mathbf{S}'_{\mathbf{x}_r^{(j)}, \infty}) \\ \text{Im}(\mathbf{S}'_{\mathbf{x}_r^{(j)}, \infty}) \end{bmatrix} \right)^{-1}$$

and

$$\mathbf{b} = \begin{bmatrix} \text{Re}(\mathbf{S}'_{\mathbf{x}_r^{(j)}, \infty})^\top & \text{Im}(\mathbf{S}'_{\mathbf{x}_r^{(j)}, \infty})^\top \end{bmatrix} \begin{bmatrix} \text{Re}(u_\infty - S_{x_r^{(j)}, \infty} \psi) \\ \text{Im}(u_\infty - S_{x_r^{(j)}, \infty} \psi) \end{bmatrix}.$$

- Using  $P_{\mathbb{X}_{N_r}} = \{P_{\mathbb{X}_{N_r}, T} \text{ on } P_{\mathbb{X}_{N_r}, B}\}$ , update the parameterization of the domain  $x_r^{(j)} = P_{\mathbb{X}_{N_r}}(x_r^{(j)} + h_r)$ , with the appropriate projection for the solution space used.

There are different stopping criteria that may be used here, among which are:

- The number of iterations realized. Sometimes we would like to stop our procedure after a certain number of iterations in order to conserve time and resources;
- The magnitude of the residue vector  $(u_\infty - S_{x_r^{(j)}, \infty} \psi)$  reaches a value  $\epsilon_1$ , which means that we obtain our result up to a certain tolerance  $\epsilon_1$ ;
- The difference between the residue on two consecutive steps decreases at a rate smaller than a value  $\epsilon_2$ . This means that our method is taking too long to provide a desired answer if it is going to provide an answer at all.

There are other variations of stopping criteria based on these ideas that can be used in this problem; for more details look at [19] or [20].

We implement a combination of all of the above stopping criteria for our method in this step. After we reach our stopping criteria, we set the new approximation of the domain as  $x^{(j+1)}$ . We then repeat steps 1 and 2 to obtain a new approximation of the domain until a

general stopping criterion is reached. We summarize Method B, an alternative implementation of Johansson and Sleeman's method, in Algorithm 4.1.1.

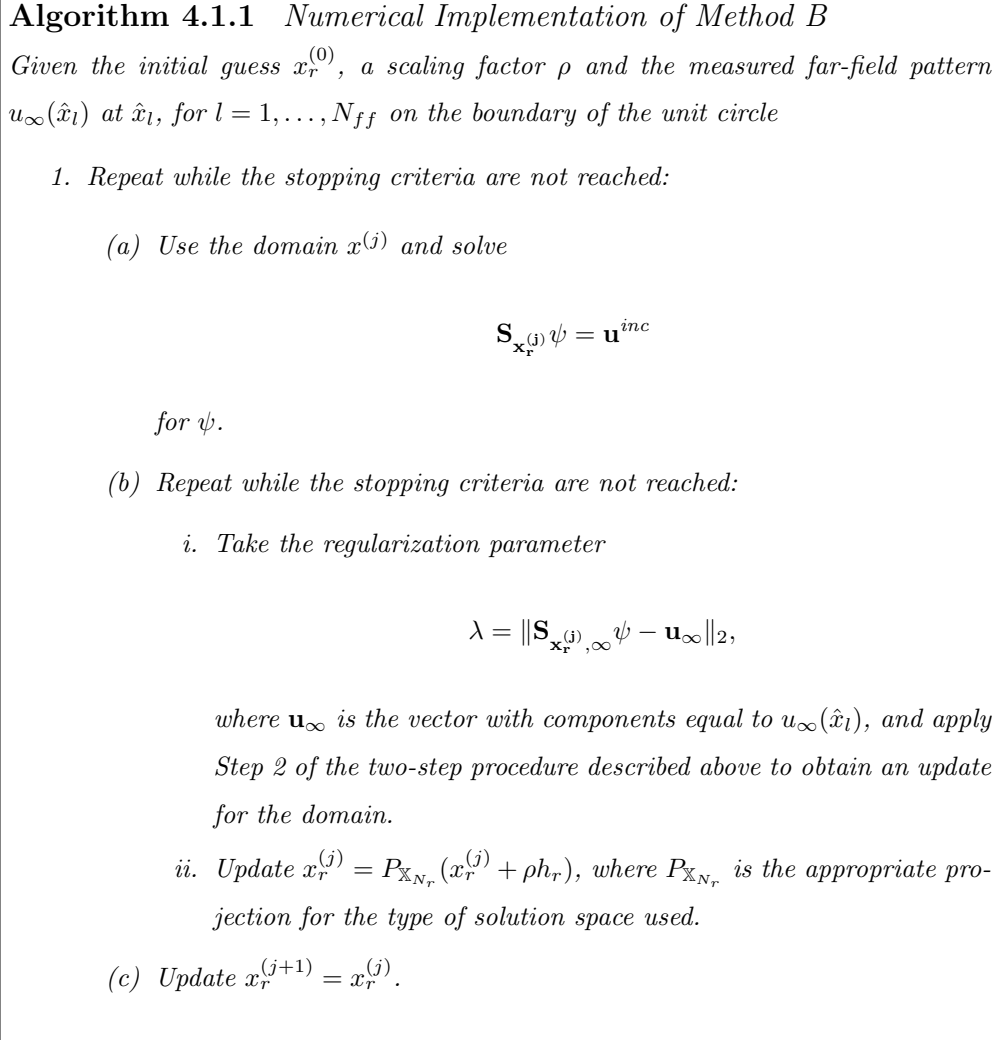


Figure 4.2: Implementation of Method B described in Chapter 2 for solving the inverse problem for an object  $D$  with Dirichlet boundary conditions using single frequency far field pattern measures.

**Remark 4.1.2** We choose the order of the penalty term to be  $p = 1$  in our implementation, which means that our matrix  $\mathbf{I}^1$  is equivalent to the  $H^1([0, 2\pi])$ . It is possible to choose  $p = 0$ , which would be equivalent to the  $L^2([0, 2\pi])$  norm.

**Remark 4.1.3** We choose  $\lambda$  equal to the  $L^2$ -norm of the residue vector. In this case, we should be careful to not allow the value of  $\lambda$  to grow too much.

**Remark 4.1.4** In [47], the authors propose to choose the regularization parameter  $\lambda$  equal to the  $L^2$ -norm of the residue in Equation (3).

**Remark 4.1.5** In [18], the authors propose taking  $\lambda$  to be the  $L^2$ -norm of the residue to a power of  $\mu$ , where  $\mu$  takes different integer values. In [23] and other works, the use of a constant value was proposed.

**Remark 4.1.6** One can also use the Levenberg-Marquardt hooking step to choose  $\lambda$ . In this case, we choose an initial  $\lambda$  and an  $\epsilon_\lambda$ -neighborhood of  $\lambda$  to look for the best  $\lambda$  that would minimize the residue at each step. There are different ways to implement this; see [19; 20].

**Remark 4.1.7** For some of our examples, we choose the scaling factor  $\rho$  equal to 1 in our implementation of the method. Other choices are possible; see [18]. For other examples we apply the globalization techniques of Chapter 2. We must keep in mind that if we choose a value too small for the scaling factor  $\rho$ , the method takes more time to converge and if we take a value too large, the method may take longer, or may not converge at all.

## 4.1.2 Numerical results

We present some examples illustrating the implementation of a method for solving the inverse scattering problem for a single frequency. We choose the examples to illustrate the influence of the initial guess, the shape of the object that we are reconstructing, the wavenumber of the incident plane wave, and the solution space used. For all the examples presented in this chapter, we considered the  $H^1$ -penalty term.

### Example 4.1.1 (Comparison of Methods A and B)

We compare the results of the Methods A and B for the reconstruction of the object D with parameterization

$$x(t) = (2 + 0.3 \cos(3t))(\cos(t), \sin(t)), \quad (54)$$

which we from now on call the ‘‘Pear’’.

We consider different scenarios for our comparison of Methods A and B. In all the scenarios considered, we have an incident wave with wavenumber  $k$  and incidence direction  $d$ . The far field data was measured at points uniformly distributed over the circle  $\hat{x}_l = (\cos(\theta_l), \sin(\theta_l))$ , for  $\theta_l = 2(l - 1)\pi/N_{ff}$ ,  $l = 1, \dots, N_{ff}$ , with  $N_{ff} = 32$ . We look for the solution in the space

$$\mathbb{X}_{N_r} = \left\{ x_r(t) : x_r(t) = a_0 + \sum_{m=1}^{N_r} (a_m \cos(mt) + b_m \sin(mt)), \quad x_r(0) = x_r(2\pi), \quad x_r(t) > x_{\min} \right\},$$

where  $N_r = 5$  and  $x_{\min} > 0$ . The stopping criteria used for both methods are

$$\|S_{\infty, x^{(j)}}\psi - u_{\infty}\|_2 < \epsilon \quad (55)$$

and

$$\left| \|S_{\infty, x^{(j)}}\psi - u_{\infty}\|_2 - \|S_{\infty, x^{(j-1)}}\psi - u_{\infty}\|_2 \right| < 10^{-6}. \quad (56)$$

We use the the stopping criterion (55) to control the absolute value of the error in the approximation of the far field pattern. The stopping criterion (56) is used to ensure that our iterations advance toward the solution at a reasonable rate.

For this example, we use wavenumbers  $k = 1$  and  $k = 3$  and different incidence directions  $d = n_d\pi/4$ , where  $n_d = 0, 1, \dots, 4$ . For the wavenumber  $k = 1$  in all incidence directions, we use as an initial guess the circle with radius 0.1 centered at the origin, and the stopping criterion  $\epsilon = 0.25$ . For the wavenumber  $k = 3$  in all incidence directions, we use as an initial guess the circle with radius 1.8 centered at the origin, and the stopping criterion  $\epsilon = 0.8$ . Throughout this thesis, we use  $x_{\min}$  equal to the radius of the initial guess. Below these tolerance values, we start to have problems with convergence of the algorithm.

In Table 4.1, we present the number of iterations of the two-step procedure and the CPU time in seconds necessary for obtaining the solution of the problem using Methods A and B, with stopping criteria (55) and (56). For Method A this means that for each two-step procedure iteration we solve the system in (49) and the system in (52) each once. For Method B, we include in parentheses the number of inner iterations for the the solution of Equation (52). The number of iterations outside parentheses is the number of times that we solve the system in (49), and the number inside parentheses is the number of times that we solve the system in (52). The approximate solutions obtained with both methods were similar.

To calculate the CPU time in seconds, we ran the algorithms with the same conditions 10 times each and took the average time spent to execute the program. We used a computer with a 2.4 GHz Intel Core i7 processor and 8 GB RAM for the simulations.

As expected, Method B requires in general fewer iterations of Equation (49) than Method A. Consequently, Method B requires less CPU time than Method A. This is an advantage since the system in (49) is larger than the system in (52) and consequently its solution requires a greater number of operations.

In Figure 4.3, we present the plot of the residue as a function of the number of iterations for Methods A and B for each of the scenarios in our example. The residue is calculated before the two-step procedure in each iteration. Each curve in each figure represents the residues for a problem with incidence direction  $d$ . In Figure 4.3(a), we have the result using Method A with  $k = 1$ . Since the number of iterations for Method A with  $k = 1$  is very high,

k	Radius	$\epsilon$	Direction $d$	Method A		Method B	
				Iterations	CPU time	Iterations	CPU time
1	0.1	0.25	0	217	143.41	10(34)	5.53
			$\pi/4$	26	16.64	11(38)	6.23
			$\pi/2$	160	109.30	13(43)	7.77
			$3\pi/4$	313	210.01	22(58)	12.63
			$\pi$	21	14.2	8(33)	4.82
3	1.8	0.8	0	4	7.14	6(19)	11.03
			$\pi/4$	6	10.49	3(10)	5.44
			$\pi/2$	6	10.73	5(14)	9.60
			$3\pi/4$	5	9.10	5(15)	8.94
			$\pi$	5	8.96	3(10)	5.40

Table 4.1: We compare the number of iterations and CPU time in seconds needed for Methods A and B to obtain the solution for the Dirichlet scattering problem using the incident plane wave with wavenumbers  $k = 1$  and  $k = 3$ , and incidence direction  $d = n_d\pi/4$ , where  $n_d = 0, 1, \dots, 4$ . For the wavenumber  $k = 1$  in all incident directions, we use as initial guess the circle with radius 0.1 and  $\epsilon = 0.25$ , and for the wavenumber  $k = 3$  in all incident directions, we use as initial guess the circle with radius 1.8 and  $\epsilon = 0.8$ . The number of iterations for each method is presented with the respective average CPU time in seconds. For Method B, the number of iterations necessary for the inner loop is in parenthesis.

we used in this plot the log-10 scale on the  $x$ -axis. The result for Method B with  $k = 1$  is in Figure 4.3(b). The result for Method A with  $k = 3$  is in Figure 4.3(c). The result for Method B with  $k = 3$  is in Figure 4.3(d).

#### Example 4.1.2 (Comparison of B-spline and trigonometric polynomial solution spaces)

In this example we use Method B to solve the inverse problem for different objects using two different solution spaces; the space of B-spline polynomials and the space of trigonometric polynomials. We compare the solutions obtained by the two types of solution space. The solution space of trigonometric polynomials is

$$\mathbb{X}_{N_r^{(1)}}^{(1)} = \left\{ x_r(t) : x_r(t) = a_0 + \sum_{m=1}^{N_r} (a_m \cos(mt) + b_m \sin(mt)), \quad x_r(0) = x_r(2\pi), \quad x_r(t) > x_{\min} \right\},$$

with  $N_r^{(1)}$  being the number of modes in the trigonometric polynomial, and the solution space of B-splines is

$$\mathbb{X}_{N_r^{(2)}}^{(2)} = \left\{ r(t) : r(t) = \sum_{m=1}^{N_r} c_m N_m^q(t), \quad x_r(0) = x_r(2\pi), \quad x_r(t) > x_{\min} \right\},$$

with  $N_r^{(2)}$  being the number of basis functions (which is equal to the number of knots used for describing the B-spline), and  $q$  is the degree of the B-spline. In all of the scenarios of

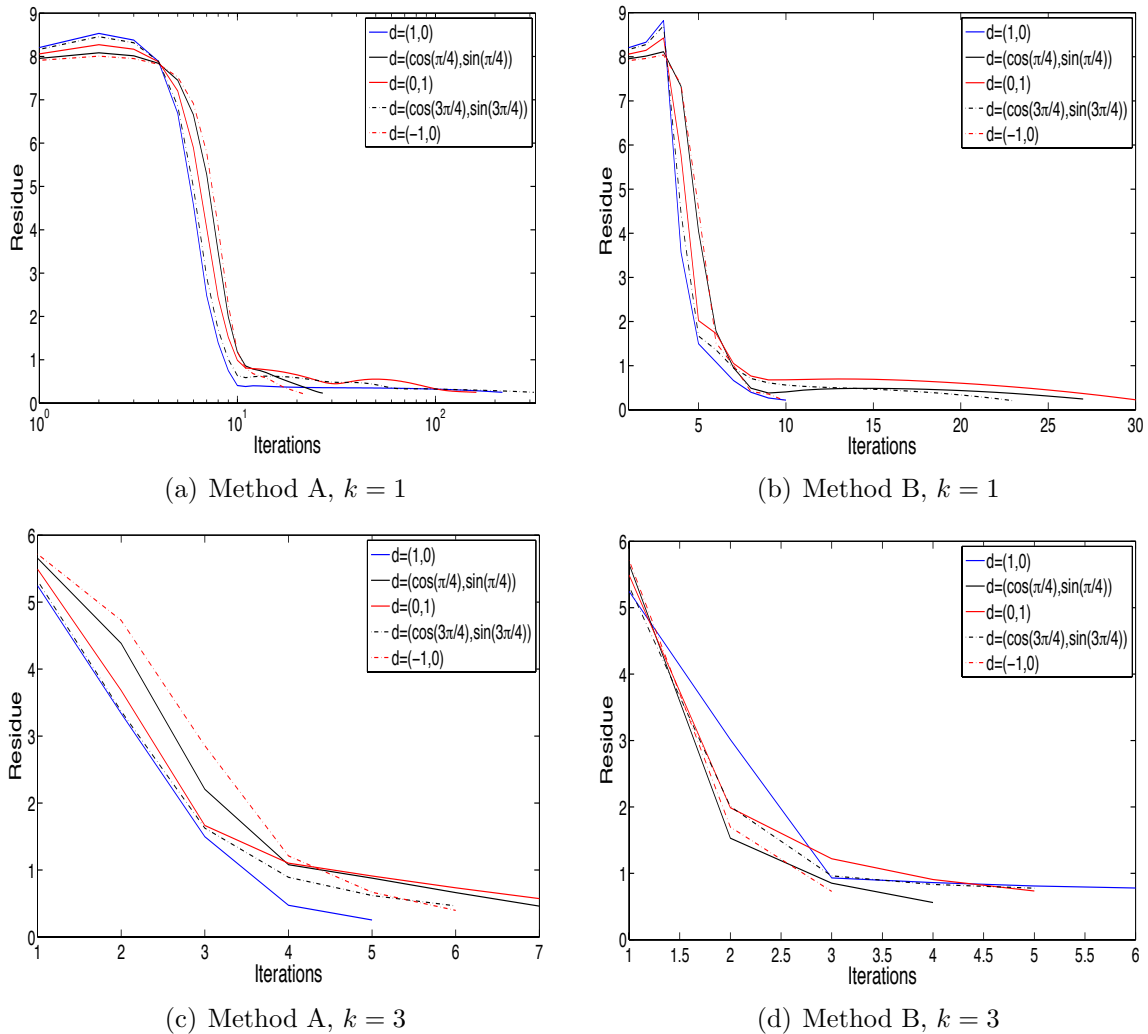


Figure 4.3: Plot of residue versus number of iterations for all the scenarios of this example. Each curve represents the residue in each iteration for the problem using an incident plane wave with wavenumber  $k$  and incidence direction  $d$  using Method A or Method B. (a) Method A with  $k = 1$ . (Note here that the  $x$ -axis is on the log-scale for only this figure.) (b) Method B with  $k = 1$ . (c) Method A with  $k = 3$ . (d) Method B with  $k = 3$ .

this example, we take  $q = 4$ .

In all of the scenarios considered in this example, we use the incident plane wave with wavenumber  $k = 1$  and incidence direction  $d$ . The far field data was measured at points uniformly distributed over the circle  $\hat{x}_l = (\cos(\theta_l), \sin(\theta_l))$ , for  $\theta_l = 2(l-1)\pi/N_{ff}$ ,  $l = 1, \dots, N_{ff}$ , with  $N_{ff} = 32$ .

We consider three scenarios:

- In the first scenario, the object that we use as a scatterer has the parameterization

$x(t) = x_r(t)(\cos(t), \sin(t))$  and  $x_r : [0, 2\pi] \rightarrow \mathbb{R}$ , with  $x_r(t) = (2 + 0.3 \cos(3t))$ . As in the last example, we call it the Pear. Note that this object is in the solution space of trigonometric polynomials. For this scenario, the direction of the incident wave is  $d = (0, 1)$ . The stopping criterion is (55) with  $\epsilon = 0.1$ . First, we try to approximate this object using trigonometric polynomials with  $N_r^{(1)} = 5$  and a circle with radius 0.1 centered at the origin as an initial guess. The result is shown in Figure 4.4(a). Later, we try to approximate this object using polynomials of B-splines with  $N_r^{(2)} = 12$  and a circle with radius 0.1 centered at the origin as an initial guess. The result is shown in Figure 4.4(b).

- In the second scenario, the object that we use as a scatterer has the parameterization  $x(t) = x_r(t)(\cos(t), \sin(t))$  and  $x_r : [0, 2\pi] \rightarrow \mathbb{R}$ , with  $x_r(t) = \sqrt{3 \cos^2(t) + 1}$ . We call this object the Peanut. Although this object is star-shaped, it is not in the solution space of trigonometric polynomials. For this scenario, the direction of the incident wave is  $d = (\cos(\pi/3), \sin(\pi/3))$ . The stopping criterion is (55) with  $\epsilon = 0.1$ . First, we try to approximate this object using trigonometric polynomials with  $N_r^{(1)} = 5$  and a circle with radius 0.1 centered at the origin as an initial guess. The result is shown in Figure 4.4(c). Later, we try to approximate this object using polynomials of B-splines with  $N_r^{(2)} = 12$  and a circle with radius 0.1 centered at the origin as an initial guess. The result is shown in Figure 4.4(d).

- In the third scenario, the object that we use as a scatterer has the parameterization  $x : [0, 2\pi] \rightarrow \mathbb{R}^2$ , with

$$x(t) = (\cos(t) + 0.65 \cos(2t) - 0.65, 1.5 \sin(t)). \quad (57)$$

We call this object the Kite. This object parameterization is not of the form  $x(t) = x_r(t)(\cos(t), \sin(t))$ , and is neither in the solution space of trigonometric polynomials nor the B-spline solution space. For this scenario, the direction of the incident wave is  $d = (-1, 0)$ . The stopping criterion is (55) with  $\epsilon = 0.1$ . First, we try to approximate this object using trigonometric polynomials with  $N_r^{(1)} = 20$  and a circle with radius 0.3 centered at the origin as an initial guess. The result is shown in Figure 4.4(e). Later, we try to approximate this object using polynomials of B-splines with  $N_r^{(2)} = 40$  and a circle with radius 0.3 centered at the origin as an initial guess. The result is shown in Figure 4.4(f).

Note that the dimension of both spaces for each of the scenarios is very similar: for the first two scenarios, the space  $\mathbb{X}_{N_r}^{(1)}$  has dimension 11 and the space  $\mathbb{X}_{N_r}^{(2)}$  has dimension 12, while for the third scenario,  $\mathbb{X}_{N_r}^{(1)}$  has dimension 41 and the space  $\mathbb{X}_{N_r}^{(2)}$  has dimension 40.

Looking at the reconstructions of the object for the three scenarios, we conclude that the solution obtained in the first scenario is very similar to that obtained in the second scenario

Object	$\epsilon$	Direction $d$	Iterations	
			Trig	B-spline
Pear	0.1	$(0, 1)$	48(113)	61(184)
Peanut	0.1	$(\sqrt{3}/2, 1/2)$	44(104)	111(353)
Kite	0.1	$(-1, 0)$	24(53)	195(525)

Table 4.2: Number of iterations needed for Method B to obtain the solution for the three scenarios using as solution spaces the space of trigonometric polynomials and the space of B-splines. The number of iterations needed for the trigonometric polynomial solution space is under the column labeled “Trig”, while the number of iterations needed for the B-spline solution space is under the column labeled “B-spline”. We have an incident plane wave with wavenumber  $k$ , and incidence direction  $d$ . The column labeled “Object” has the objects used in each one of the three scenarios, the column labeled  $\epsilon$  has the value used for the stopping criterion in each one of the scenarios, and the column Direction has the direction of the incident wave for each one of the scenarios.

using either space. For the third scenario, the solution obtained using the B-spline solution space has the same quality of the solution obtained using the solution space of trigonometric polynomials. Since the Kite is not in the solution space of trigonometric polynomials, it seems that the B-spline can approximate the object more closely.

We present in Table 4.2 the number of iterations of the two-step procedure needed for obtaining the solution in each of the three scenarios, in the same fashion as it was presented in Table 4.1 for Method B. For all the scenarios, the approximation using the solution space of trigonometric polynomials performs better computationally than the solution space of B-splines. One possible explanation for this is that the objects that we are approximating are parameterized using trigonometric functions.

Although using the space solution of trigonometric polynomials gives better computational performance, we still believe that the approach using the solution space of B-splines has some advantages. Such advantages are compatibility with CAD tools, the chance of obtaining good approximations for any kind of object despite the expensive computational cost, and finally the advantage of the B-splines being local functions, which guarantees that we can locally update some parameters of the object, obtaining better approximations; and this is not possible with trigonometric functions, since those functions are global in the entire domain.

### Example 4.1.3 (Relation of the frequency and initial guess with the solution)

In this example, we present the influence of the initial guess and frequency of the incident plane wave on the solution of the problem. We have two scenarios in this example. In each scenario presented, the far field data was measured at points uniformly distributed over the circle  $\hat{x}_l = (\cos(\theta_l), \sin(\theta_l))$ , for  $\theta_l = 2(l - 1)\pi/N_{ff}$ ,  $l = 1, \dots, N_{ff}$ , with  $N_{ff} = 32$ .

In the first scenario, we solve the problem for the incident plane wave with wavenumber  $k = 0.5$  and direction  $d = (1, 0)$ .

We first consider the object to be the Pear, and we solve the problem using the solution space of trigonometric polynomials with  $N_r^{(1)} = 5$  and the solution space of B-splines  $N_r^{(2)} = 8$  and  $q = 4$ . Later, we consider the object with parameterization  $x(t) = (2 + 0.4 \cos(9t))(\cos(t), \sin(t))$ , which we call from now on the 9-gear, and solve the problem using the solution space of trigonometric polynomials with  $N_r^{(1)} = 10$  and the solution space of B-splines  $N_r^{(2)} = 32$  and  $q = 4$ . For all tests, we use as an initial guess a circle with center at the origin and radius 0.5.

We present the result for the reconstruction of the Pear using the solution space of the trigonometric polynomials in Figure 4.5(a) and the result using the B-splines solution space in Figure 4.5(b). The result for the 9-gear reconstruction using the solution space of the trigonometric polynomials can be seen in Figure 4.5(c), while the result using the B-spline solution space can be seen in Figure 4.5(d).

In the second scenario, we take the incident plane wave with same direction  $d = (1, 0)$ , but different wavenumber  $k = 5$ .

For all tests, we use the 9-gear object, and we solve the problem using the solution space of trigonometric polynomials with  $N_r^{(1)} = 10$  and the solution space of B-splines  $N_r^{(2)} = 32$  and  $q = 4$ . For each of the solution spaces we solve the problem using as initial guess the circle centered at the origin with radius 0.5, and the circle centered at the origin with radius 2.

We present the result for the reconstruction of the 9-gear using the solution space of the trigonometric polynomials and as initial guess the circle centered at the origin with radius 0.5 in Figure 4.6(a). In Figure 4.6(b) we have the reconstruction using the same solution space with the initial guess being the circle centered at the origin with radius 2.

The result for the using the B-splines solution space can be seen in Figure 4.6(c), for the initial guess being the circle centered at the origin with radius 0.5, and in Figure 4.6(d), for the initial guess being the circle centered at the origin with radius 2.

Since the method presented is a linearization of Equation (6), the convergence of the solution to the shape of the object depends on the choice of initial guess. Also, Figures 4.5 and 4.6 indicate that there is a dependence on the magnitude of the wavenumber  $k$ , as expected from Theorem 2.2.3.

It is clear from Figures 4.5(a)–4.5(d) that for low frequencies, we can choose as an initial guess parameterizations that are not close to the original object and still obtain convergence for the method. On the other hand, we can see from Figures 4.6(a)–4.6(d) that for higher frequencies, the initial guess must be closer to the object in order to obtain convergence.

In the first scenario, where the incident plane wave has wavenumber  $k = 0.5$ , and where we used the circle of radius 0.5 centered at the origin as an initial guess, we were able to produce fuzzy approximations of the scattered object at low frequencies. In the second scenario where the incident plane wave has wavenumber  $k = 5$ , when we used the initial guess not close enough to object (Figures 4.6(a) and 4.6(c)), the method did not converge; however, as seen in Figures 4.6(b) and 4.6(d), when we used the initial guess as the circle with radius 2 centered at the origin, we obtained a relatively detailed reconstruction of the object.

It is clear that if we want to obtain a detailed reconstruction of the object it is necessary to use several frequencies, which sets the framework for the multi-frequency method shown in [21].

As expected from Example 4.1.2, the solutions obtained using the trigonometric polynomial solution space and the B-spline solution space are very similar, and can be both considered good quality reconstructions of the scatterer.

We can conclude that if the initial guess is not close enough to the object, the solution will not converge to the parameterization of the object  $D$ . The region where we choose the initial guess depends on the frequency used. For low frequencies, we can use solutions that are not close to the original object and still obtain convergence of the method. This behavior is summarized in the following table:

Frequency	Reconstruction	Initial Guess
Lower	Fuzzy	Simple
Higher	Sharp	Closer to object

## 4.2 Inverse scattering problem for multiple frequencies

In the last section, we presented a variation on Johansson and Sleeman’s method, which we called Method B, for the reconstruction of the shape of the object  $D$  using a single frequency.

It is shown in [21] that the scatterer can be reconstructed with a resolution that is proportional to the wavenumber, so for low wavenumbers and consequently low frequencies, we are able to produce rough approximations of the object, while for higher frequencies, we can reconstruct the object with detail in the illuminated part.

However, the convergence of our method depends on the frequency of the incident plane wave and on the initial guess used: see Theorem 3.1 of [23], where the authors used one step of the Newton method at each frequency. If we are using a lower frequency, we do not need an initial guess close to the object’s shape, while if we use a higher frequency our initial guess needs to be closer to the shape of the object.

We verify with our examples in the previous section that the method can provide fuzzy approximations to the shape of  $D$  using as an initial guess a shape that is not very close

to  $D$  when the frequency of the incident plane wave that generates the scattered data is low enough. At the same time, the method can provide sharp approximations of the object using data for higher frequencies when provided with an initial guess close to the shape of the object.

This dependence of the reconstruction on the data frequency led Chen to introduce in [21] a new approach to the reconstruction of objects using multi-frequency data for the reconstruction of the object. Chen proposed the RLA method for the potential problem, which would solve the inverse problem recursively on the frequency of the data. The inverse scattering problem for sound-soft obstacles was solved in [23] using the RLA. The problem solved in [23] is:

**Problem 2** *Given  $N_{total} = N_{ff} \times N_{inc}$  far field pattern measures at the  $N_{ff}$  points  $\hat{x}_l \in \Omega$ , where  $\Omega$  is the circle of centered at the origin with radius 1, generated by the scattering of the  $N_{inc}$  incident plane waves  $u_j^{inc}(x) = e^{ik_j x \cdot d}$  with fixed direction  $d$  and varying wavenumbers  $k_j$  for  $j = 1, \dots, N_{inc}$ , where  $k_1 < k_2 < \dots < k_{N_{inc}}$  by an unknown object  $D$  with known boundary condition, reconstruct the shape of the object  $D$ .*

The idea of the RLA is that for each single frequency, we would use a Newton method to solve the inverse scattering problem, as shown in [23]. As we saw in Chapter 2, the Newton method is very expensive because it requires the solution of several different direct problems for the same boundary  $\partial D$  and different boundary conditions [3]. To overcome this problem and improve the speed of the method, we propose to use Method B instead of the Newton method to solve the problem at each frequency.

### 4.2.1 Numerical implementation of the RLA-B

We present the numerical implementation of the RLA using Method B for each frequency.

Suppose that our data set contains measures of the far field pattern for an object  $D$  at the points  $\hat{x}_l$ ,  $l = 1, \dots, N_{ff}$  for different wave numbers  $k_j$ ,  $j = 1, \dots, N_{inc}$ , where  $k_1 < k_2 < \dots < k_{N_{inc}}$ . Our idea is to implement Algorithm 4.1.1 from the last section for each one of the wavenumbers  $k_j$ , starting from the lowest and going recursively to the highest.

Choose a solution space  $\mathbb{X}_{N_r}$  and an initial guess  $\mathbf{x}^{(0)}$ . Take  $\mathbf{x}_{\mathbf{k}_1}^{(0)} = \mathbf{x}^{(0)}$  and apply Algorithm 4.1.1. We obtain an approximate solution  $\mathbf{x}_{\mathbf{k}_1}^{(sol)}$ . We make  $\mathbf{x}^{(1)} = \mathbf{x}_{\mathbf{k}_1}^{(sol)}$ . We repeat this procedure recursively to obtain Algorithm 4.2.1 in Figure 4.2.1.

**Remark 4.2.1** *We should not expect to obtain a good approximation in the shadowed part of the object, since the scattered field of the object goes to zero in that region with increasing frequency. The shadowed part of the object is the part with the worse approximation.*

**Remark 4.2.2** *Although there is not a uniform way to choosing the stopping criteria for each of the steps, it is possible to use the same stopping criteria for each problem with a fixed frequency, or to use adaptive stopping criteria dependent on the frequency or the quality of the approximation.*

## 4.2.2 Numerical results

**Example 4.2.1** *The multi-frequency Algorithm 4.2.1*

We consider four scenarios using the multiple frequency Algorithm 4.2.1. In each of the scenarios, we consider a scatterer  $D$  and multiple incident waves with fixed direction  $d$  and varying wavenumber  $k_j$ , where  $j = 1, \dots, N_{\text{inc}}$ . We measure the far field data at points uniformly distributed over the circle  $\hat{x}_l = (\cos(\theta_l), \sin(\theta_l))$ , for  $\theta_l = 2(l-1)\pi/N_{ff}$ ,  $l = 1, \dots, N_{ff}$  for each of the wavenumbers  $k_j$ ,  $j = 1, \dots, N_{\text{inc}}$ . We look for the star-shaped solution  $x(t) = x_r(t)(\cos(t), \sin(t))$  with the radius function  $x_r(t)$  in the space of trigonometric polynomials

$$\mathbb{X}_{N_r} = \left\{ x_r(t) \mid x_r(t) = a_0 + \sum_{m=1}^{N_r} (a_m \cos(mt) + b_m \sin(mt)), x_r(0) = x_r(2\pi), x_r(t) > x_{\min} \right\}.$$

In all the scenarios, we use as an initial guess the circle centered at the origin with radius 0.1.

- In the first scenario, we consider the object  $D$  to be the Kite. The number of incident plane waves is  $N_{\text{inc}} = 8$ , the incidence direction of the plane waves is  $d = (-1, 0)$  and the wavenumber of each of the waves is  $k_j = 0.5j$ , where  $j = 1, \dots, N_{\text{inc}}$ . We find the solution in the space of trigonometric polynomials with degree  $N_r = 20$ . In Figure 4.8, we show the partial result obtained by the method at wavenumbers: (a)  $k = 0.5$ , (b)  $k = 2$ , and (c)  $k = 3.5$ . In (d), we have the solution for the method using all frequencies.
- In the next scenario, we assume that the object  $D$  has parameterization  $x : [0, 2\pi] \rightarrow \mathbb{R}^2$ , with  $x(t) = (2 + 0.4 \cos(7t))(\cos(t), \sin(t))$ , to which we refer from now on as the “7-gear”. The number of incident plane waves is  $N_{\text{inc}} = 10$ , the incidence direction of the plane waves is  $d = (0, 1)$ , and the wavenumber of each of the waves is  $k_j = 0.5j$ , where  $j = 1, \dots, N_{\text{inc}}$ . We choose to look for the solution in the space of trigonometric polynomials with degree  $N_r = 10$ . In Figure 4.9, we show the partial result obtained by the method at wavenumbers: (a)  $k = 0.5$ , (b)  $k = 2$ , and (c)  $k = 3.5$ . In Figure 4.9(d), we have the solution for the method using all frequencies.
- In the third scenario, we consider the object  $D$  to be the 9-gear. The number of incident plane waves is  $N_{\text{inc}} = 12$ , the incidence direction of the plane waves is  $d = (1, 0)$ , and the wavenumber of each of the waves is  $k_j = 0.5j$ , where  $j = 1, \dots, N_{\text{inc}}$ . We choose to look for the solution in the space of trigonometric polynomials with degree  $N_r = 10$ .

In Figure 4.10, we show the partial result obtained by the method at wavenumbers: (a)  $k = 0.5$ , (b)  $k = 2.5$ , and (c)  $k = 4.5$ . In Figure 4.10(d), we have the solution for the method using all frequencies.

- In the last scenario, we assume that the object  $D$  has a parameterization  $x : [0, 2\pi] \rightarrow \mathbb{R}^2$ , with  $x(t) = (2 + 0.4 \cos(15t))(\cos(t), \sin(t))$ , to which we refer from now on as the “15-gear”. The number of incident plane waves is  $N_{\text{inc}} = 12$ , the incidence direction of the plane waves is  $d = (1, 0)$ , and the wavenumber of each of the waves is  $k_j = 0.5j$ , where  $j = 1, \dots, N_{\text{inc}}$ . We choose to look for the solution in the space of trigonometric polynomials with degree  $N_r = 17$ . In Figure 4.11, we show the partial result obtained by the method at wavenumbers: (a)  $k = 0.5$ , (b)  $k = 2$ , and (c)  $k = 4.5$ . In Figure 4.11(d), we have the solution for the method using all frequencies.

We also present the plot of the residue as a function of frequency for the multi-frequency method in Figure 4.12. Each point in the graph is the residue after one iteration of the two-step procedure. This graph shows the decrease in the residue with the increase of the frequency, which happens because we are improving the details of the solution in the illuminated part. We see that the residue does not go to zero with increasing frequency; instead, it seems to stabilize at a value greater than zero. We expect this, since we are not able to provide a good approximation of the object in the shadowed part and most of the error of the residue is due to the inaccuracy of the approximation in that part of the object.

We come to the following conclusions:

- As expected, we obtain a detailed reconstruction of the object in the illuminated part. Unfortunately, the method is not able to obtain a good reconstruction of the shadowed part of the object.
- We can consider the multiple frequency solution procedure as a preconditioning of the method. The solution at each lower frequency works as an initial guess for the method at the next higher frequency.
- To address the problem of not being able to reconstruct the shadowed part of the object, in the next section we introduce objects that will work as reflectors for the incident wave, providing information from the shadowed part.

### 4.3 Inverse scattering problem for multiple frequencies in the presence of multiple scatterers

In the previous section, we presented our method for the reconstruction of the object using far field measurements at multiple frequencies. The method seems to provide very detailed

reconstructions of the illuminated part of the object; however, we are not able to obtain a sharp reconstruction of the shadowed part of the object. To overcome this problem we follow the ideas of Sini and Nguyen (work in progress) and use multiple scatterers to reflect the incident wave back to the shadowed part of the object  $D$ .

We presented the implementation of the direct multiple scattering problem in Chapter 3, and we use this implementation in the multifrequency method in the presence of multiple objects. The method is an extension of the procedures in Section 4.2 with the presence of multiple objects.

### 4.3.1 Numerical results

We present an example illustrating the method using data obtained at multiple frequencies and with introduced obstacles. The examples illustrate the improvement of the reconstruction of the object in the presence of known scatterers. We solve the same problem as in Example 4.2.2.

- We repeat the first scenario of the previous example, but this time, instead of having only the Kite, we also have two known scatterers: the circle of radius 1 centered at the point  $(-6, -6)$ , and the circle of radius 1 centered at the point  $(-6, 6)$ . The number of incident plane waves is  $N_{\text{inc}} = 8$ , the incidence direction of the plane waves is  $d = (-1, 0)$ , and the wavenumber of each of the waves is  $k_j = 0.5j$ , where  $j = 1, \dots, N_{\text{inc}}$ . We choose to look for the solution in the space of trigonometric polynomials with degree  $N_r = 30$ . The result is shown in Figure 4.13(a).
- In the next scenario, we consider the object  $D$  to be the 7-gear and introduce two scatterers: the circle of radius 1 centered at the point  $(6, 7)$ , and the circle of radius 1 centered at the point  $(-6, 7)$ . The number of incident plane waves is  $N_{\text{inc}} = 10$ , the incidence direction of the plane waves is  $d = (0, 1)$ , and the wavenumber of each of the waves is  $k_j = 0.5j$ , where  $j = 1, \dots, N_{\text{inc}}$ . We choose to look for the solution in the space of trigonometric polynomials with degree  $N_r = 10$ . In Figure 4.13(b), we have the solution for the method using all frequencies.
- In the third scenario, we consider the object  $D$  to be the 9-gear and introduce two scatterers: the circle of radius 1 centered at the point  $(6, 6)$ , and the circle of radius 1 centered at the point  $(6, -6)$ . The number of incident plane waves is  $N_{\text{inc}} = 12$ , the incidence direction of the plane waves is  $d = (1, 0)$ , and the wavenumber of each of the waves is  $k_j = 0.5j$ , where  $j = 1, \dots, N_{\text{inc}}$ . We choose to look for the solution in the space of trigonometric polynomials with degree  $N_r = 10$ . In Figure 4.13(c), we have the solution for the method using all frequencies.

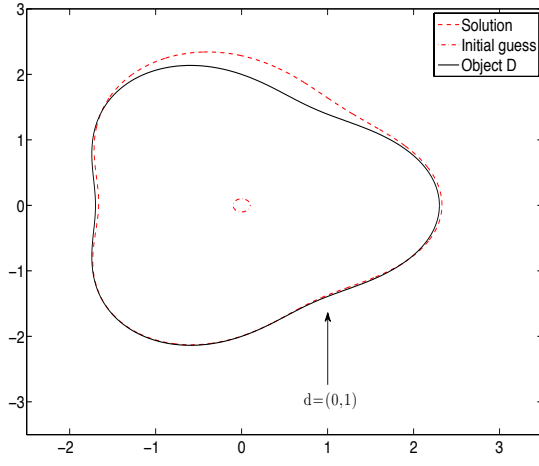
- In the last scenario, we consider the object  $D$  to be the 15-gear and introduce two scatterers: the circle of radius 1 centered at the point  $(6, 6)$ , and the circle of radius 1 centered at the point  $(6, -6)$ . The number of incident plane waves is  $N_{\text{inc}} = 12$ , the incidence direction of the plane waves is  $d = (1, 0)$ , and the wavenumber of each of the waves is  $k_j = 0.5j$ , where  $j = 1, \dots, N_{\text{inc}}$ . We choose to look for the solution in the space of trigonometric polynomials with degree  $N_r = 17$ . In Figure 4.13(d), we have the solution for the method using all frequencies.

As in the last example, we also present in Figure 4.14 the graph of the residue as a function of the frequency for the multifrequency method. Each point in the graph is the residue after an iteration of the two-step procedure.

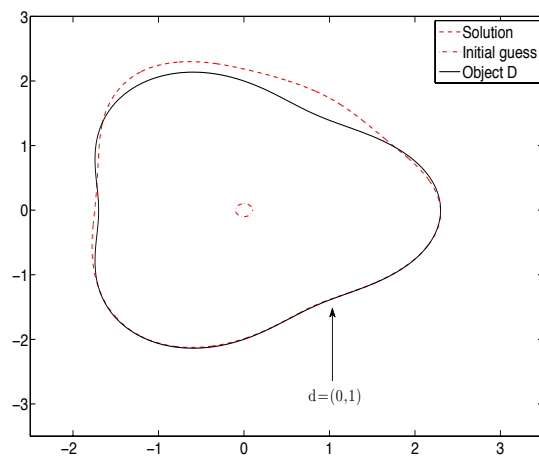
This time, we see a decrease in the residue with increasing frequency. This is a consequence of the better approximation to the shadowed part of the object due to the reflection of the incident plane wave off the known scatterers. Those reflections work as incident waves in and of themselves, improving the quality of the approximation in the shadowed part of the object.

We conclude the following:

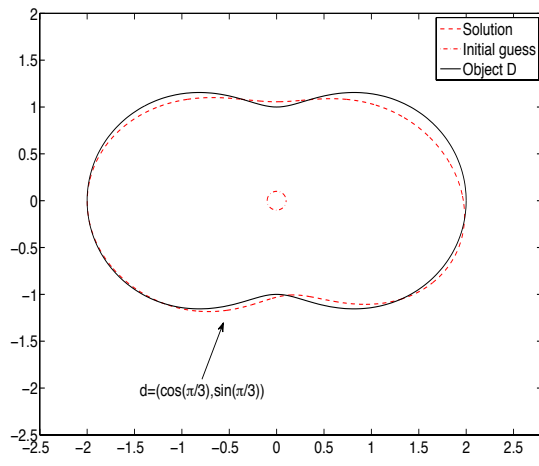
- We are able to provide good reconstructions of the object. The incident wave reflects off the scatterers introduced, and this reflected wave illuminates the shadowed parts of the object, providing us the information necessary for reconstructing these parts.
- We can consider the scatterers as sources for new waves; this is a good opportunity to obtain more information from the object with the use of fewer sources.



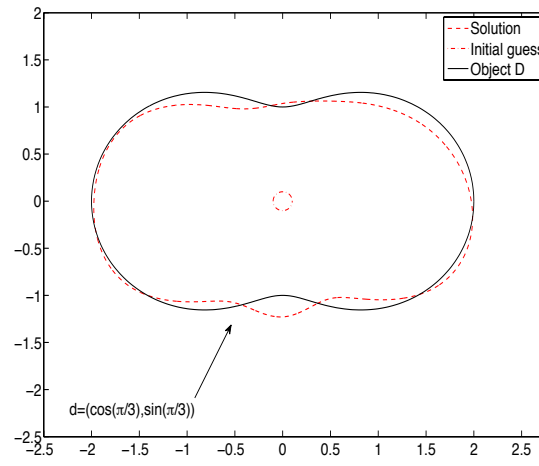
(a) Trigonometric,  $k = 1$ ,  $d = (0, 1)$ ,  $N_r^1 = 5$



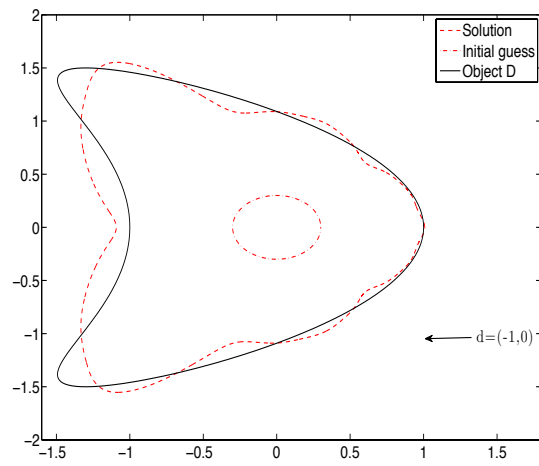
(b) Spline,  $k = 1$ ,  $d = (0, 1)$ ,  $N_r^2 = 12$



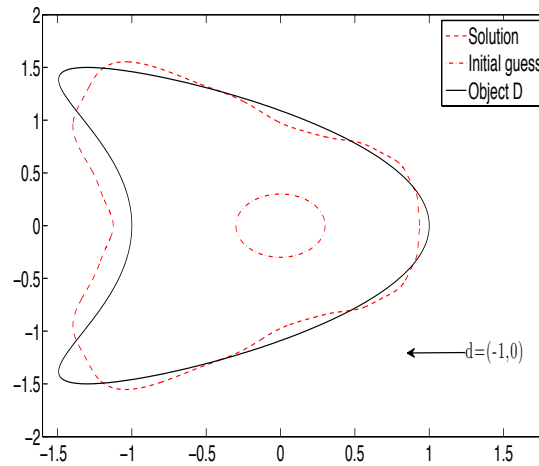
(c) Trigonometric,  $k = 1$ ,  $d = (\sqrt{3}/2, 1/2)$ ,  $N_r^1 = 5$



(d) Spline,  $k = 1$ ,  $d = (\sqrt{3}/2, 1/2)$ ,  $N_r^2 = 12$

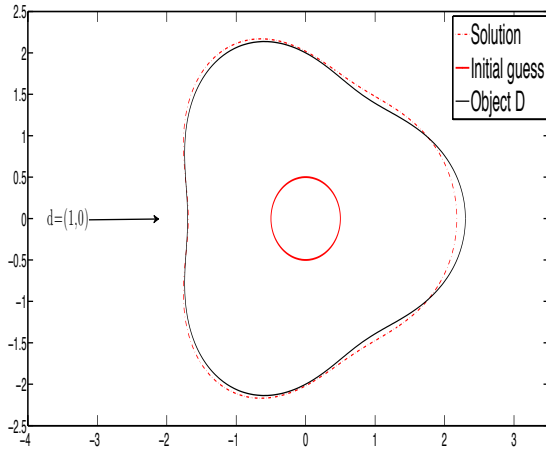


(e) Trigonometric,  $k = 1$ ,  $d = (-1, 0)$ ,  $N_r^1 = 20$

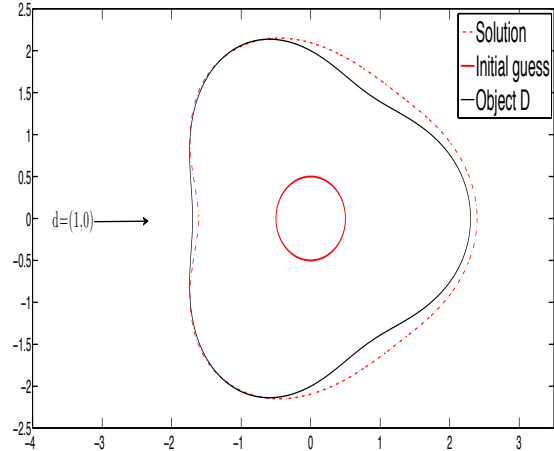


(f) Spline,  $k = 1$ ,  $d = (-1, 0)$ ,  $N_r^2 = 40$

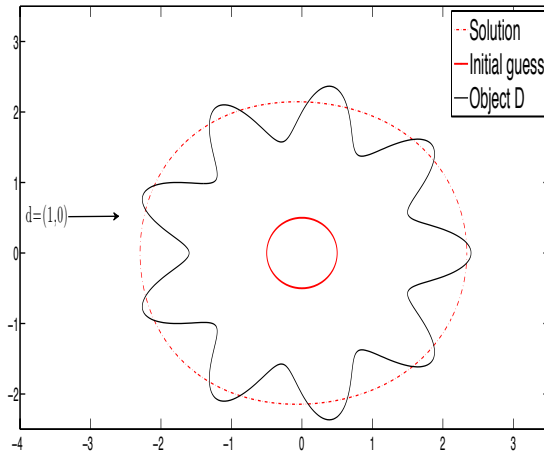
Figure 4.4: We solve for the Pear using: (a) the space of trigonometric polynomials with  $N_r^{(1)} = 5$ ; and (b) the space of B-splines with  $N_r^{(2)} = 12$ . We solve for the Peanut using (c) the space of trigonometric polynomials with  $N_r^{(1)} = 5$ ; and (d) the solution of B-splines with  $N_r^{(2)} = 12$ . We solve for the Kite using: (e) the space of trigonometric polynomials with  $N_r^{(1)} = 20$ ; and (f) the space of B-splines with  $N_r^{(2)} = 40$ .



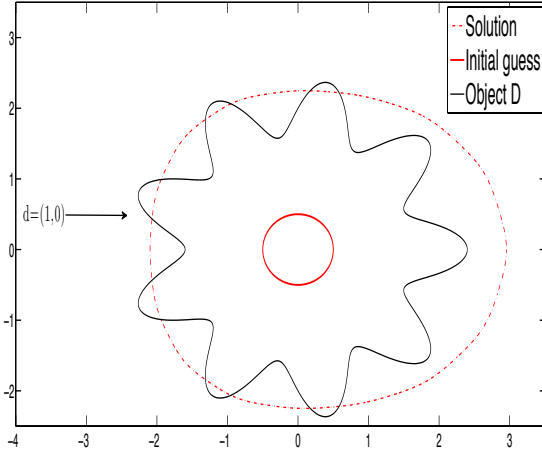
(a)  $k = 0.5$ ,  $N_r = 5$ ,  $d = (1, 0)$



(b)  $k = 0.5$ ,  $N_r = 10$ ,  $d = (1, 0)$



(c)  $k = 0.5$ ,  $N_r = 8$ ,  $d = (1, 0)$



(d)  $k = 0.5$ ,  $N_r = 32$ ,  $d = (1, 0)$

Figure 4.5: Solution of the inverse scattering problem for incident plane wave with wavenumber  $k = 0.5$  and incident direction  $d = (1, 0)$  and using as initial guess the circle with center at the origin and radius 0.5. (a) Using the solution space of trigonometric polynomials to reconstruct the Pear with  $N_r^{(1)} = 5$ . (b) Using the solution space of B-splines to reconstruct the Pear with  $N_r^{(2)} = 8$  and  $q = 4$ . (c) Using the solution space of trigonometric polynomials to reconstruct the 9-gear with  $N_r = 10$ . (d) Using the solution space of B-splines to reconstruct the 9-gear with  $N_r = 32$ .

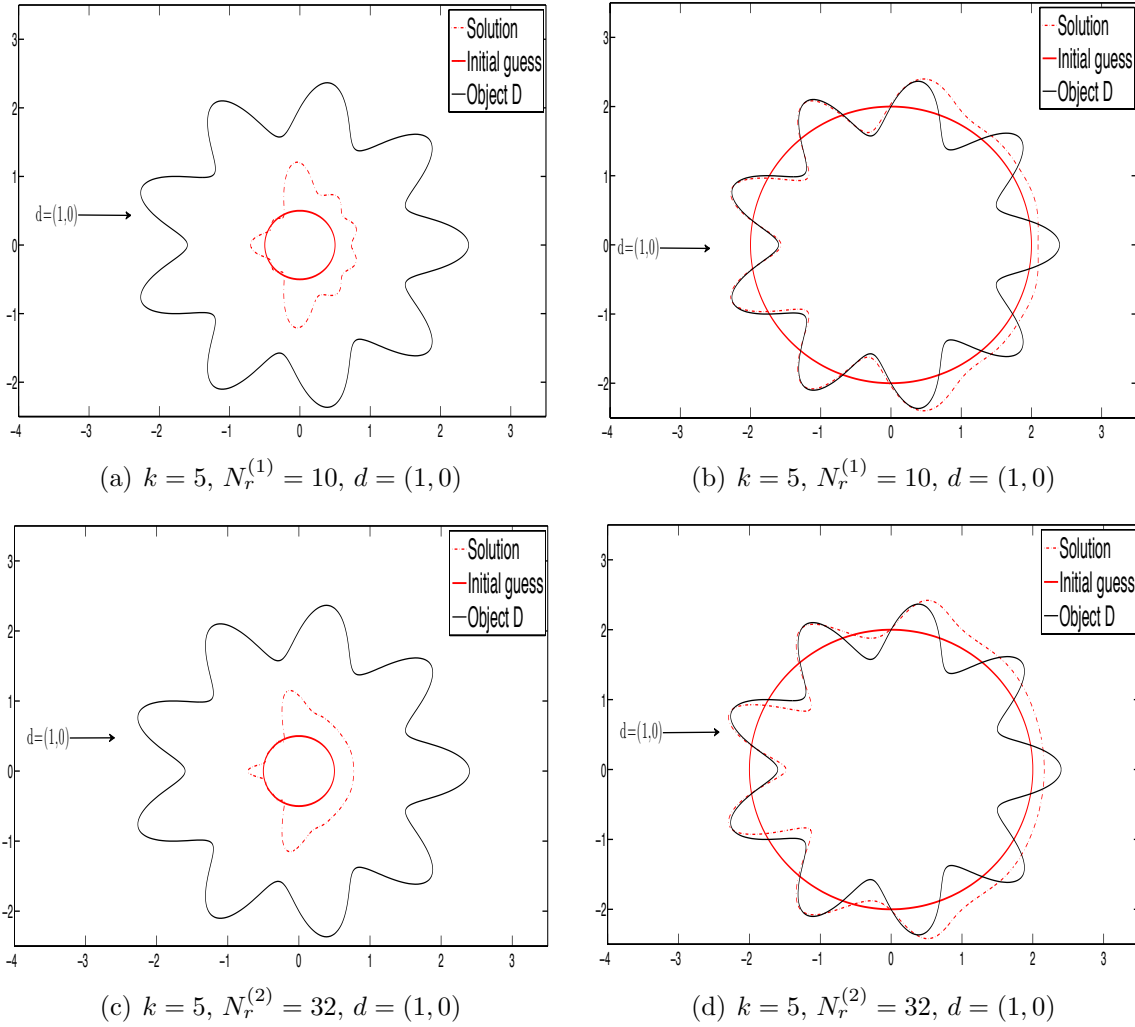


Figure 4.6: Solution of the inverse scattering problem for incident plane wave with wavenumber  $k = 0.5$  and incident direction  $d = (1, 0)$ . We reconstruct the 9-gear. (a) Using the solution space of trigonometric polynomials with  $N_r^{(1)} = 10$  and initial guess being the circle with center at the origin and radius 0.5. (b) Using the solution space of trigonometric polynomials with  $N_r^{(1)} = 10$  and initial guess being the circle with center at the origin and radius 2. (c) Using the solution space of B-splines with  $N_r^{(2)} = 32, q = 4$  and initial guess being the circle with center at the origin and radius 0.5. (d) Using the solution space of B-splines with  $N_r^{(2)} = 32, q = 4$  and initial guess being the circle with center at the origin and radius 2.

**Algorithm 4.2.1** *Given the initial guess  $\mathbf{x}^{(0)}$ , and the measured far-field pattern  $\mathbf{u}_\infty^{\mathbf{k}_j}$  at the points  $\hat{x}_l$ , for  $l = 1, \dots, N_{ff}$ , in the unit disk for the respective wavenumbers  $k_j$ ,  $j = 1, \dots, N_{inc}$ .*

1. For  $j = 1, \dots, N_{inc}$ :
  - (a) Use Algorithm 4.1.1 with initial guess  $\mathbf{x}_{\mathbf{k}_j}^{(0)} = \mathbf{x}^{(j-1)}$  and far field pattern measures  $\mathbf{u}_\infty^{\mathbf{k}_j}$ . We obtain the result  $\mathbf{x}_{\mathbf{k}_j}^{(sol)}$ .
  - (b) Make  $\mathbf{x}^{(j)} = \mathbf{x}_{\mathbf{k}_j}^{(sol)}$ .

Figure 4.7: Implementation of the iterative method for solving the inverse problem for an object  $D$  with Dirichlet boundary conditions using multiple frequencies far field pattern measures.

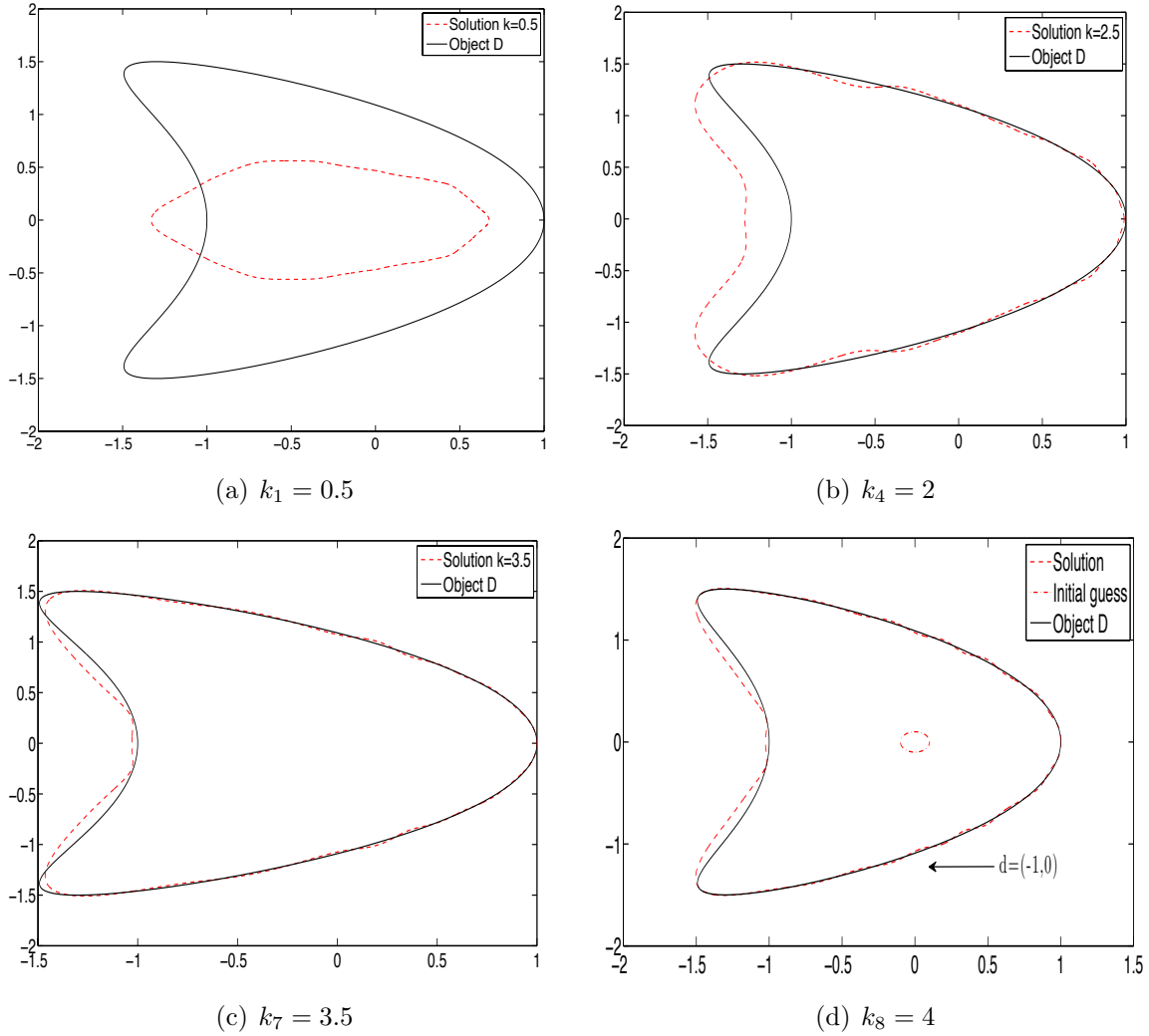


Figure 4.8: Solution of the inverse scattering problem for the Kite using the multi-frequency method. The incident plane waves have fixed incidence direction  $d = (-1, 0)$  and varying wavenumbers  $k_j = 0.5j$ , where  $j = 1, \dots, 8$ . We use as the initial guess for the multi-frequency the circle with center at the origin and radius 0.1. The solution space with trigonometric polynomials of degree  $N_r = 20$  is used for the method. We have the partial solution obtained at the wavenumber: (a)  $k_1 = 0.5$ , (b)  $k_4 = 2$ , and (c)  $k_7 = 3.5$ . In (d), we have the solution using all frequencies.

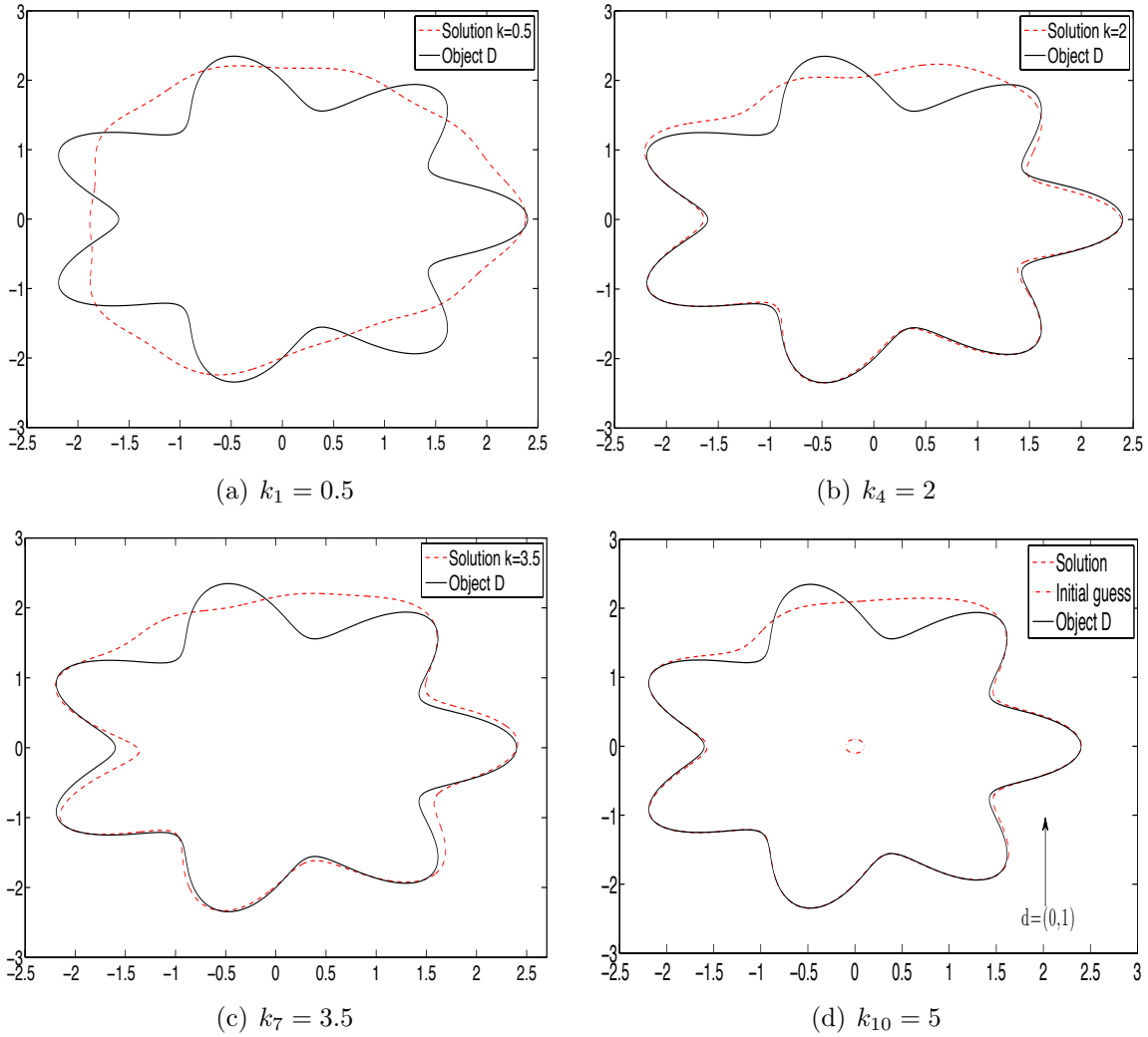


Figure 4.9: Solution of the inverse scattering problem for the 7-gear using the multi-frequency method. The incident plane waves have fixed incidence direction  $d = (0, 1)$  and varying wavenumbers  $k_j = 0.5j$ , where  $j = 1, \dots, 10$ . We use as the initial guess for the multi-frequency the circle with center at the origin and radius 0.1. The solution space with trigonometric polynomials of degree  $N_r = 10$  is used for the method. We have the partial solution obtained at the wavenumber: (a)  $k_1 = 0.5$ , (b)  $k_4 = 2$ , and (c)  $k_7 = 3.5$ . In (d), we have the solution using all frequencies.

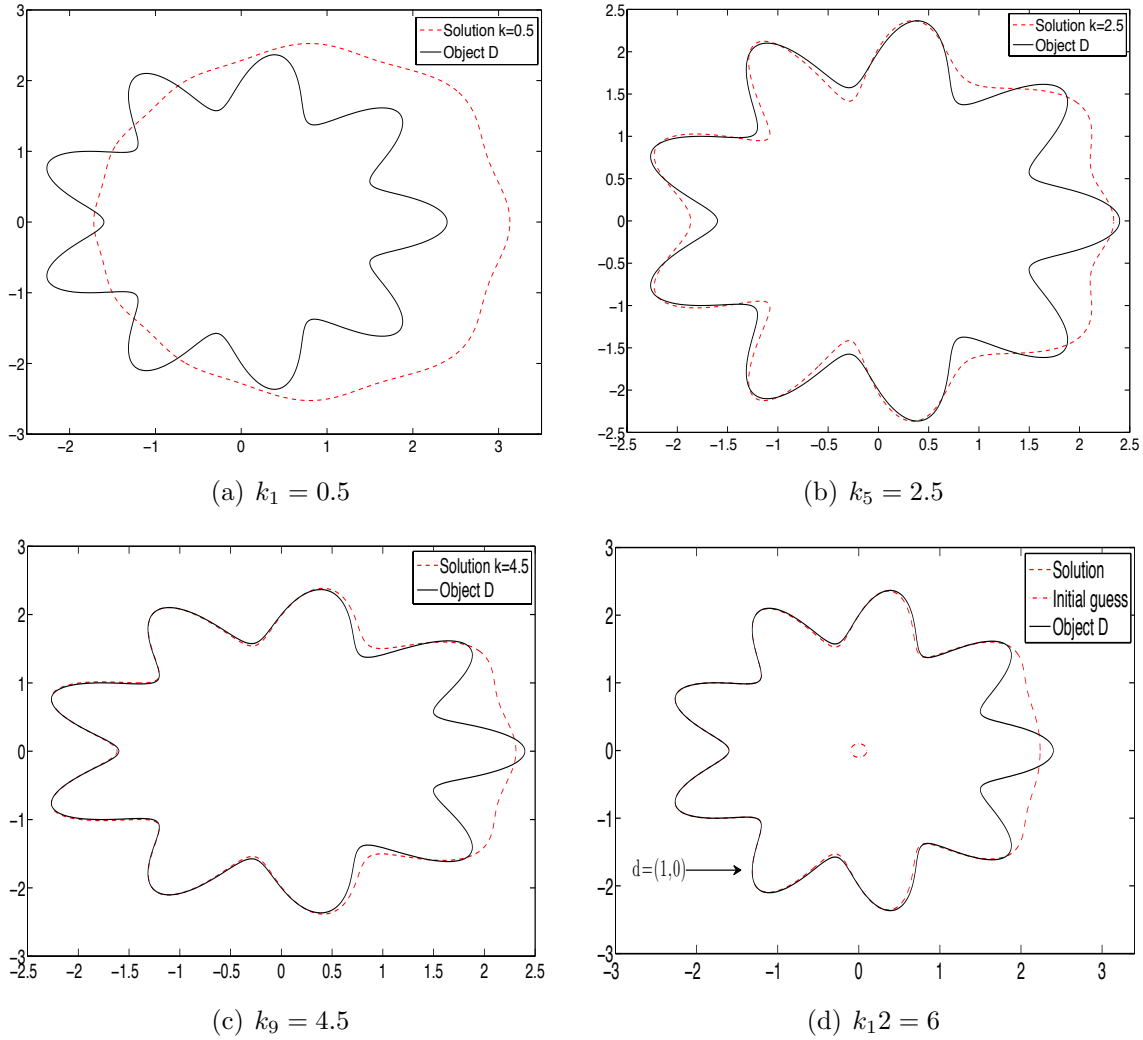


Figure 4.10: Solution of the inverse scattering problem for the 9-gear using the multi-frequency method. The incident plane waves have fixed incidence direction  $d = (1, 0)$  and varying wavenumbers  $k_j = 0.5j$ , where  $j = 1, \dots, 12$ . We use as the initial guess for the multi-frequency the circle with center at the origin and radius 0.1. The solution space with trigonometric polynomials of degree  $N_r = 10$  is used for the method. We have the partial solution obtained at the wavenumber: (a)  $k_1 = 0.5$ , (b)  $k_5 = 2.5$ , and (c)  $k_9 = 4.5$ . In (d), we have the solution using all frequencies.

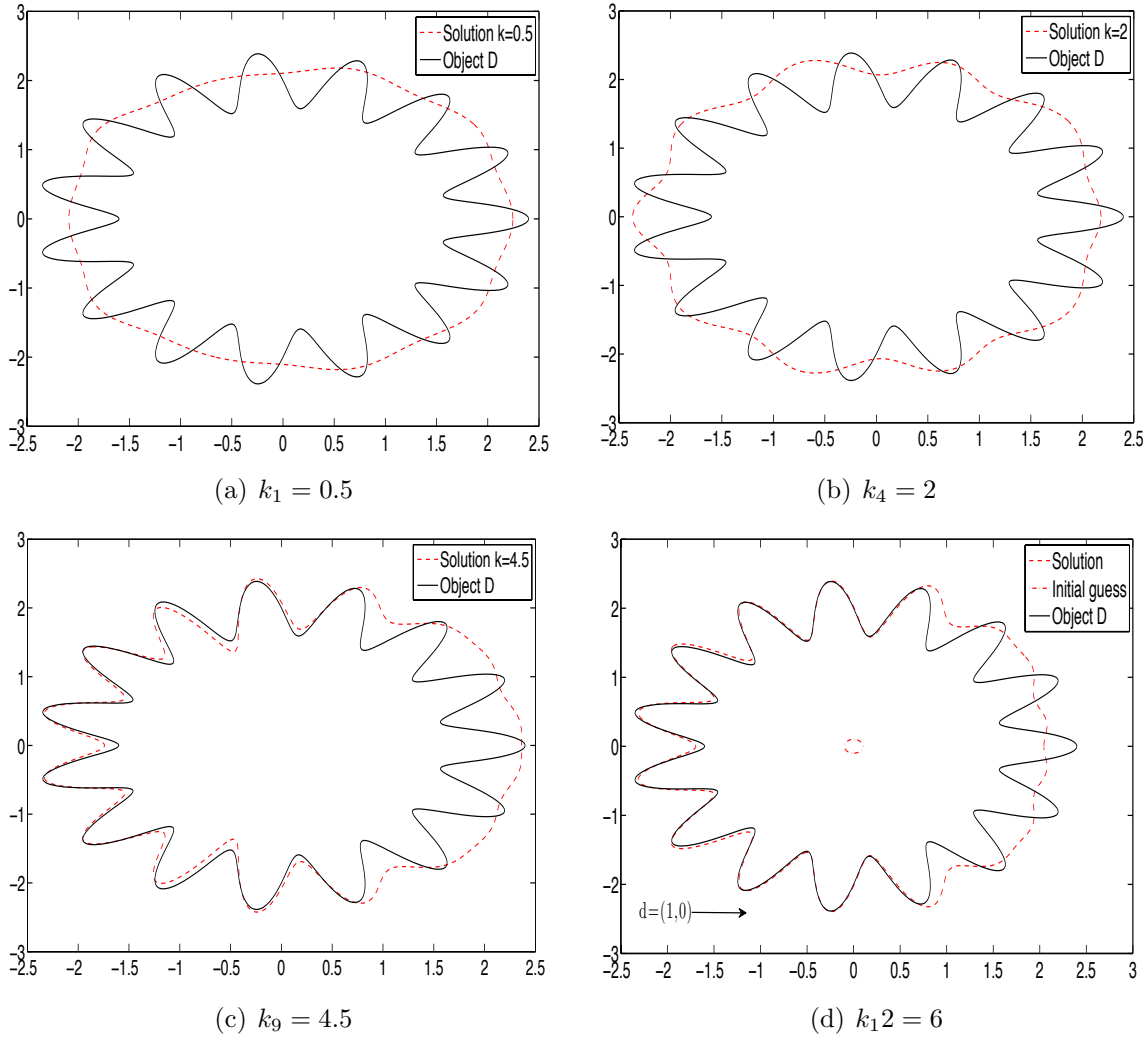
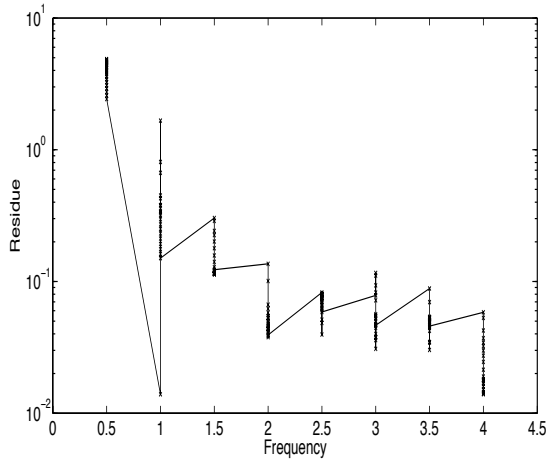
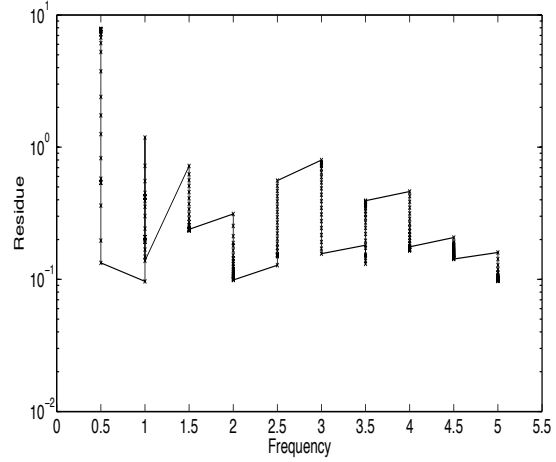


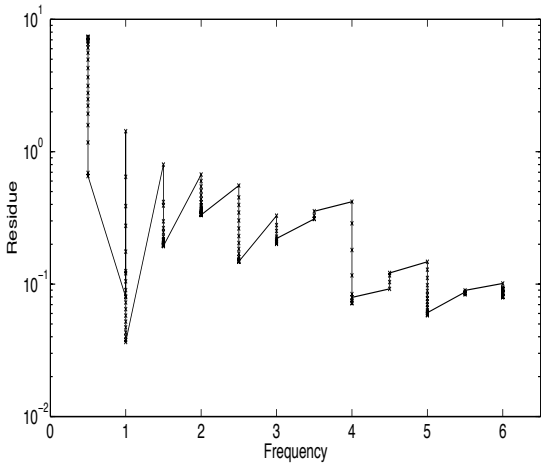
Figure 4.11: Solution of the inverse scattering problem for the 15-gear using the multi-frequency method. The incident plane waves have fixed incidence direction  $d = (1, 0)$  and varying wavenumbers  $k_j = 0.5j$ , where  $j = 1, \dots, 12$ . We use as the initial guess for the multi-frequency the circle with center at the origin and radius 0.1. The solution space with trigonometric polynomials of degree  $N_r = 17$  is used for the method. We have the partial solution obtained at the wavenumber: (a)  $k_1 = 0.5$ , (b)  $k_4 = 2$ , and (c)  $k_9 = 4.5$ . In (d), we have the solution using all frequencies.



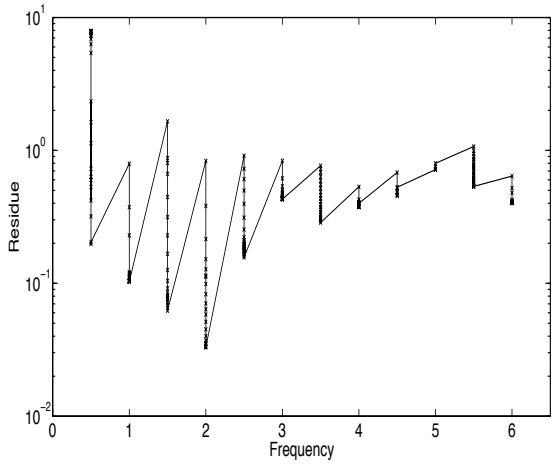
(a) Kite,  $k_j = 0.5j$ ,  $j = 1, \dots, 8$ ,  $d = (-1, 0)$



(b) 7-Gear,  $k_j = 0.5j$ ,  $j = 1, \dots, 16$ ,  $d = (0, 1)$

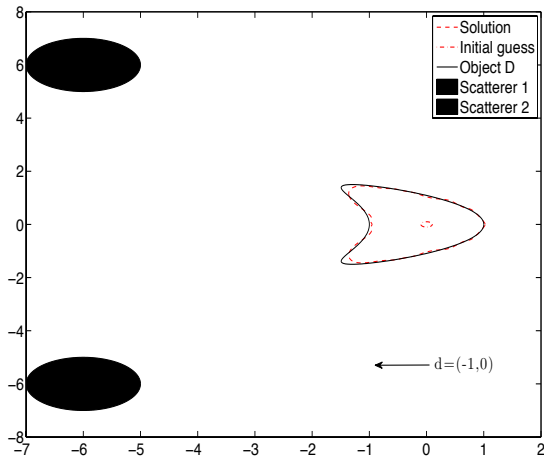


(c) 9-gear,  $k_j = 0.5j$ ,  $j = 1, \dots, 16$ ,  $d = (1, 0)$

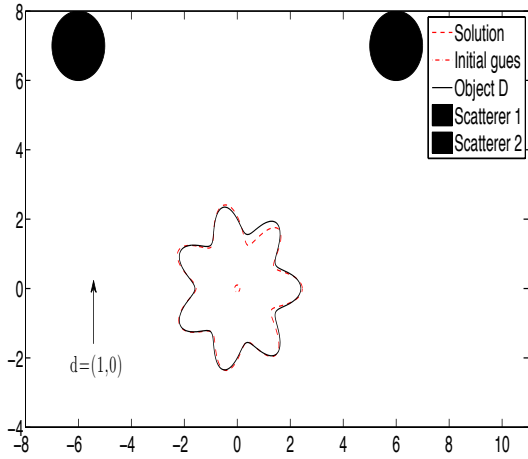


(d) 15-gear,  $k_j = 0.5j$ ,  $j = 1, \dots, 16$ ,  $d = (1, 0)$

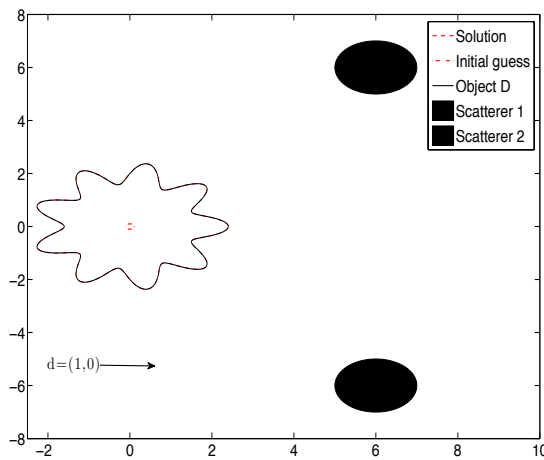
Figure 4.12: Graph of the residue versus frequency for the multi-frequency method. We present the graph for the scenarios in our example for: (a) Kite, (b) 7-gear, (c) 9-gear and (d) 15-gear. On the  $y$ -axis, we have the residue on the log-scale and on the  $x$ -axis we have the frequency. Each point in the graph is the residue after an iteration of the two-step procedure.



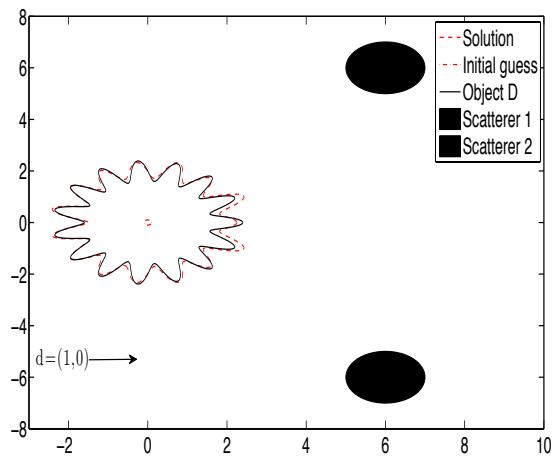
(a)  $k_j = 0.5j$ ,  $N_r = 30$ ,  $N_{\text{inc}} = 8$ ,  $d = (-1, 0)$



(b)  $k_j = 0.5j$ ,  $N_r = 10$ ,  $N_{\text{inc}} = 10$ ,  $d = (0, 1)$

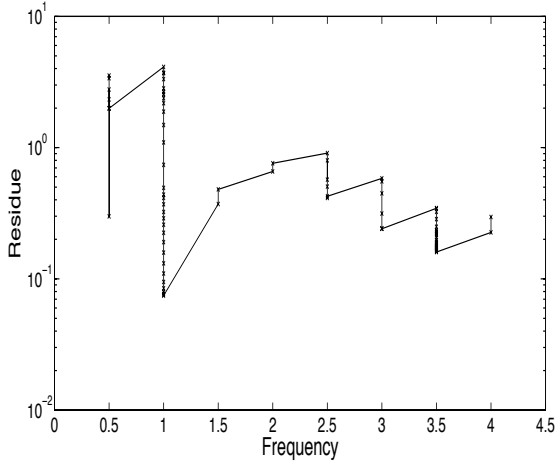


(c)  $k_j = 0.5j$ ,  $N_r = 10$ ,  $N_{\text{inc}} = 12$ ,  $d = (1, 0)$

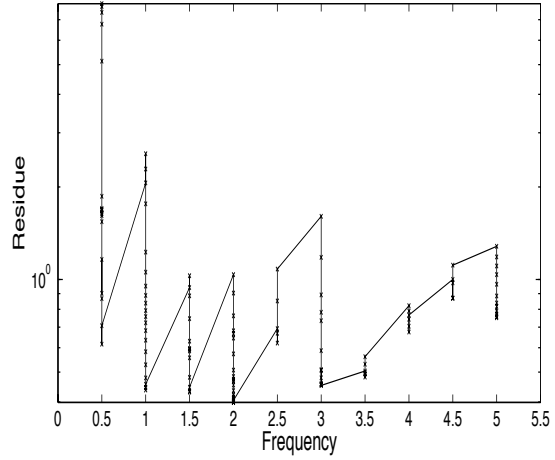


(d)  $k_j = 0.5j$ ,  $N_r = 17$ ,  $N_{\text{inc}} = 12$ ,  $d = (1, 0)$

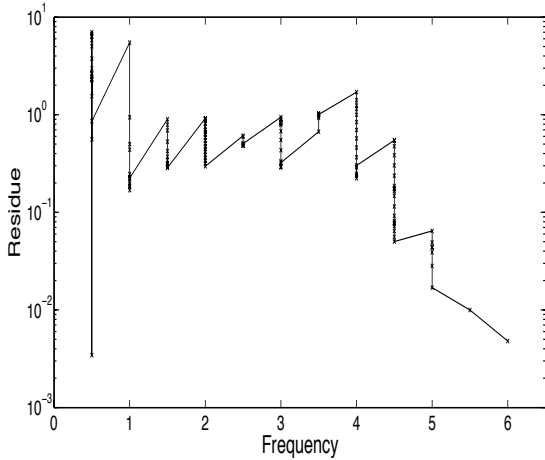
Figure 4.13: Solution of the inverse scattering problem for: (a) Kite in the presence of two circles of radius 1 with centers at  $(-6, 6)$  and  $(-6, -6)$ , (b) 7-gear in the presence of two circles of radius 1 with centers at  $(-6, 7)$  and  $(6, 7)$ , (c) 9-gear in the presence of two circles of radius 1 with centers at  $(-6, 6)$  and  $(6, 6)$ , and (d) 15-gear in the presence of two circles of radius 1 with centers at  $(-6, 6)$  and  $(6, 6)$ .



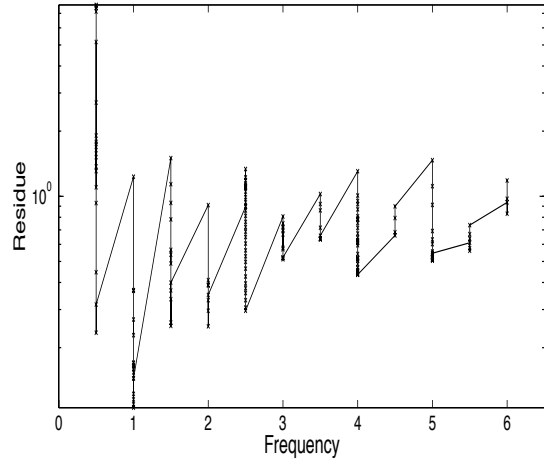
(a) Kite,  $k_j = 0.5j$ ,  $j = 1, \dots, 8$ ,  $d = (-1, 0)$



(b) 7-Gear,  $k_j = 0.5j$ ,  $j = 1, \dots, 16$ ,  $d = (0, 1)$



(c) 9-gear,  $k_j = 0.5j$ ,  $j = 1, \dots, 16$ ,  $d = (1, 0)$



(d) 15-gear,  $k_j = 0.5j$ ,  $j = 1, \dots, 16$ ,  $d = (1, 0)$

Figure 4.14: Plot of the residue versus frequency for the multifrequency method in the presence of known objects. We present the graph for the scenarios in our example for: (a) Kite in the presence of two circles of radius 1 with centers at  $(-6, 6)$  and  $(-6, -6)$ , (b) 7-gear in the presence of two circles of radius 1 with centers at  $(-6, 7)$  and  $(6, 7)$ , (c) 9-gear in the presence of two circles of radius 1 with centers at  $(-6, 6)$  and  $(6, 6)$ , and (d) 15-gear in the presence of two circles of radius 1 with centers at  $(-6, 6)$  and  $(6, 6)$ . On the  $y$ -axis, we have the residue on the log-scale and on the  $x$ -axis we have the frequency. Each point in the graph is the residue after an iteration of the two-step procedure.

# Chapter 5

## A globalization technique for inverse problems

In this chapter, we present a globalization technique to use with the methods of the previous section. For frequencies out of the resonance region the initial guess must be very close to the object that we want to reconstruct; however, most of the time we do not have such a close initial guess. To address this problem, we introduce in this chapter several globalization techniques that provide a better initial guess for the methods.

In Section 5.1, we derive (71) to approximate the far field pattern of a strictly convex object using the Kirchhoff approximation for the wave scattered by an obstacle (60). This formula is the basis for the globalization techniques presented in this chapter. Following the presentation of the formula, we show some numerical results comparing the far field pattern obtained by the Kirchhoff approximation formula and the method of integral equations presented in Chapter 2.

The numerical solution of the direct scattering problem presented in Chapter 3 is very accurate, as can be seen in [3; 67], but the mesh discretization used is proportional to the wavenumber  $k$  of the incident plane wave. This means that the number of columns and also rows of the scattering matrix for the domain with parameterization  $x$ ,  $\mathbf{S}_{\mathbf{x}_r}$ , grows linearly with  $k$ , which means that the problem is more computationally expensive to solve. To avoid expending computational resources in the solution of the direct scattering problem, we use the Kirchhoff approximation for high frequencies. Using the Kirchhoff approximation for convex objects on high frequencies, we are able to obtain a formula to calculate directly the far field pattern without constructing the integral operators  $S_{x_r}$  and  $S_{x_r, \infty}$ .

In the Section 5.2, we present a method based on the Kirchhoff approximation to obtain a formula to solve the inverse scattering problem. We also apply the method to reconstruct a circle with radius  $R$  and center at the origin and prove that the region of convergence is proportional to  $1/k$ , where  $k$  is the wavenumber of the incident plane wave.

Finally, in Section 5.3, we deal with the following new problem to reconstruct an object  $D$ :

**Problem 3** *Given the far field patterns  $u_\infty^{k_j}$  generated by the scattering of the two incident plane waves  $u_j^{\text{inc}}(x) = e^{ik_j x \cdot d}$  with fixed direction  $d$  and wavenumbers  $k_a$  and  $k_b$ , where  $k_a < k_b$ , by an unknown convex object  $D$  with homogeneous Dirichlet boundary condition, such that the wavenumbers  $k_a$  and  $k_b$  are not in the resonance region of the object, reconstruct the shape of  $D$ .*

As we pointed out previously, for the inverse methods presented in this thesis, as the frequency of the incident plane wave increases, the initial guess should be closer to the object. Without a good initial guess, we are not able to apply the method presented in Chapter 2.

In order to generate a good initial guess, we present here an idea that can be considered a globalization technique. We obtain a better initial guess for the object by solving the problem using data for low frequencies. In Section 5.3.1, we present a procedure based on the Kirchhoff approximation formula that allows us to generate far field data for wavenumbers lower than  $k_a$ . The data generated has better quality for higher frequencies, and is better in the illuminated part of the object. In Section 5.3.2, using the data generated by a new procedure, we present a method to obtain a good initial guess of the illuminated part of the object. This good initial guess can be used to recover the object using Method B presented in Chapter 2. We show some numerical results at the end of this chapter.

## 5.1 Direct problem at frequencies out of the resonance region for convex objects

### 5.1.1 The Kirchhoff approximation formula

We will consider the scattering of an incident plane wave by a strictly convex obstacle  $D$ , where we have a frequency out of the resonance region. In this case, instead of solving integral equations like (3), we use the Kirchhoff approximation for the scattered field. Using the Kirchhoff approximation for the scattered field together with the stationary phase method for high oscillatory integrals, we are able to obtain a formula to approximate the far field pattern of the object. To obtain this approximation, we use a similar approach to [31].

We begin with a few definitions, including those of the illuminated and shadowed parts of an object.

**Definition 5.1.1** *Take  $\nu(x)$  to be the outward-pointing vector normal to  $\partial D$  at the point  $x \in \partial D$ . The illuminated part of the object  $D$  by a wave with incidence direction  $d$  is defined to be*

$$\partial D_d^+ = \{x \in \partial D : d \cdot \nu(x) < 0\},$$

*and the shadowed part is defined to be*

$$\partial D_d^- = \{x \in \partial D : d \cdot \nu(x) \geq 0\}.$$

**Definition 5.1.2** Given a plane wave with incidence direction  $d$  to a convex object  $D$ , the shadow points of the convex object  $D$  are the points  $x_s^1$  and  $x_s^2$  such that

$$d \cdot \nu(x_s^j) = 0, \quad (58)$$

for  $j = 1, 2$ .

As we can see from the definitions, the boundary of the sets  $\partial D^+$  and  $\partial D^-$  is comprised of the shadow points of the convex object  $D$  generated by the incident plane wave  $u^{\text{inc}}$ .

We also have the following definition for a specular point:

**Definition 5.1.3** Given an incidence direction  $z$ , we define the specular point  $x_z \in \partial D_z^+$  as the point such that

$$x_z \cdot z = \min_{x \in \partial D_z^+} x \cdot z.$$

Because we consider only convex objects  $D$ , the specular point  $x_z$  is unique.

Supposing that the object  $D$  is illuminated by an incident plane wave with direction  $z = (z_1, z_2)$ , the equation of the line tangent to the resulting illuminated part  $\partial D_z^+$  of the object at the specular point  $x_z$  is:

$$z_1 x_1 + z_2 x_2 = x_z \cdot z.$$

Consequently, we have the following relation for the normal vector at the specular point:

$$\nu(x_z) = -z. \quad (59)$$

For the case where we have the frequency out the resonance region, we can approximate the normal derivative of the far field using the Kirchhoff approximation. In the Kirchhoff approximation, we have

$$\frac{\partial u}{\partial \nu}(x) = \begin{cases} 2 \frac{\partial u^{\text{inc}}}{\partial \nu}(x), & \text{for } x \in \partial D_d^+ \\ 0, & \text{for } x \in \partial D_d^-. \end{cases} \quad (60)$$

Using the approximation (60) in Equation (52), we obtain:

$$u_\infty^{\text{kirc}}(\hat{x}) = -\frac{e^{i\pi/4}}{\sqrt{2\pi k}} \int_{\partial D_d^+} \frac{\partial u^{\text{inc}}}{\partial \nu}(x) e^{-ik\hat{x} \cdot x} ds(x). \quad (61)$$

Substituting the incident plane wave into Equation (61), we obtain:

$$u_\infty^{\text{kirc}}(\hat{x}) = \frac{e^{-i\pi/4} \sqrt{k}}{\sqrt{2\pi}} \int_{\partial D_d^+} d \cdot \nu(x) e^{ik(d-\hat{x}) \cdot x} ds(x).$$

Parameterizing the set  $\partial D$  with the function  $x(t) : [0, 2\pi] \rightarrow \mathbb{R}^2$ , we obtain the integral

$$u_{\infty}^{\text{kirc}}(\hat{x}) = \frac{e^{-i\pi/4}\sqrt{k}}{\sqrt{2\pi}} \int_{t_1^+}^{t_2^+} d \cdot \nu(x(t)) e^{ik(d-\hat{x}) \cdot x(t)} |x'(t)| dt, \quad (62)$$

where  $t_1^+$  and  $t_2^+$  are the boundary points of the domain  $\partial D_d^+$  for the parameterization variable  $t$ .

Take  $\tau \in [t_1^+, t_2^+]$  such that  $x(\tau)$  is the specular point of the object illuminated by an incident plane wave with direction  $z = \frac{d-\hat{x}}{|d-\hat{x}|}$ . We have that

$$\nu(x(\tau)) = -\frac{d-\hat{x}}{|d-\hat{x}|}. \quad (63)$$

Take the function

$$g(t) = (d-\hat{x}) \cdot x(t), \quad (64)$$

therefore its first derivative is

$$g'(t) = (d-\hat{x}) \cdot x'(t), \quad (65)$$

and its second derivative is

$$g''(t) = (d-\hat{x}) \cdot x''(t). \quad (66)$$

Plugging the specular point  $x(\tau)$  into Equation (65) and using (63) we obtain

$$\begin{aligned} g'(\tau) &= (d-\hat{x}) \cdot x'(\tau) \\ &= \nu(x(\tau)) \cdot x'(\tau) |d-\hat{x}| \\ &= 0. \end{aligned}$$

We call  $\tau$ , where  $g'(\tau) = 0$ , the stationary point of the function  $g(t)$ . Since the object  $D$  is convex,  $\tau$  is the unique non-degenerate stationary point of  $g(t)$  on the illuminated part of the object, which means that  $g'(\tau) = 0$ , and  $g''(\tau) \neq 0$ .

The integral in Equation (62) has a high oscillatory kernel with the exception of the region around the stationary point. To solve this integral, we use the stationary phase method [32]. We have the following theorem about the stationary phase method [32] that will be used to obtain our formula for the far field pattern of the object  $D$ :

**Theorem 5.1.1** *Suppose  $g(t)$  is a  $C^2([0, 2\pi])$  function,  $g''(t) \neq 0$ , and  $g'(\tau) = 0$ , where  $\tau$  is the stationary point. Then*

$$\int_a^b f(t) e^{ikg(t)} dt = f(\tau) \exp \left[ ikg(\tau) + \frac{i\pi}{4} \frac{g''(\tau)}{|g''(\tau)|} \right] \sqrt{\frac{2\pi}{k|g''(\tau)|}} \left[ 1 + \mathcal{O}\left(\frac{1}{k}\right) \right],$$

as  $k \rightarrow \infty$ .

**Proof:** See [32]. □

The strict convexity of  $D$  implies that  $\tau$  is the unique point where  $g(t)$  attains a minimum in the illuminated part of the object, and that

$$\frac{g''(\tau)}{|g''(\tau)|} = 1. \quad (67)$$

Applying the theorem above on Equations (62) and (67), we obtain

$$u_{\infty}^{\text{kirc}}(\hat{x}) = \frac{d \cdot \nu(x(\tau))}{\sqrt{|(d - \hat{x}) \cdot x''(\tau)|}} |x'(\tau)| e^{ik(d - \hat{x}) \cdot x(\tau)} [1 + \mathcal{O}(k^{-1})], \quad (68)$$

as  $k \rightarrow \infty$ .

Because  $d \cdot d = \hat{x} \cdot \hat{x} = 1$ , we have

$$(d - \hat{x}) \cdot \hat{x} = -(d - \hat{x}) \cdot d.$$

We also have

$$2d \cdot (d - \hat{x}) = |d - \hat{x}|^2. \quad (69)$$

Using (63) and (69) in (68), we get from [70]

$$u_{\infty}^{\text{kirc}}(\hat{x}) = -\frac{1}{2} \sqrt{\frac{|d - \hat{x}|}{|-\nu(x(\tau)) \cdot x''(\tau)|}} e^{ik(d - \hat{x}) \cdot x(\tau)} |x'(\tau)| [1 + \mathcal{O}(k^{-1})].$$

We define the curvature of a smooth curve  $\partial D$  as

$$\kappa(t) = -\frac{\nu(x(t)) \cdot x''(t)}{|x'(t)|^2}. \quad (70)$$

Using (70), we can write the following approximation  $\tilde{u}_{\infty}(\hat{x}) \approx u_{\infty}^{\text{kirch}}(\hat{x})$  of the far field pattern:

$$\tilde{u}_{\infty}(\hat{x}) = -\frac{1}{2} \sqrt{\frac{|d - \hat{x}|}{\kappa(\tau)}} e^{ik(d - \hat{x}) \cdot x(\tau)}, \quad (71)$$

as  $k \rightarrow \infty$ . From now on, we use  $\tilde{u}_{\infty}$  to refer to the far field pattern obtained using the Kirchhoff approximation.

We define the far field operator  $K(x; \hat{x}) : \mathbb{X}_c \times \Omega \rightarrow L^2(\Omega)$  for frequencies out of the resonance region as

$$K(x; \hat{x}) = -\frac{1}{2} \sqrt{\frac{|d - \hat{x}|}{\kappa(\tau)}} e^{ik(d-\hat{x}) \cdot x(\tau)}, \quad (72)$$

where the domain is parameterized by  $x \in \mathbb{X}_c$ , where  $\mathbb{X}_c$  is the set of parameterizations of convex obstacles, and  $\Omega$  is the unit circle with center at the origin. In this chapter, to keep notation consistent with the other chapters, we abuse notation by writing  $K(x; \hat{x}) = K_{x_r}(\hat{x})$  every time we use a star-shaped domain with parameterization  $x(t) = x_r(t)(\cos(t), \sin(t))$ .

## 5.1.2 Numerical implementation and results

We present examples comparing the Kirchhoff approximation with the Nyström method presented in Chapter 3 applied to different objects at different frequencies. In all scenarios presented, the incident plane wave has a relatively high wavenumber compared to the object's size, and it illuminates the convex part of the object.

### Example 5.1.1 Comparison of the Nyström method and the Kirchhoff approximation

In this example, we have the following configuration: a plane wave with direction  $d$  and wavenumber  $k$  is incident at a convex object  $D$ . We calculate the far field pattern at the points  $\hat{x}_l = 2\pi(l-1)/N_{ff}$ , for  $l = 1, \dots, N_{ff}$  using the Kirchhoff approximation (72) and the Nyström method as in Chapter 3. Since we want to see detailed graphs of the far field pattern, we pick  $N_{ff} = 640$ .

We present three scenarios:

- In the first scenario, the object  $D$  is the unit circle centered at the origin, to which we refer as  $S^1$ , and the plane wave has the incidence direction  $d = (1, 0)$  and wavenumber  $k = 10$ . We present the results in Figure 5.1. In Figures 5.1(a) and 5.1(b), the real and imaginary parts of the far field pattern for the two solutions are presented, in blue we have the solution given by the Nyström method and in red we have the solution given by the Kirchhoff approximation. In Figures 5.1(c) and 5.1(d), the absolute value of the difference of the real and imaginary parts of the solution given by the Nyström method and the Kirchhoff approximation is shown. Note that in Figures 5.1(c) and 5.1(d) the  $y$ -axis uses the log scale.
- In this scenario, the object  $D$  has the parameterization  $x : [0, 2\pi] \rightarrow \mathbb{R}^2$ , with  $x(t) = (3 + 0.15 \cos(3t))(\cos(t), \sin(t))$ . For the sake of simplicity we call this object the Egg. The incidence direction and wavenumber are  $d = (1, 0)$  and  $k = 10$ . In Figure 5.2, we have the results for this scenario. In Figures 5.2(a) and 5.2(b), the real and imaginary parts of the far field pattern for the two solutions are presented: in blue we have the solution given by the Nyström method and in red we have the solution given by the

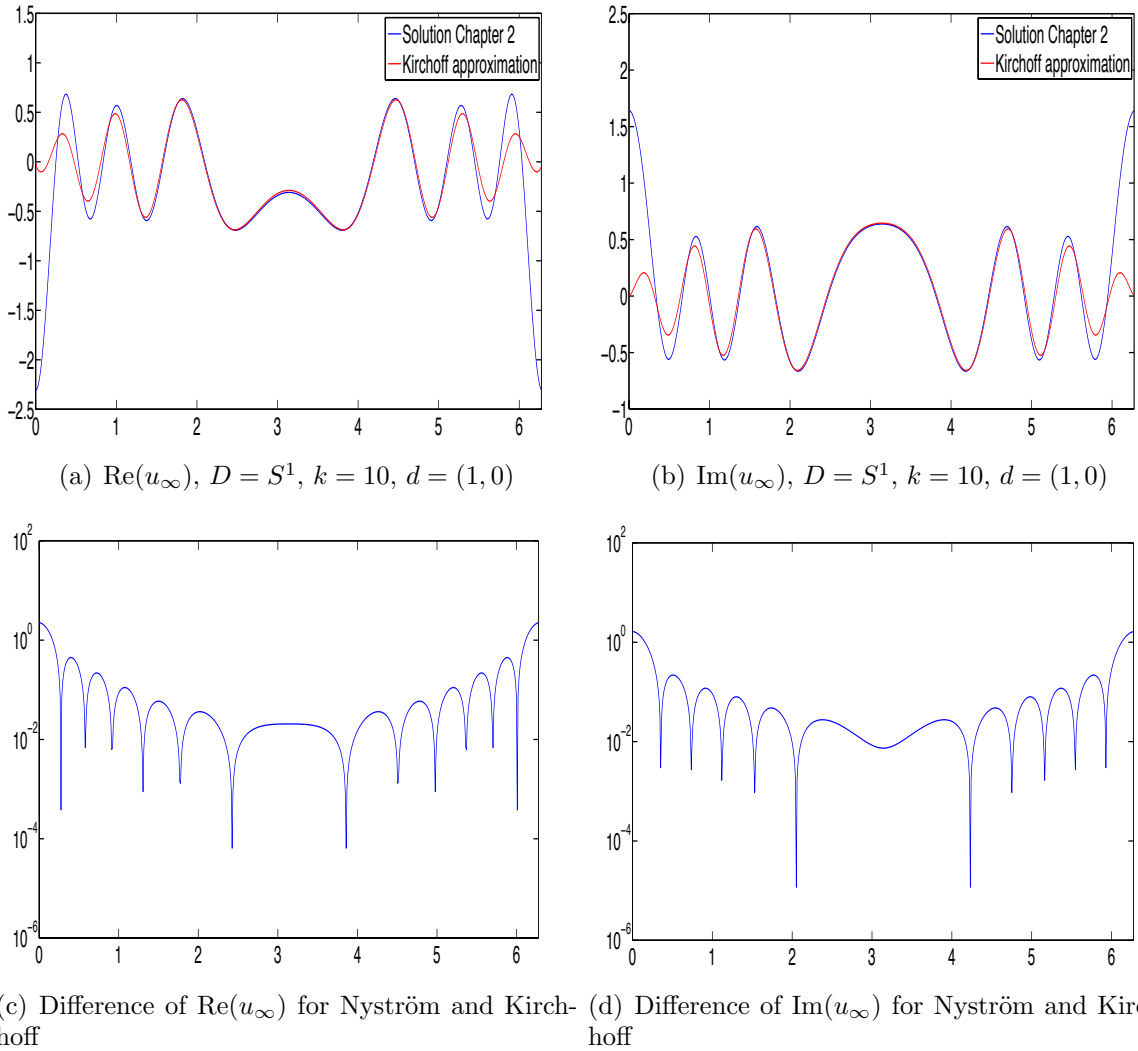


Figure 5.1: Comparison of the far field pattern obtained for the circle  $S^1$  with  $k = 10$  and  $d = (1, 0)$  by the Nyström method and by the Kirchhoff approximation. In (a) and (b) we have respectively the real and imaginary parts of the far field pattern, where blue is used for the Nyström method and red for the Kirchhoff approximation. In (c) and (d) we have respectively the absolute value of the difference between the real and imaginary parts of the solutions given by the Nyström method and the Kirchhoff approximation. Note that we have a log scale on the  $y$ -axis of the graphs.

Kirchhoff approximation. In Figures 5.2(c) and 5.2(d), the absolute value of the difference of the real and imaginary parts of the solution given by the Nyström method and the Kirchhoff approximation are shown. Note that in Figures 5.2(c) and 5.2(d) the  $y$ -axis uses the log scale.

- Finally, we take the non-convex object  $D$  to be the Kite, and we assume an incident plane wave with incidence direction  $d = (-1, 0)$  and wavenumber  $k = 20$ . We note that the illuminated part goes from  $t = \pi/2$  to  $t = 3\pi/2$ , and this part of the Kite

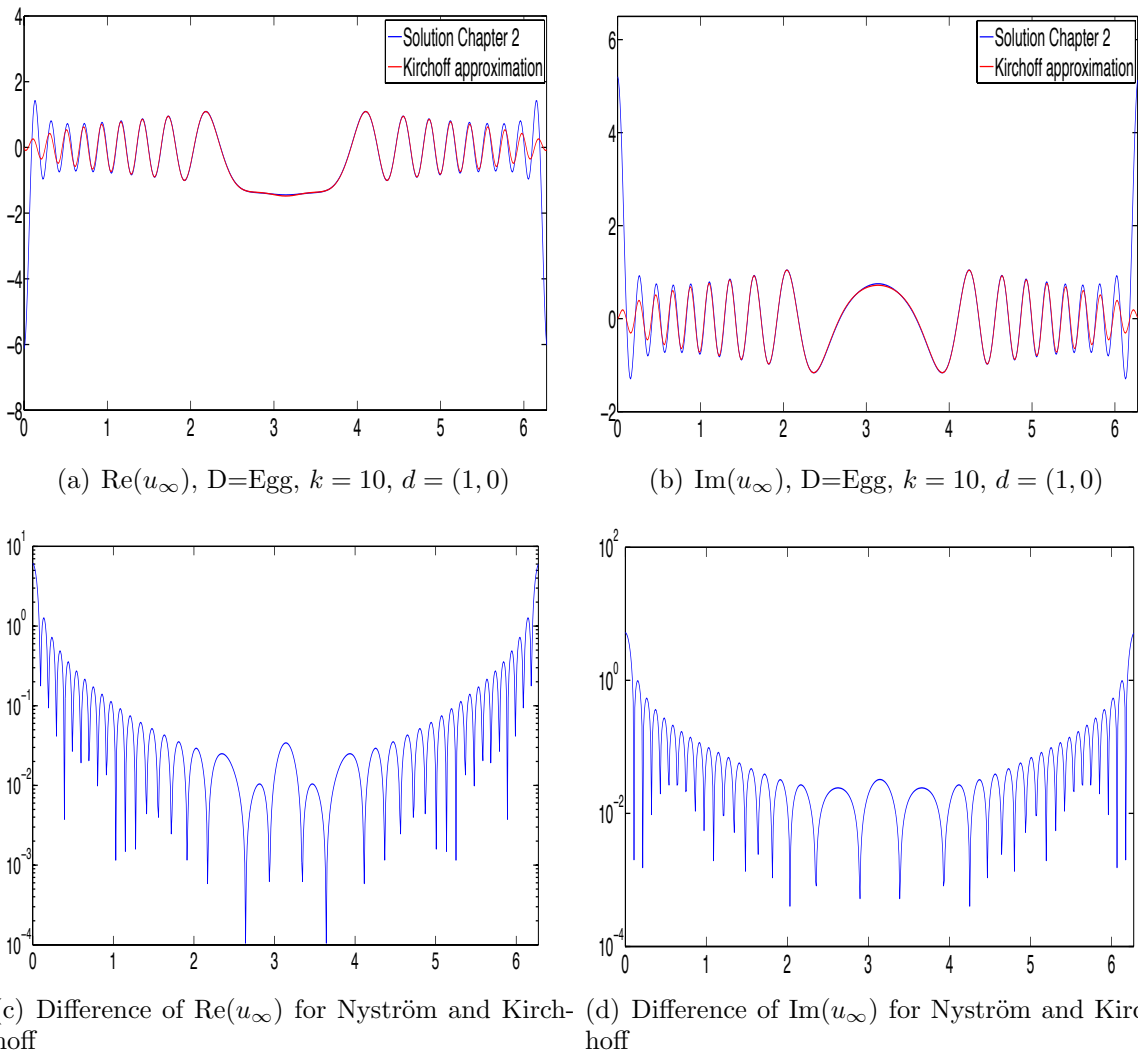


Figure 5.2: Comparison of the far field pattern obtained for the Egg with  $k = 10$  and  $d = (1, 0)$  by the Nyström method and by the Kirchhoff approximation. In (a) and (b) we have respectively the real and imaginary parts of the far field pattern, where blue is used for the Nyström method and red for the Kirchhoff approximation. In (c) and (d) we have respectively the absolute value of the difference between the real and imaginary parts of the solutions given by the Nyström method and the Kirchhoff approximation. Note that we have a log scale on the  $y$ -axis of the graphs.

is convex. The results are in Figure 5.3. In Figures 5.3(a) and 5.3(b), the real and imaginary parts of the far field pattern for the two solutions are presented: in blue we have the solution given by the Nyström method and in red we have the solution given by the Kirchhoff approximation. In Figures 5.3(c) and 5.3(d), the absolute value of the difference of the real and imaginary parts of the solution given by the Nyström method and the Kirchhoff approximation is shown. Note that in Figures 5.3(c) and 5.3(d) the  $y$ -axis uses the log scale.

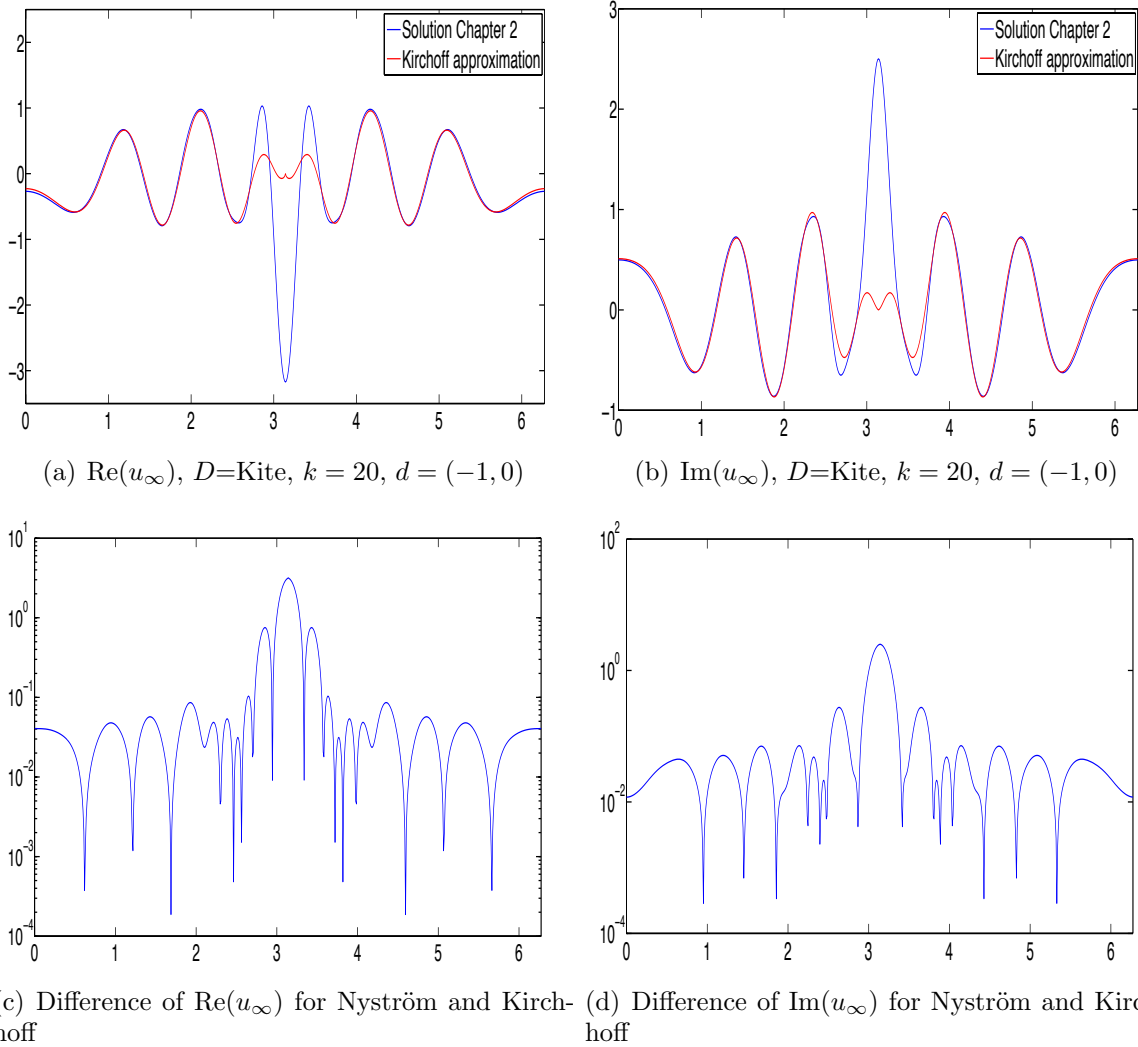


Figure 5.3: Comparison of the far field pattern obtained for the Kite with  $k = 20$  and  $d = (-1, 0)$  by the Nyström method and by the Kirchhoff approximation. In (a) and (b) we have respectively the real and imaginary parts of the far field pattern, where blue is used for the Nyström method and red for the Kirchhoff approximation. In (c) and (d) we have respectively the absolute value of the difference between the real and imaginary parts of the solutions given by the Nyström method and the Kirchhoff approximation. Note that we have a log scale on the  $y$ -axis of the graphs.

We see from Figures 5.1, 5.2 and 5.3 that the Kirchhoff approximation yields good results in the illuminated part of the object, and its accuracy deteriorates in the shadowed part of the object. We observe that the Kirchhoff approximation works only for convex objects, or in problems such that the part of the object illuminated by the incoming plane wave is convex.

## 5.2 Inverse problems using the Kirchhoff approximation formula

### 5.2.1 Inverse problem for single frequency using the Kirchhoff approximation formula

In Section 5.1, we follow the steps of [31; 71] and use the Kirchhoff approximation for the scattered field and the stationary phase method for highly oscillatory integrals to obtain formula (72) that allows us to calculate an approximation  $\tilde{u}_\infty$  of the far-field pattern of the convex object  $D$ , which has great accuracy for frequencies out of the resonance region in the illuminated part of the object, as was shown in Example 5.1.2.

In this section, we present an algorithm based on the far field pattern approximation formula (72) for the reconstruction of the shape of the convex object  $D$  using the far field pattern measured  $u_\infty$  at the points  $\hat{x}_l \in \Omega^+$ , for  $l = 1, \dots, \tilde{N}_{ff}$ , where  $\Omega^+ \subset \Omega$  and  $\Omega^+$  is the set where the approximation formula of the far field pattern (72) can be used to obtain a good approximation of the far field pattern. This means that we expect that the higher the wavenumber, the smaller is the set  $\Omega^+$ .

The algorithm proposed is an iterative two-step procedure. For the sake of simplicity, we refer to this method based on the Kirchhoff approximation formula as Method C.

Before describing Method C, we need to define the solution set for the domains that we use in this problem. We define the space of strictly convex domains  $\mathbb{X}_{N_r, c} \subset \mathbb{X}_{N_r}$  such that

$$\mathbb{X}_{N_r, c} = \{x_r : [0, 2\pi] \rightarrow \mathbb{R} \mid x_r(t) \in \mathbb{X}_{N_r}, \kappa(t) > 0 \text{ and } x_r(t) > 0, t \in [0, 2\pi]\},$$

where  $\kappa(t)$  is the curvature of the the domain  $\partial D$  with parameterization

$$x(t) = x_r(t)(\cos(t), \sin(t)).$$

The outline of Method C for the inverse scattering problem is as follows:

1. Choose an initial guess  $\partial D^{(0)}$  with parameterization  $x^{(0)} = x_r^{(0)}(\cos(t), \sin(t))$ , with  $x_r^{(0)} \in \mathbb{X}_{N_r, c}$ .
2. Repeat until the stopping criterion is reached:
  - (a) Use the two-step procedure based on Equation (72) with the parameterization  $x^{(j)} = x_r^{(j)}(\cos(t), \sin(t))$ , with  $x_r^{(j)} \in \mathbb{X}_{N_r, c}$  to obtain a new parameterization of the domain  $x^{(j+1)} = x_r^{(j+1)}(\cos(t), \sin(t))$ , updating  $x^{(j)}$ , such that  $x_r^{(j+1)} \in \mathbb{X}_{N_r, c}$ .

Next, we describe the two-step procedure used by Method C:

1. Suppose we have a parameterization  $x^{(j)}(t) = x_r^{(j)}(t)(\cos(t), \sin(t))$  approximating the boundary  $\partial D$ . We calculate the specular points  $x^{(j)}(\tau_l) \in x^{(j)}$  for the vectors  $z_l = \frac{d - \hat{x}_l}{|d - \hat{x}_l|}$ ,  $l = 1, \dots, \tilde{N}_{ff}$ , solving the problem

$$\tau_l = \operatorname{argmin}_{\tau \in \partial D_{z_l}^+} x^{(j)}(\tau) \cdot \frac{d - \hat{x}_l}{|d - \hat{x}_l|}, \quad (73)$$

where  $\partial D_{z_l}^+$  is the part illuminated by the vector  $z_l$ . Since we are looking for the specular point on the illuminated part of a strictly convex object with boundary  $\partial D^{(j)}$ , the solution for (73) is unique.

2. In the next step, using the specular points  $x^{(j)}(\tau_l)$  of the curve  $x^{(j)}$  for the vectors  $\frac{d - \hat{x}_l}{|d - \hat{x}_l|}$ , define the residue function  $\tilde{r} : \mathbb{X}_{N_r, c} \rightarrow L^2(\Omega)$  as

$$\tilde{r}(x_r) = K_{x_r}(\hat{x}) - u_\infty(\hat{x}),$$

where  $x(t) = x_r(t)(\cos(t), \sin(t))$ , and the functional

$$\tilde{f}(x_r) = \frac{1}{2} \|\tilde{r}(x_r)\|_{L^2(\Omega)}^2.$$

We solve the following problem:

$$\min_{x_r \in \mathbb{X}_{N_r, c}} \tilde{f}(x_r), \quad (74)$$

where  $\mathbb{X}_{N_r, c}$  is the set of trigonometric polynomials for convex domains.

As we see, the two-step procedure of Method C is computationally much less expensive than the two-step procedure used for Methods A and B. Finding the roots in the first step of Method C is computationally less expensive than solving the integral equations (3) for the first step of Methods A and B.

This problem is nonlinear, so instead of minimizing the function  $\tilde{f}(x)$ , we minimize the first order approximation around  $x_r^{(j)}$ ,

$$\tilde{M}^{(j)}(x_r) = K_{x_r^{(j)}} + \tilde{J}(x_r^{(j)})(x - x_r^{(j)}), \quad (75)$$

where  $\tilde{M}^{(j)} : \mathbb{X}_{N_r, c} \rightarrow L^2(\Omega)$  is the first-order model approximation of  $\tilde{f}$  and  $\tilde{J}(x_r^{(j)})$  is the Fréchet derivative of  $K_{x_r}$  with respect to the domain  $x^{(j)}$ .

To obtain the linear approximation of  $\tilde{r}(x_r)$  around  $x_r^{(j)}$ , we have the following theorem:

**Theorem 5.2.1** *Suppose the curvature of the boundary of the scatterer  $\partial D$  is greater than zero in the illuminated part  $\partial D^+$ , which means that the part of the object illuminated by the incoming plane wave is convex. The domain derivative of (72) considering*

the specular points to be fixed is given by

$$\begin{aligned} \partial_x (K_x(\hat{x})) h = & -\frac{\sqrt{|d-\hat{x}|}}{2} e^{ik(d-\hat{x})\cdot x(\tau)} \left\{ \frac{ik [(d-\hat{x})\cdot h]}{\sqrt{|\kappa(\tau)|}} + \frac{3}{2} \frac{x' \cdot h'}{\sqrt{|x'_1 x''_2 - x'_2 x''_1| |x'|}} \right. \\ & \left. + \frac{|x'|^{3/4} h'' \cdot (x'_2, -x'_1) + x'' \cdot (h'_2, -h'_1)}{(x'_1 x''_2 - x'_2 x''_1)^{3/2}} \right\}, \end{aligned} \quad (76)$$

where  $x(t) = (x_1(t), x_2(t))$ ,  $\partial_x$  represents the domain derivative operator, and  $h = (h_1, h_2)$  is very small.

**Proof:** Apply the definition of the Fréchet derivative, and the result follows from a long series of calculations.  $\square$

Approximating  $\tilde{f}(x_r)$  by  $\bar{f}(x_r)$ , where  $\bar{f}(x_r)$  is the right hand side of Equation (75), we obtain the problem

$$\min_{x_r \in \mathbb{X}_{N_r, c}} \bar{f}(x_r). \quad (77)$$

The operator obtained using several values of  $\hat{x}_l$  is ill-posed. We must use a regularization technique like in the previous section to solve Equation (77). Instead of solving Equation (77), we define the Tikhonov functional

$$\bar{f}(x_r) = \frac{1}{2} \|\tilde{M}^{(j)}(x_r)\|_{L^2(\Omega)}^2 + \frac{1}{2} \lambda \|x - x^{(j)}\|_{H^1(\Omega)}^2,$$

where  $x(t) = x_r(t)(\cos(t), \sin(t))$ , and solve the following problem:

$$\min_{x_r \in \mathbb{X}_{N_r, c}} \bar{f}(x_r), \quad (78)$$

where  $\lambda > 0$  is a regularization parameter, chosen such that the problem is not ill-posed.

In the same fashion as for Method B, to solve (78) we use a Gauss-Newton method and obtain the update for each step

$$h_r = - \left( \tilde{J}(x_r^{(j)})^* \tilde{J}(x_r^{(j)}) + \lambda^{(j)} I^p \right)^{-1} \tilde{J}(x_r^{(j)})^* \tilde{r}(x_r^{(j)}), \quad (79)$$

where  $I^p$  is the identity operator for the  $H^p$ -norm.

After finding  $h_r$ , we must update  $x_r^{(j)} = x_r^{(j)} + h_r$ , but as there is no guarantee that the new parameterization obtained by the polynomial  $x_r^{(j)} + h_r$  will yield a convex object, we must project the obtained result onto the space  $\mathbb{X}_{N_r, c}$ . We define the operator  $P_{\mathbb{X}_{N_r, c}} : \mathbb{X}_{N_r} \rightarrow \mathbb{X}_{N_r, c}$  as

$$P_{\mathbb{X}_{N_r, c}}(x_r^{(j)} + h_r) \in \mathbb{X}_{N_r, c}.$$

The implementation of this operator is showed in detail in the next section.

We update the domain, setting  $x_r^{(j)} = P_{\mathbb{X}_{N_r, c}}(x_r^{(j)} + h_r)$ .

## 5.2.2 Numerical implementation of Method C

Suppose we know the measures  $u_\infty(\hat{x}_l)$  of the far field pattern at the points  $\hat{x}_l \in \Omega$ , for  $l = 1, \dots, N_{ff}$ , where  $\Omega$  is the unit circle. First, we show how to numerically implement the two step procedure of Method C.

Assume that the object  $D$  can be parameterized  $x^{(j)}(t) = x_r^{(j)}(t)(\cos(t), \sin(t))$ , with  $x_r^{(j)}(t) \in \mathbb{X}_{N_r, c}$ .

1. For the first step, we solve Equation (73) to find the specular point for the vectors

$$z_l = \frac{d - \hat{x}_l}{|d - \hat{x}_l|}.$$

We find the shadow boundary points  $x_{l,s_1}$  and  $x_{l,s_2}$ , such that

$$\nu(x_{l,s_j}) \cdot z_l = 0,$$

for  $j = 1, 2$ . To solve this equation, we can apply a root-finding method, like the secant method, the Newton method or the bisection method. We uniformly discretize the domain  $[0, 2\pi]$  with the points  $t_n = n2\pi/N_n$ . We apply this division of the domain  $[0, 2\pi]$  in subintervals, and in each subinterval, we use the bisection method to verify the existence of a root, followed by a Newton method on those intervals with roots. Finding the two roots of the equation, we obtain the set  $\partial D_{z_l}^+$ . This gives us our constraint set for (73).

Since we are looking for the minimum of the function

$$x^{(j)}(\tau) \cdot \frac{d - \hat{x}_l}{|d - \hat{x}_l|}, \quad (80)$$

we set its derivative equal to zero and find the root of the equation

$$(x^{(j)})'(\tau) \cdot \frac{d - \hat{x}_l}{|d - \hat{x}_l|} = 0. \quad (81)$$

Once we obtain the roots for Equation (81) we apply our constraint that the point must be in  $\partial D_{z_l}^+$ . Since the object is strictly convex, our solution will be the unique point  $x(\tau_l)$  for each vector  $z_l$ .

2. For the second step, we solve Equation (79) for each of the vectors  $z_l$  and the respective specular points  $\tau_l$ . This will give a total of  $\tilde{N}_{ff}$  equations. Putting those equations together, we obtain the linear system

$$\left( \tilde{\mathbf{J}}(\mathbf{x}_r^{(j)})^* \tilde{\mathbf{J}}(\mathbf{x}_r^{(j)}) + \lambda^{(j)} \mathbf{I} \mathbf{P} \mathbf{h}_r \right) = -\tilde{\mathbf{J}}(\mathbf{x}_r^{(j)})^* \tilde{\mathbf{r}}(\mathbf{x}_r^{(j)}),$$

where

- $\mathbf{x}_r^{(j)} = (a_0^{(j)}, a_1^{(j)}, \dots, a_{N_r}^{(j)}, b_1^{(j)}, \dots, b_{N_r}^{(j)})$  is the vector that has as components the coefficients of the polynomial  $x_r^{(j)}(t) = a_0^{(j)} + \sum_{n=1}^{N_r} (a_n^{(j)} \cos(nt) + b_n^{(j)} \sin(nt))$ ;
- $\mathbf{I}^p$  is the matrix of the  $H^p$ -norm as in Chapter 4;
- $\tilde{\mathbf{r}}(\mathbf{x}_r^{(j)})$  is the vector with components  $\tilde{r}(x_r^{(j)}(\tau_l))$ , where  $\tau_l$  is the specular point for  $z_l$  for  $l = 1, \dots, \tilde{N}_{ff}$ ;
- $\tilde{\mathbf{J}}(\mathbf{x}_r^{(j)})$  is the  $\tilde{N}_{ff} \times N_r$  matrix with elements  $j_{ln}$ , where  $j_{ln}$  refers to the derivative at the point  $\tau_l$ ,  $l = 1, \dots, \tilde{N}_{ff}$  of the function related to the coefficients of the trigonometric polynomial  $x^{(j)}(t)$ , where  $n = 1, \dots, 2N_r + 1$ , as follows:
  - $n = 1$  refers to the constant function 1;
  - $n = 2, \dots, N_r + 1$  refers to the terms  $\cos(nt)$ ; and
  - $n = N_r + 2, \dots, 2N_r + 1$  refers to the terms  $\sin(nt)$ ; and
- $\tilde{\mathbf{J}}(\mathbf{x}_r^{(j)})^*$  is the adjoint matrix of  $\tilde{\mathbf{J}}(\mathbf{x}_r^{(j)})$ .

With respect to the projection operator  $P_{\mathbb{X}_{N_r, c}}$ , we implement a heuristic algorithm to obtain a convex parameterization for the domain  $\partial D^{(j)}$ . The procedure is the following:

- We discretize the domain  $[0, 2\pi]$  with  $N_{\text{obj}}$  points, getting  $t_m = m2\pi/N_{\text{obj}}$ , for  $m = 1, \dots, N_{\text{obj}} - 1$ .
- Next, we obtain the points  $x^{(j)}(t_m) = x_r^{(j)}(t_m)(\cos(t_m), \sin(t_m))$ , using the points  $t_m$ . Let us say that we obtain an  $N_{\text{obj}} \times 2$  matrix where the first column has respectively the values of the  $x$  and  $y$  coordinates of the points  $x^{(j)}(t_m)$ .
- We apply the MATLAB function `convhull` to obtain the convex hull of the points  $x^{(j)}(t_m) \in \mathbb{R}^2$ . This function uses the `quickhull` algorithm, of which a detailed description can be found in [72]. The `convhull` function gives us the points that form the convex hull of the domain  $\partial D^{(j)}$ ; this set of points, called  $\mathcal{CV}(\partial D^{(j)})$ , forms a subset of the original set of points  $x^{(j)}(t_m)$ .
- We create the  $N_{\text{obj}} \times 2$  matrix  $\mathbf{P}$ , with elements such that if  $x^{(j)}(t_m) \in \mathcal{CV}(\partial D^{(j)})$ , then  $P_{m,1} = x_r^{(j)}(t_m) \cos(t_m)$  and  $P_{m,2} = x_r^{(j)}(t_m) \sin(t_m)$ . For the components such that  $x^{(j)}(t_m) \notin \mathcal{CV}(\partial D^{(j)})$ , we make a linear extrapolation of the points. In detail, if we have two consecutive points in the convex hull  $x^{(j)}(t_{m_1})$  and  $x^{(j)}(t_{m_2})$ , we perform the following:
  - If  $t_{m_2} = t_{m_1} + 2\pi/N_{\text{obj}}$ , we do not take any action.
  - If  $t_{m_2} > t_{m_1} + 2\pi/N_{\text{obj}}$ , we calculate the number of the initial  $x^{(j)}(t_m)$  points that are not included in the set  $\mathcal{CV}(\partial D^{(j)})$ . Say we have  $\tilde{N}_{\text{obj}}$  points between the points  $t_{m_1}$  and  $t_{m_2}$ . Since we have a star-shaped object, there is a one-to-one relation between the  $\tilde{N}_{\text{obj}}$  points that are not in the set  $\mathcal{CV}(\partial D^{(j)})$  and the straight line between the points  $x^{(j)}(t_{m_1})$  and  $x^{(j)}(t_{m_2})$ . We call those points  $\bar{x}^{(j)}(t_m)$ , from  $m = m_1 + 1, \dots, m_2 - 1$ . Finally, we set for those points

$$P_{m,1} = \bar{x}_r^{(j)}(t_m) \cos(t_m) \text{ and } P_{m,2} = \bar{x}_r^{(j)}(t_m) \sin(t_m).$$

- Given the polynomial  $\tilde{x}_r^{(j)}(t) = a_{0,p} + \sum_{m=1}^{N_r} (a_{m,p} \cos(mt) + b_{m,p} \sin(mt))$ , we have the equations  $\tilde{x}_r^{(j)}(t_m) \cos(t_m) = P_{m,1}$  and  $\tilde{x}_r^{(j)}(t_m) \sin(t_m) = P_{m,2}$ , that give a system of  $2N_{\text{obj}}$  equations in  $N_r$  variables, the coefficients of the polynomial  $\tilde{x}_r^{(j)}$ . To solve this system, we use the least squares method. (Remembering to always use  $N_{\text{obj}} > N_r$ .)

**Remark 5.2.1** *This algorithm does not necessarily give us a convex object. If we want to improve the results, we can apply this algorithm iteratively, until we are satisfied with the result. A problem with this algorithm occurs when we try to approximate the points  $P_m$  by the trigonometric polynomial  $\tilde{x}_r^{(j)}$ . It is very difficult to control the oscillatory behavior of the trigonometric polynomial. To overcome this problem, one can use a trigonometric polynomial with a low  $N_r$ . Again, there is no guarantee that the object obtained is convex.*

**Remark 5.2.2** *Another choice is to use B-splines instead of using trigonometric polynomials. The results obtained suffer from the same problem as those obtained using trigonometric polynomials. We believe that is possible to obtain a better projection algorithm using B-splines, but it would be necessary to develop a CAD tool to generate convex objects.*

**Remark 5.2.3** *With respect to the choice of the parameter  $\lambda$ , we advise choosing the residue times  $2\epsilon_{\hat{x}}/N_{ff}$ .*

After presenting the two-step procedure, we summarize Method C.

**Algorithm 5.2.1 (Method C)**

1. Choose an initial guess for the domain  $\partial D^{(0)}$  with a parameterization  $x^{(0)} = x_r^{(0)}(\cos(t), \sin(t))$ .
2. Repeat the two-step procedure to update  $\mathbf{x}^{(j+1)} = \mathbf{P}_{N_r, c}(\mathbf{x}^{(j)} + \mathbf{h}_r)$  until the stopping criteria are reached.

Figure 5.4: Implementation of the iterative method for solving the inverse problem for an object  $D$  with Dirichlet boundary conditions using single frequency far field pattern measures.

**Remark 5.2.4** *With respect to the stopping criteria, the same ones used in the previous chapters can be applied. Another criterion that can be applied is that if the quality of the approximation decreases in a certain number of steps, which means that the residue increases in those steps, we could stop the method.*

### 5.2.3 The special case of the circle with fixed center

We consider the special case in which the object  $D$  that we try to reconstruct is the circle of radius  $R$  and center at the origin. We choose the initial guess to solve this problem as the circle with parameterization  $x^{(0)} = x_r^{(0)}(\cos(t), \sin(t))$ , where we have  $x_r^{(0)} = a_0^{(0)} \in \mathbb{R}$ . We search for the solution in the space

$$\mathbb{X}_0 = \{x_r(t)(\cos(t), \sin(t)) : x_r(t) = a_0 \in \mathbb{R}\}. \quad (82)$$

Since we are looking for solutions in the space of circles, the solution of the Equation (73) is constant and equal to

$$\tau_l = \frac{d - \hat{x}_l - \pi}{2} + n\pi, \quad (83)$$

where  $n \in \mathbb{Z}$ ,  $x^{(j)}(\tau_l) \in \partial D^{(j),+}$ , for  $l = 1, \dots, N_{ff}$ , where  $\partial D^{(j),+}$  is the illuminated part of the object  $\partial D^{(j)}$  by the vector with direction  $z_l = \frac{d - \hat{x}_l}{|d - \hat{x}_l|}$ .

Since the specular points are the same in all steps, the method becomes only the solution of the second step of the two-step procedure. The problem becomes the application of the Newton method for a one dimensional parameter.

The curvature of the object is constant and equal to  $1/a_0^{(j)}$ . We also have that

$$(d - \hat{x}_l) \cdot y(\tau) = -2a_0^{(j)} \cos(n\pi) \cos(\theta_l) \sin\left(\frac{\theta_d - \theta_l}{2}\right), \quad (84)$$

where  $\theta_d = \arctan(d)$ ,  $\theta_l = \arctan(\hat{x}_l)$  and  $n \in \mathbb{Z}$ .

Using (83) and (84), the operator  $K_x$  at the point  $\hat{x}_l$  becomes

$$K_{x_r}(\hat{x}_l) = -\frac{1}{2} \sqrt{a_0^{(j)} |d - \hat{x}_l|} e^{-ik2a_0^{(j)} \cos(n\pi) \cos(\theta_l) \sin\left(\frac{\theta_d - \theta_l}{2}\right)},$$

and its derivative  $J_{x_r} = \partial_x(K_{x_r})$  with respect to the domain variable is

$$J_{x_r^{(j)}}(\hat{x}) = -A(\hat{x}, d) e^{-ik2a_0^{(j)} \cos(n\pi) \cos(\theta_l) \sin\left(\frac{\theta_d - \theta_l}{2}\right)} \left[ \frac{1}{2\sqrt{a_0^{(j)}}} - 2ik \cos(n\pi) \sqrt{a_0^{(j)}} \cos(\theta_l) \sin\left(\frac{\theta_d - \theta_l}{2}\right) \right],$$

where

$$A(\hat{x}, d) = \frac{\sqrt{|d - \hat{x}_l|}}{2}.$$

Since we seek the radius of the circle, we must restrict our search to a positive real value. We have  $N_{ff}$  measures for the far field pattern  $u_\infty$  of the object, and as each measure is in  $\mathbb{C}$ , this constitutes  $2N_{ff}$  equations for our problem in  $\mathbb{R}$ . This gives us an overdetermined system of equations. The real and imaginary parts of the operator  $J_{x^{(j)}}(\hat{x})$  are

$$\operatorname{Re} \left( J_{x_r^{(j)}} \right) (\hat{x}) = -A(\hat{x}, d) \left[ \frac{\cos(2rk \cos(n\pi))}{2\sqrt{r}} - 2k \cos(n\pi) \sqrt{r} \sin(2rk \cos(n\pi)) \right],$$

and

$$\operatorname{Im} \left( J_{x_r^{(j)}} \right) (\hat{x}) = A(\hat{x}, d) \left[ \frac{\sin(2rk \cos(n\pi))}{2\sqrt{r}} + 2k \cos(n\pi) \sqrt{r} \cos(2rk \cos(n\pi)) \right],$$

for any  $\hat{x}$ . If we take the real and imaginary parts of  $J_{x_r^{(j)}}(\hat{x})$  for all  $\hat{x}_l$ , we obtain a vector with  $2N_{ff}$  components.

**Remark 5.2.5** *As we are approximating the object by a circle at each step, it is not necessary to project the solution into a convex object.*

Suppose our incident plane wave has direction  $d = (1, 0)$ . Since we are looking only for one variable (the radius), it suffices to use one measure of the far field pattern; then we take  $N_{ff} = 1$ . We use the measure of the far field pattern at  $\hat{x}_1 = (-1, 0)$ , which gives us a system of two equations and one unknown. For this problem,  $z_1 = (1, 0)$ , and its specular point is  $\tau_1 = \pi$ .

In this particular setting, we prove a result relating the frequency of the incident wave to the size of the region where we choose our initial guess and obtain convergence to the right solution with the method. We start by presenting a general result by Kantorovich for the Newton method:

**Theorem 5.2.2 (Newton-Kantorovich)**

*Let  $X$  and  $Y$  be Banach spaces and  $F : D \subset X \rightarrow Y$ . Suppose that on an open convex set  $D_0 \subset D$ ,  $F$  is Fréchet differentiable and*

$$\|F'(x) - F'(y)\| \leq L\|x - y\|, \quad x, y \in D_0. \quad (85)$$

*For some  $x_0 \in D_0$ , assume that  $\Gamma_0 \equiv [F'(x_0)]^{-1}$  is defined on all of  $Y$  and that  $h \equiv \beta L \eta \leq 1/2$ , where  $\|\Gamma_0\| \leq \beta$  and  $\|\Gamma_0 F x_0\| \leq \eta$ . Set*

$$\begin{aligned} t^* &= \frac{1}{\beta K} \left( 1 - \sqrt{1 - 2h} \right) \\ t^{**} &= \frac{1}{\beta K} \left( 1 + \sqrt{1 - 2h} \right) \end{aligned}$$

*and suppose that  $S = \{x \mid \|x - x_0\| \leq t^*\} \subset D_0$ . Then the Newton iterates  $x_{k+1} = x_k - [F'(x_k)]^{-1} F(x_k)$ ,  $k = 0, 1, \dots$ , are well defined, lie in  $S$ , and converge to a solution  $x^*$  of  $Fx = 0$  that is unique in  $D_0 \cap \{x \mid \|x - x_0\| < t^{**}\}$ . Moreover, if  $h < 1/2$ , the order of convergence is at least quadratic.*

**Proof:** The proof can be found in [73–75]. □

For the sake of notation, let us define the operator  $\mathcal{K} : I \subset \mathbb{R}^+ \rightarrow \mathbb{R}$  such that

$$\mathcal{K}(x) = (\operatorname{Re}(J_x))^2 + (\operatorname{Im}(J_x))^2.$$

From simple calculations we have that

$$\mathcal{K}(x) = \frac{1}{2} \left( \frac{1}{4x} + 4k^2x \right).$$

We have the following lemmas regarding properties of the function  $\mathcal{K}$ :

**Lemma 5.2.1** *For the function  $\mathcal{K}$  in the open convex set  $I = [a, b]$ , where  $a, b > 0$ , the following inequality holds:*

$$|\mathcal{K}(x) - \mathcal{K}(y)| \leq L|x - y|, \tag{86}$$

where

$$L = \frac{1 + 32k^2a^2b}{8a^2}. \tag{87}$$

**Proof:** We have that

$$\begin{aligned} |\mathcal{K}(x) - \mathcal{K}(y)| &= \frac{1}{2} \left| \frac{1}{4x} + 4k^2x^2 - \left( \frac{1}{4y} + 4k^2y^2 \right) \right| \\ &\leq \frac{1}{8} \left| \frac{1}{x} - \frac{1}{y} \right| + 2k^2|x^2 - y^2| \\ &\leq \frac{1}{8|xy|}|x - y| + 2k^2|x + y||x - y| \\ &\leq \left( \frac{1}{8|xy|} + 2k^2|x + y| \right) |x - y|. \end{aligned}$$

□

**Lemma 5.2.2** *Consider  $\Gamma_0 = [\mathcal{K}(x_0)]$ . We have the following inequality regarding  $\Gamma_0$  in the open convex set  $I = [a, b]$ , where  $a, b > 0$ , for the point  $x_0 \in D$ :*

$$\beta \leq \frac{1}{2x_0k^2},$$

where  $\beta = |\Gamma_0|$ .

**Proof:** We have that

$$\begin{aligned} |\Gamma_0| &= \left| [\mathcal{K}(x_0)]^{(-1)} \right| \\ &= \frac{8x_0}{1 + 16k^2x_0^2} \\ &\leq \frac{1}{2k^2x_0}. \end{aligned}$$

□

**Lemma 5.2.3** For the far field pattern  $\tilde{u}_\infty(\hat{x})$ , its Euclidean norm  $\|\tilde{u}(\hat{x})\|$ , and the function

$$F(x) = \begin{bmatrix} \operatorname{Re}(J_x) & \operatorname{Im}(J_x) \end{bmatrix} \begin{bmatrix} \operatorname{Re}(K(x) - \tilde{u}_\infty) \\ \operatorname{Im}(K(x) - \tilde{u}_\infty) \end{bmatrix},$$

we have that  $\|\Gamma_0 F(x_0)\| \leq \eta$ , where

$$\eta = \frac{1}{2k^2 x_0} \left[ \frac{1}{4} + kx_0 + \left( \frac{\sqrt{2}}{4\sqrt{x_0}} + k\sqrt{2r} \right) \|\tilde{u}_{\hat{x}}\| \right].$$

**Proof:** The proof follows from Lemma 5.2.2 and the fact that

$$\|\Gamma_0 F x_0\| \leq \left[ \frac{1}{4} + kx_0 + \left( \frac{\sqrt{2}}{4\sqrt{x_0}} + k\sqrt{2r} \right) \|\tilde{u}_{\hat{x}}\| \right]. \quad (88)$$

□

Suppose that the object  $D$  is a circle of radius  $R$  centered at the origin. We have the following theorem concerning our method.

**Theorem 5.2.3** The size of the interval  $S$  on which the presented method converges is  $\mathcal{O}(1/k)$ .

**Proof:** We apply Lemmas 5.2.1, 5.2.2, 5.2.3 and simple calculations to the formulas for  $t^*$  and  $t^{**}$  in the Newton-Kantorovich Theorem.

We have that  $\beta L = \mathcal{O}(1)$  and  $h \equiv \beta L \eta = \mathcal{O}(1/k)$ . Using this in the formulas for  $t^*$  and  $t^{**}$ , and using the Taylor expansion series for the square roots, we obtain

$$t^* = \mathcal{O}\left(\frac{1}{k}\right),$$

and

$$t^{**} = C - \mathcal{O}\left(\frac{1}{k}\right),$$

where  $C$  is a real constant. □

Next, we present an example showing the dependence of the interval of convergence of Method C on the inverse of the wavenumber.

**Example 5.2.1** Checking the influence of the wavenumber on the interval of convergence.

To illustrate the dependence of the convergence interval on the wavenumber of the incidence plane wave, consider the following scenario. The object  $D$  that we want to reconstruct is the circle with center at the origin and radius  $R$ . The incident plane wave has wavenumber  $k$  and incidence direction  $d = (1, 0)$ . We have one far field pattern measure at the point  $\hat{x}_1 = (-1, 0)$ . We consider two types of measures for the far field pattern:  $u_\infty$  given by the

$k$	Radius = 1	Radius = 2	Radius = 4	Radius = 8
1	(0.00,2.57)	(0.66,3.57)	(2.50,5.57)	(6.46,9.57)
2	(0.33,1.78)	(1.25,2.78)	(3.23,4.78)	(7.22,8.78)
4	(0.63,1.39)	(1.62,2.39)	(3.61,4.39)	(7.61,8.39)
8	(0.81,1.19)	(1.81,2.19)	(3.81,4.19)	(7.81,8.19)
16	(0.90,1.10)	(1.90,2.10)	(3.90,4.10)	(7.90,8.10)
32	(0.95,1.05)	(1.95,2.05)	(3.95,4.05)	(7.95,8.05)

Table 5.1: We consider the reconstruction of the circle with radius  $R$  and center at the origin. We have the far field at the point  $\hat{x} = (-1, 0)$  generated by an incident plane wave with incidence direction  $d = (1, 0)$  and wavenumber  $k$ . We present for the radius  $R = 1, 2, 4$  and 8 and the wavenumbers  $k = 1, 2, 4, 8, 16$  and 32 the interval of convergence of Method C, using as the far field pattern measurement  $u_\infty$  the measure generated using the integral equations of Chapter 2.

$k$	Radius = 1	Radius = 2	Radius = 4	Radius = 8
1	(0.00,2.67)	(0.71,3.63)	(2.53,5.60)	(6.48,9.58)
2	(0.36,1.81)	(1.27,2.80)	(3.24,4.79)	(7.23,8.79)
4	(0.63,1.40)	(1.62,2.39)	(3.62,4.39)	(7.61,8.39)
8	(0.81,1.20)	(1.81,2.20)	(3.81,4.20)	(7.81,8.20)
16	(0.90,1.10)	(1.90,2.10)	(3.90,4.10)	(7.90,8.10)
32	(0.95,1.05)	(1.95,2.05)	(3.95,4.05)	(7.95,8.05)

Table 5.2: We consider the reconstruction of the circle with radius  $R$  and center at the origin. We have the far field at the point  $\hat{x} = (-1, 0)$  generated by an incident plane wave with incidence direction  $d = (1, 0)$  and wavenumber  $k$ . We present for the radius  $R = 1, 2, 4$  and 8 and the wavenumbers  $k = 1, 2, 4, 8, 16$  and 32 the interval of convergence of Method C, using as the far field pattern measurement  $\tilde{u}_\infty$  the measure generated using the Kirchhoff approximation formula (72).

integral equations of Chapter 2 and  $\tilde{u}_\infty$  given by the Kirchhoff approximation formula. We consider the radius  $R = 1, 2, 4$  and 8 and the wavenumbers  $k = 1, 2, 4, 8, 16$  and 32. We obtained for each combination of radius  $R$  and wavenumber  $k$  the interval of convergence of the method, which means that if we choose as initial guess for the radius of the circle to approximate this problem a value in this interval, it will converge to the solution. In Table 5.1, we present for each wavenumber  $k$  and radius  $R$  the interval of convergence using Method C with  $N_r = 0$  and the far field pattern  $u_\infty$ . In Table 5.2, we present for each wavenumber  $k$  and radius  $R$  the interval of convergence using Method C to find the circle using  $N_r = 0$  and the far field pattern  $\tilde{u}_\infty$ .

We see that in both tables the size of the interval of convergence decreases with the wavenumber at a rate of  $1/k$ . The results are very similar for both choices of the measures used for the far field pattern.

## 5.3 Globalization technique for frequencies out of the resonance region

### 5.3.1 Generating synthetic data

As seen in the previous section and also in Chapter 3, the choice of the initial guess is related to the frequency of the data available. If we have low frequency data from the far field, we can approximate the object with a simple initial guess that is not necessarily close to the desired object. On the other hand, if the far field pattern of the object is generated by a higher frequency incident plane wave, our initial guess must be close to the object to provide an accurate reconstruction of the shape of the object. In Chapter 3, we present a multi-frequency method that was able to reconstruct the detailed shape of an object using far field data generated by incident waves with different frequencies.

Unfortunately, far field data from several frequencies is not always available. Sometimes, we have an even more restrictive situation, where we have only a few measurements of the far field data for frequencies out of the resonance region. Solving the inverse problem of shape reconstruction of the object using this data would require an initial guess very close to the object. This initial guess is not available most of the time.

In this section, we present a procedure to generate synthetic low frequency far field data using a pair of measures of the far field pattern obtained at frequencies out of the resonance region. In this procedure, we use an extrapolation operator based on the approximated formula for the Kirchhoff approximation to generate a low frequency far field pattern from the given frequencies far field patterns, where those frequencies are out of the resonance region. The quality of the data generated by this extrapolation operator is better in the illuminated part of the object.

Using the far field formula (71) obtained from the application of the Kirchhoff approximation, we calculate the ratio of the far field pattern generated by the Kirchhoff approximation for two wavenumbers  $k$  and  $k + \delta k$ ,  $\delta k > 0$ , and obtain:

$$\tilde{q}_{k,k+\delta k} = \frac{\tilde{u}_{\infty}^{k+\delta k}}{\tilde{u}_{\infty}^k} = e^{i[(d-\hat{x})\cdot x(\tau)]\delta k}. \quad (89)$$

In Equation (71), notice that according to our approximation, in some range for the frequency, we can assume that the amplitude of the far field pattern is constant and has the value

$$A(u_{\infty}^k) = -\frac{1}{2} \sqrt{\frac{|d - \hat{x}|}{\kappa(\tau)}}. \quad (90)$$

If we choose a  $k_{\text{new}}$  big enough, we can say that the value of the amplitude of the generated far field data is equal to (90).

Using the ratio of the two frequencies (89), and supposing that  $\delta k$  is smaller than the order of magnitude of the size of the object, we can obtain the approximation  $\tilde{u}_\infty^{k_{\text{new}}}$  of the far field pattern at frequency  $k_{\text{new}}$  by setting

$$\tilde{u}_\infty^{k_{\text{new}}} = A(u_\infty^k)(e^{\arg(q_{k,k+\delta k})})^{k_{\text{new}}/\delta k}. \quad (91)$$

The function  $g(\tau) = (d - \hat{x}) \cdot x(\tau)$  in (89) is continuous on the illuminated part of the object and since the object is strictly convex, all its values of  $g$  have the same sign if  $\hat{x} \neq d$ .

We have  $\delta k g(\tau) = 2n_{g(\tau)}\pi + \theta_{g(\tau)}$ , where  $\theta_{g(\tau)} \in [0, 2\pi]$  and  $n_{g(\tau)} \in \mathbb{Z}$ . Depending on the value of  $\delta k$ , we obtain different values for the integer  $n_{g(\tau)}$ . If we have  $n_{g(\tau)} \neq 0$  then  $e^{2n_{g(\tau)}\pi + \theta_{g(\tau)}} = e^{\theta_{g(\tau)}}$ , which can be a problem because we can lose the information on  $n_{g(\tau)}$  and consequently obtain the wrong phase when raising the argument of the ratio  $q_{k,k+\delta k}$  to the power  $k_{\text{new}}/\delta k$ .

To address this problem, we must choose our  $\delta k$  such that  $0 < |(d - \hat{x}) \cdot x(\tau)| \delta k \leq 2\pi$ . For  $x(t) = x_r(t)(\cos(t), \sin(t))$ , the idea is to choose  $\delta k > 0$  such that

$$\delta k \leq \frac{2\pi}{\max |d - \hat{x}| \max x_r(t)}.$$

Choosing  $\delta k$  in the interval  $\left[0, \frac{2\pi}{\max |d - \hat{x}| \max x_r(t)}\right]$  gives us  $n_{g(\tau)} = 0$ . In this case, there is no danger of having jumps in the phase of the generated data. Normally, we do not possess accurate estimates of the size of the object, in which case we advise the use of a small  $\delta k$ .

Finally, we define the extrapolation operator:

**Definition 5.3.1** *Suppose we have far field pattern measurements  $\tilde{u}_\infty^{k_j}$  at the points  $\hat{x}_l$ , for  $j = 1, 2$  and  $l = 1, \dots, \tilde{N}_{ff}$ , where  $k_1 = k$  and  $k_2 = k + \delta k$  are frequencies outside of the resonance region. We define the operator  $\tilde{\mathcal{I}}_{k,\delta k}^{k_{\text{new}}} : \mathbb{C}^2 \rightarrow \mathbb{C}$  such that*

$$\tilde{\mathcal{I}}_{k,\delta k}^{k_{\text{new}}}(\tilde{u}_\infty^k, u_\infty^{k+\delta k}) = A(u_\infty^k)(e^{\arg(q_{k,k+\delta k})})^{k_{\text{new}}/\delta k} = \tilde{u}_\infty^{k_{\text{new}}} \quad (92)$$

*that takes as input the two far field measures for  $k_1$  and  $k_2$  and gives as a result an estimation  $\tilde{u}_\infty^{k_{\text{new}}}$  of the far field pattern generated by the deflection of an incident plane wave with frequency  $k_{\text{new}}$ , and measured at the points  $\hat{x}_l$ , for  $l = 1, \dots, \tilde{N}_{ff}$ , using formula (91).*

The extrapolation operator is supposed to yield an approximation of the far field pattern at the wavenumber  $k_{\text{new}}$ , as we were calculating the far field pattern at this wavenumber using the Kirchhoff approximation.

We do not know the measures  $\tilde{u}_\infty^k$  and  $\tilde{u}_\infty^{k+\delta k}$  given by the Kirchhoff approximation; instead, we are given measures of the far field patterns  $u_\infty^k$  and  $u_\infty^{k+\delta k}$ . In this case, we calculate the ratio

$$q_{k,k+\delta k} = \frac{u_\infty^{k+\delta k}}{u_\infty^k} = \frac{\tilde{u}_\infty^{k+\delta k} + \mathcal{O}\left(\frac{1}{k+\delta k}\right)}{\tilde{u}_\infty^k + \mathcal{O}\left(\frac{1}{k}\right)}. \quad (93)$$

If  $k \rightarrow \infty$  then  $q_{k,k+\delta k} \rightarrow \tilde{q}_{k,k+\delta k}$ .

Instead of using the operator  $\tilde{\mathcal{I}}_{k,\delta k}^{k_{\text{new}}}$  to obtain an estimation of the far field pattern at the wavenumber  $k_{\text{new}}$ , we define the operator  $\mathcal{I}_{k,\delta k}^{k_{\text{new}}} : \mathbb{C}^2 \rightarrow \mathbb{C}$  such that

$$\mathcal{I}_{k,\delta k}^{k_{\text{new}}}(u_{\infty}^k, u_{\infty}^{k+\delta k}) = A(u_{\infty}^k)(e^{\arg(q_{k,k+\delta k})})^{k_{\text{new}}/\delta k}. \quad (94)$$

We define the right hand side of (94) as  $\bar{u}_{\infty}^{k_{\text{new}}}$ . From now on we use  $\bar{u}_{\infty}$  to refer to the far field pattern obtained using the data generation procedure presented in this section.

Note here that if we use the ratio  $\tilde{q}_{k,k+\delta k}$  in the operator  $\mathcal{I}_{k,\delta k}^{k_{\text{new}}}$ , we obtain the operator  $\tilde{\mathcal{I}}_{k,\delta k}^{k_{\text{new}}}$ , hence the data obtained is exactly the same as if we were calculating the far field pattern using the Kirchhoff approximation formula (71).

**Remark 5.3.1** *This approximation works only in the illuminated part of convex objects. The quality of the approximation of the synthetic data is better in the illuminated part closer to the specular point, whereas close to the shadow boundary and to the shadowed part, the approximation is not of good quality.*

Next, we show examples of this approximation for different objects.

**Example 5.3.1** *Comparison of the far field pattern generated by the extrapolation operator and obtained by the Nyström method.*

We present the following scenario for different convex objects  $D$  in this example. We have incident plane waves with fixed incidence direction  $d = (1, 0)$ , and wavenumbers  $k_a$  and  $k_b$ . We obtain the far field pattern at the points  $\hat{x}_l = 2l\pi/N_{ff}$ ,  $N_{ff} = 2048$ . Using the extrapolation operator (92), we generate the approximation  $\bar{u}_{\infty}^{k_m}$ , with  $k_m$ , for  $m = 0, 1, 2$  at the same points  $\hat{x}_l$ . We also calculate the far field pattern using the Nyström method for comparison with the results obtained with our extrapolation operator. We compare the generated data by the procedure presented in this section with the data obtained using the Nyström method presented in Chapter 3 and the data obtained by the Kirchhoff formula (71). We show the absolute error for the real and imaginary parts of the data generated with respect to the far field pattern given by the Nyström method, respectively:

$$e_{\text{abs}}^{\text{Re}} = |\text{Re}(u_{\infty}) - \text{Re}(\bar{u}_{\infty})| \quad \text{and} \quad e_{\text{abs}}^{\text{Im}} = |\text{Im}(u_{\infty}) - \text{Im}(\bar{u}_{\infty})|,$$

and the relative error for the real and imaginary parts of the data generated with respect to the far field pattern given by the Nyström method, respectively:

$$e_{\text{rel}}^{\text{Re}} = \frac{|\text{Re}(u_{\infty}) - \text{Re}(\bar{u}_{\infty})|}{|u_{\infty}|}, \quad \text{and} \quad e_{\text{rel}}^{\text{Im}} = \frac{|\text{Im}(u_{\infty}) - \text{Im}(\bar{u}_{\infty})|}{|u_{\infty}|},$$

We also show the absolute error for the real and imaginary parts of the data generated with respect to the far field pattern given by the Kirchhoff approximation, respectively:

$$\tilde{e}_{\text{abs}}^{\text{Re}} = |\text{Re}(\tilde{u}_\infty) - \text{Re}(\bar{u}_\infty)| \quad \text{and} \quad \tilde{e}_{\text{abs}}^{\text{Im}} = |\text{Im}(\tilde{u}_\infty) - \text{Im}(\bar{u}_\infty)|,$$

and the relative error for the real and imaginary parts of the data generated with respect to the far field pattern given by the Kirchhoff approximation, respectively:

$$\tilde{e}_{\text{rel}}^{\text{Re}} = \frac{|\text{Re}(\tilde{u}_\infty) - \text{Re}(\bar{u}_\infty)|}{|u_\infty|}, \quad \text{and} \quad \tilde{e}_{\text{rel}}^{\text{Im}} = \frac{|\text{Im}(\tilde{u}_\infty) - \text{Im}(\bar{u}_\infty)|}{|u_\infty|}.$$

1. First, we consider the object  $D$  to be the ellipse with parameterization

$$x(t) = (3 \cos(t), 4 \sin(t)),$$

with  $t \in [0, 2\pi]$ . We take the wavenumbers of the given data to be  $k_a = 19$  and  $k_b = 20$ , and we generate the far field data for wavenumbers  $k_m = 2 + 6m$ . We present the results in Figure 5.5. We have the real and imaginary parts respectively of the far field patterns  $u_\infty$ ,  $\bar{u}_\infty$  and  $\tilde{u}_\infty$  in (a) and (b) for  $k = 2$ , (c) and (d) for  $k = 8$ , and (e) and (f) for  $k = 14$ . In Figure 5.6, we present the graphs of the absolute error for the real and imaginary parts with respect to the far field obtained using the Nyström method of the data generated in (a) for  $k = 2$ , (c) for  $k = 8$  and (e) for  $k = 14$ . In the same figure, we have the relative error for the real and imaginary parts with respect to the far field obtained using the Nyström method of the data generated in (b) for  $k = 2$ , (d) for  $k = 8$  and (f) for  $k = 14$ . In Figure 5.7, we present the graphs of the absolute error for the real and imaginary parts with respect to the Kirchhoff approximation of the data generated in (a) for  $k = 2$ , (c) for  $k = 8$  and (e) for  $k = 14$ . In the same figure, we have the relative error for the real and imaginary parts with respect to the Kirchhoff approximation of the data generated in (b) for  $k = 2$ , (d) for  $k = 8$  and (f) for  $k = 14$ .

2. Next, suppose  $D$  has the parameterization  $x(t) = x_r(t)(\cos(t), \sin(t))$ , with  $x_r(t) =$  and  $t \in [0, 2\pi]$ . From now on, we refer to this object as the Egg. We take the wavenumbers of the given data to be  $k_a = 11$  and  $k_b = 12$ , and we generate the far field data for wavenumbers  $k_m = 2 + 4m$ . The results are in Figure 5.8. We have the real and imaginary parts respectively of the far field patterns  $u_\infty$ ,  $\bar{u}_\infty$  and  $\tilde{u}_\infty$  in (a) and (b) for  $k = 2$ , (c) and (d) for  $k = 6$ , and (e) and (f) for  $k = 10$ . In Figure 5.9, we present the graphs of the absolute error for the real and imaginary parts with respect to the far field obtained using the Nyström method of the data generated in (a) for  $k = 2$ , (c) for  $k = 6$  and (e) for  $k = 10$ . In the same figure, we have the relative error for the real and imaginary parts with respect to the far field obtained using the Nyström method of the data generated in (b) for  $k = 2$ , (d) for  $k = 6$  and (f) for  $k = 10$ . In Figure 5.10, we present the graphs of the absolute error for the real and imaginary parts with respect to the Kirchhoff approximation of the data generated in (a) for  $k = 2$ , (c) for  $k = 6$  and (e) for  $k = 10$ . In the same figure, we have the relative error for the real and imaginary parts with respect to the Kirchhoff approximation of the data generated in (b) for  $k = 2$ , (d) for  $k = 6$  and (f) for  $k = 10$ .

3. Finally, we assume the object  $D$  to be the Kite. For the sake of simplicity and to keep the incidence direction  $d = (1, 0)$  constant in this example, we rotate the Kite 180 degrees. In this configuration, the illuminated part of the Kite is convex. We take the wavenumbers of the given data to be  $k_a = 14$  and  $k_b = 15$ , and we generate data for wavenumbers  $k_m = 2 + 5m$ . We present the results in Figure 5.11. We have the real and imaginary parts respectively of the far field patterns  $u_\infty$ ,  $\bar{u}_\infty$  and  $\tilde{u}_\infty$  in (a) and (b) for  $k = 2$ , (c) and (d) for  $k = 7$ , and (e) and (f) for  $k = 12$ . In Figure 5.12, we present the graphs of the absolute error for the real and imaginary parts with respect to the far field obtained using the Nyström method of the data generated, in (a) for  $k = 2$ , (c) for  $k = 7$  and (e) for  $k = 12$ . In the same figure, we have the relative error for the real and imaginary parts with respect to the far field obtained using the Nyström method of the data generated in (b) for  $k = 2$ , (d) for  $k = 7$  and (f) for  $k = 12$ . In Figure 5.13, we present the graphs of the absolute error for the real and imaginary parts with respect to the Kirchhoff approximation of the data generated in (a) for  $k = 2$ , (c) for  $k = 7$  and (e) for  $k = 12$ . In the same figure, we have the relative error for the real and imaginary parts with respect to the Kirchhoff approximation of the data generated in (b) for  $k = 2$ , (d) for  $k = 7$  and (f) for  $k = 12$ .

Note that in the figures depicting the errors, we use the log-scale on the  $y$ -axis, also, since the object is symmetric, we present the results only for half of the domain, in this case for  $[0, \pi]$ , we do the same for the other figures in this example, with the exemption of the figures relative to the Kite. Since the object is not convex, we used the domain interval  $[\pi/2, \pi]$  in the figures related to the configuration with the Kite.

We see from this example that the quality of the data generated depends on the wavenumber  $k_{\text{new}}$  at which we are generating the new data and the position  $\hat{x}$  for which we are generating the data with relation to the illuminated part of the object.

With respect to the frequency, the data generated is better for higher frequencies than for low frequencies; this is a consequence of the fact that the Kirchhoff approximation formula used for generating the data is used for the approximate calculation of the field for high frequencies.

The data generated is of better quality close to the point where the incident plane wave hits the object, and in an area around it that increases with frequency. The quality of the data generated deteriorates going to the shadow boundary, and in our case, completely deteriorates outside the interval  $[\pi/2, 3\pi/2]$ . This is due to the effect of the diffraction of the incident wave, which is not accounted for by the Kirchhoff approximation.

### 5.3.2 Inverse problem for multiple frequency using Kirchhoff approximation

In this section, we consider the solution of Problem 3, where we know the far field pattern  $u_\infty^{k_j}$  at the points  $\hat{x}_l \in \Omega$ ,  $l = 1, \dots, N_{\text{inc}}$  generated by the deflection of two incident waves with

wavenumbers  $k_a$  and  $k_b$ , with  $k_a < k_b$ , and incidence direction  $d$ , and we want to reconstruct the shape of a sound-soft convex obstacle  $D$ . The frequency of the two incident plane waves are assumed to be outside of the resonance region of the object.

Since Methods A and B presented in Chapter 4 and Method C presented in this chapter are iterative methods related to the Newton method, it is very important to have an initial guess close enough to obtain a good approximation of the object. By Theorem 2.2.3, there is a relation between the size of the interval for choosing the initial guess and the frequency used to solve the inverse problem. This means that if the frequency is too high, we need to have an initial guess very close to the object as seen in Chapter 4. We intend to use the far field data generator of the previous section to remedy this setback.

Due to the high quality of approximation of the generated data  $\bar{u}_\infty^{k_{\text{new}}}$ , it is possible to use our data generating procedure together with the RLA presented in Chapter 4 to obtain a good approximation of convex objects.

First, we intend to use the operators  $\mathcal{I}_{k_{N_{\text{inc}}+1}, k_{N_{\text{inc}}+2}}^{k_m}$  to generate the far field pattern  $\bar{u}_\infty^{k_m}$  at the points  $\hat{x}_l$  for  $m = 1, \dots, N_{\text{inc}}$  and  $l = 1, \dots, N_{ff}$ , such that  $k_1 < k_2 < \dots < k_{N_{\text{inc}}} < k_{N_{\text{inc}}+1} < k_{N_{\text{inc}}+2}$ .

Since the generated far field data is not of good quality for all values of  $\hat{x}$  in the domain  $\Omega$ , we choose a positive real constant  $\epsilon_{\hat{x}}$  such that we use the data generated at the points  $\hat{x}_l = (\cos(t_l), \sin(t_l))$  with  $\theta - \epsilon_{\hat{x}} \leq t_l \leq \theta + \epsilon_{\hat{x}}$ , where the angle  $\theta \equiv \theta_d + \pi \pmod{2\pi}$  and  $\theta_d$  is the angle such that the incidence plane wave direction is  $d = (\cos(\theta_d), \sin(\theta_d))$ . Using this restriction, we have the far field generated data at the points  $\hat{x}_{\tilde{l}}$ , for  $\tilde{l} = 1, \dots, \tilde{N}_{ff}$  for solving the inverse problem.

This new data  $\bar{u}_\infty^{k_m}$  can be considered the data generated by the object in case we used the Kirchhoff approximation formula. It makes sense, then, to use the method developed in Section 5.2.1 to solve the inverse problem with the data generated by the Kirchhoff formula.

We propose a method based on the RLA method of Chapter 4.

**Algorithm 5.3.1 Method RLA-C:**

1. We start by choosing an initial guess  $x^{(0)} = x_r^{(0)}(\cos(t), \sin(t))$  and an initial solution set  $\mathbb{X}_{N_r^{(1)}, c}$ .
2. For  $m = 1$  to  $N_{\text{inc}}$  do
  - Given the generated far field pattern  $\bar{u}_\infty^{k_m}$  at the points  $\hat{x}_{\tilde{l}}$ , for  $\tilde{l} = 1, \dots, \tilde{N}_{ff}$ , use Method C to obtain an approximation  $x^{(m)} = x_r^{(m)}(\cos(t), \sin(t))$  with the initial guess  $x^{(m-1)}$ .
3. Choose the final solution set  $\mathbb{X}_{N_r^{(2)}}$  and project the solution onto that space.

4. For  $m = N_{inc} + 1$  to  $m = N_{inc} + 2$  do

- Given the generated far field pattern  $u_\infty^{k_m}$  at the points  $\hat{x}_l$ , for  $l = 1, \dots, N_{ff}$ , use Method B to obtain an approximation  $x^{(m)} = x_r^{(m)}(\cos(t), \sin(t))$  with the initial guess  $x^{(m-1)}$ .

The RLA-C method can be seen as a procedure for obtaining a good initial guess to use in the RLA method with wavenumbers  $k_{N_{inc}+1}$  and  $k_{N_{inc}+2}$ : we can even consider it a globalization technique for the RLA method. In the next section, we present some results for the RLA-C method. We also try to implement an alternative to the RLA-C method where we would use Method B instead of Method C for the single frequency problems at wavenumbers  $k_1, \dots, k_{N_{inc}}$ . This alternative method did not present satisfactory results and these results are not considered here.

### 5.3.3 Numerical results using the RLA-C method

In this section, we present some results obtained from our method and compare them to those obtained using the multi-frequency method presented in Chapter 4.

#### Example 5.3.2 Results for the RLA-C method

We assume two incident plane waves with fixed incidence direction  $d = (1, 0)$  and wavenumbers  $k_a$  and  $k_b$  on the object  $D$ . We measure the far field pattern  $u_\infty^{k_a}$  and  $u_\infty^{k_b}$  at points  $\hat{x}_l$ , for  $l = 1, \dots, N_{ff}$ . We choose a positive real constant  $\epsilon_{\hat{x}}$  and use the data generating procedure from Section 5.3.1 to generate the far field data  $\bar{u}_\infty^{k_m}$  for the frequencies  $k_m$ , for  $m = 1, \dots, N_{inc}$  at the points  $\hat{x}_{\tilde{l}}$ , for  $\tilde{l} = 1, \dots, \tilde{N}_{ff}$ . We solve the problem for the generated data using the solution space  $\mathbb{X}_{N_r^{(1)}, c}$  and the initial guess parameterization  $x^{(0)}$ . For the given data, we solve the problem using the solution space  $\mathbb{X}_{N_r^{(2)}}$  and the initial guess as the solution found using the generated data. For Method B, we use as  $\lambda$  the  $L_2$ -norm of the residue at each step, while for Method C, we use as  $\lambda$  the  $L_2$ -norm of the residue multiplied by the constant  $2\epsilon_{\hat{x}}/\tilde{N}_{ff}$ .

We consider three scenarios with the configuration above:

- We take the object  $D$  to be the ellipse with parameterization  $x(t) = (3 \cos(t), 4 \sin(t))$  and the wavenumbers of the incident waves to be  $k_a = 50$  and  $k_b = 51$ . The far field is given at points  $\hat{x}_l = (2l - 1)\pi/N_{ff}$ , for  $l = 1, \dots, N_{ff}$ , and we have  $N_{ff} = 32$ . For the generated data, we choose  $\epsilon_{\hat{x}} = \pi/2$ . We generate data for the wavenumbers  $k_m = m$ , for  $m = 1, \dots, 49$ . The initial guess  $x^{(0)}$  is the circle centered at the origin with radius 1.3. With respect to the solution space, we choose  $N_r^{(1)} = 3$  and  $N_r^{(2)} = 5$ . We present the results in Figure 5.14. In Figure 5.14(a), we present the result obtained applying Method C to the generated data, the object  $D$ , and the initial guess used in

the RLA-C method, and in Figure 5.14(b), we present the result obtained using the RLA-C method, the object  $D$ , and the answer obtained using Method C.

- We take the object  $D$  to be the Egg and the wavenumbers of the incident waves to be  $k_a = 55$  and  $k_b = 56$ . The far field is given at points  $\hat{x}_l = (2l - 1)\pi/N_{ff}$ , for  $l = 1, \dots, N_{ff}$ , and we have  $N_{ff} = 32$ . For the generated data, we choose  $\epsilon_{\hat{x}} = \pi/2$ . We generate data for the wavenumbers  $k_m = m$ , for  $m = 1, \dots, 54$ . The initial guess  $x^{(0)}$  is the circle centered at the origin with radius . With respect to the solution space, we choose  $N_r^{(1)} = 3$  and  $N_r^{(2)} = 5$ . We present the results in Figure 5.15. In Figure 5.15(a), we present the result obtained applying Method C to the generated data, the object  $D$ , and the initial guess used in the RLA-C method, and in Figure 5.15(b), we present the result obtained using the RLA-C method, the object  $D$ , and the answer obtained using Method C.
- We take the object  $D$  to be the rotated Kite and the wavenumbers of the incident waves to be  $k_a = 45$  and  $k_b = 46$ . The far field is given at points  $\hat{x}_l = (2l - 1)\pi/N_{ff}$ , for  $l = 1, \dots, N_{ff}$ , and we have  $N_{ff} = 32$ . For the generated data, we choose  $\epsilon_{\hat{x}} = \pi/2$ . We generate far field data for the wavenumbers  $k_m = m$ , for  $m = 1, \dots, 44$ . The initial guess  $x^{(0)}$  is the circle centered at the origin with radius 0.2. With respect to the solution space, we choose  $N_r^{(1)} = 3$  and  $N_r^{(2)} = 5$ . We present the results in Figure 5.16. In Figure 5.16(a), we present the result obtained applying Method C to the generated data, the object  $D$ , and the initial guess used in the RLA-C method, and in Figure 5.16(b), we present the result obtained after using the RLA-C method, the object  $D$ , and the answer obtained using of Method C.

We see in all scenarios of Example 5.3.2 that using the RLA-C method, we are able to reconstruct the illuminated part of the object using an initial guess that is not close to the object that we want to reconstruct. If we had tried to solve the same problem using the RLA method with the far field pattern given for the frequencies  $k_a$  and  $k_b$  using the same initial guesses, the method would fail. We can consider our procedure a globalization technique.

We have tried to use Method B instead of Method C in the RLA-C method, to solve the inverse problem for the generated far field pattern data. Unfortunately, we have not yet been able to obtain convergence of this alternative method in a general framework.

### **Example 5.3.3** *Influence of the choice of $\epsilon_{\hat{x}}$*

We assume two incident plane waves with fixed incident direction  $d = (1, 0)$  and wavenumbers  $k_a = 40$  and  $k_b = 41$  on the Egg. We measure the far field pattern  $u_{\infty}^{k_a}$  and  $u_{\infty}^{k_b}$  at points  $\hat{x}_l$ , for  $l = 1, \dots, N_{ff}$ . We vary the parameter  $\epsilon_{\hat{x}}$  and use the data generating procedure from Section 5.3.1 to generate the far field data  $\bar{u}_{\infty}^{k_m}$  for the wavenumbers  $k_m$ , for  $m = 1, \dots, N_{inc}$  at the points  $\hat{x}_{\tilde{l}}$ , for  $\tilde{l} = 1, \dots, \tilde{N}_{ff}$ . We solve the problem for the generated data using the

solution space  $\mathbb{X}_{N_r^{(1)},c}$ , where the initial guess parameterization  $x^{(0)}$  is the circle of radius 1.2 centered at the origin. For the given data, we solve the problem using the solution space  $\mathbb{X}_{N_r^{(2)}}$  and the initial guess as the solution found using the generated data.

As  $\epsilon_{\hat{x}}$  increases, the quality of the reconstruction obtained improves when using Method C. Overall, the quality of the reconstruction in the illuminated part of the object obtained by the RLA-C method improves with the increase of  $\epsilon_{\hat{x}}$ .

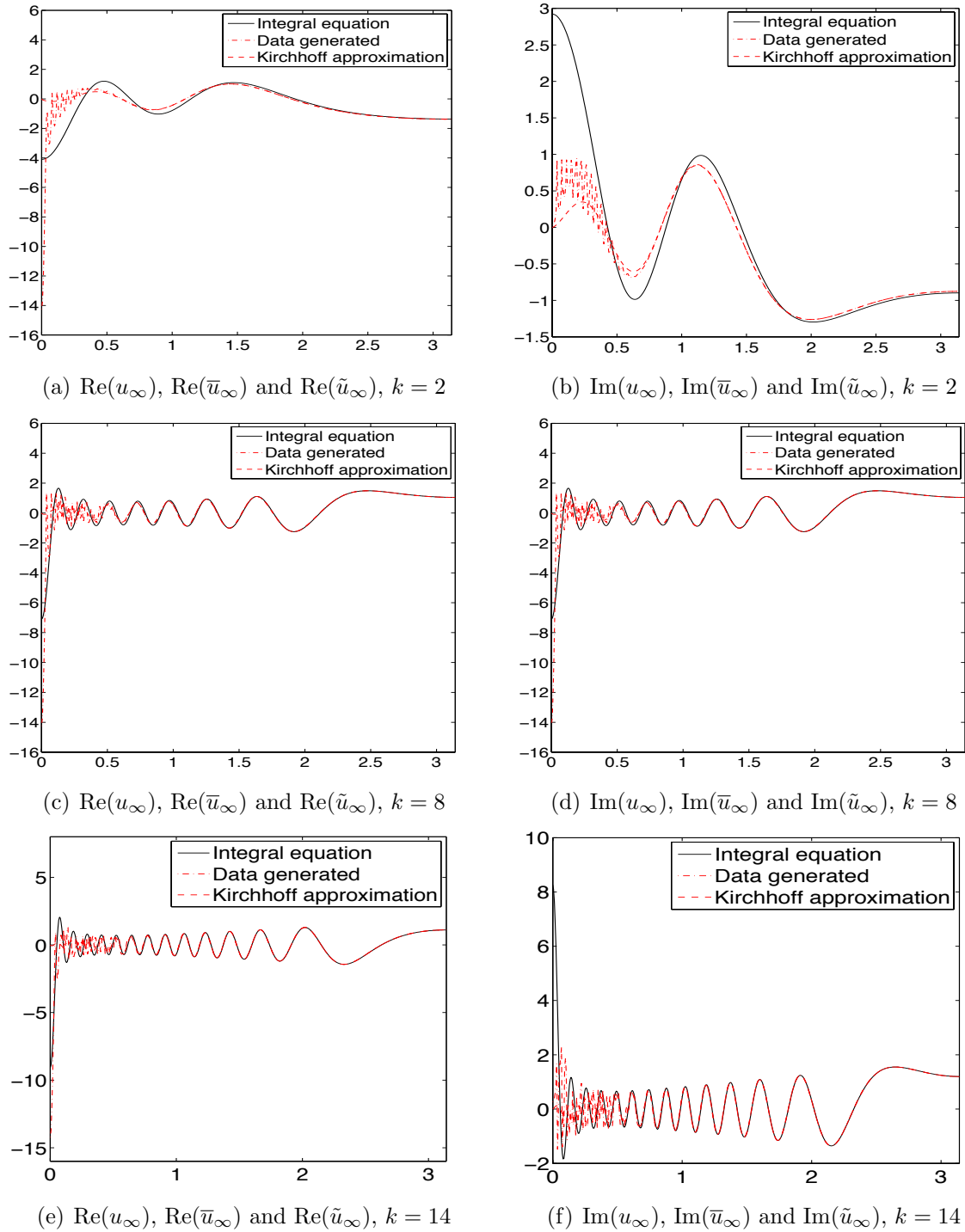
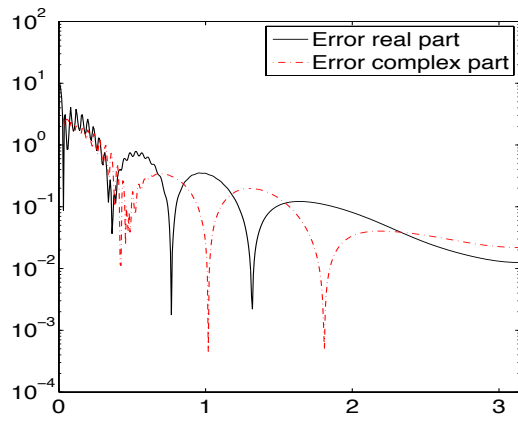
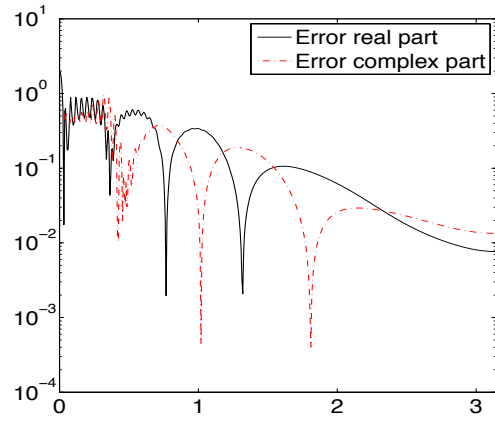


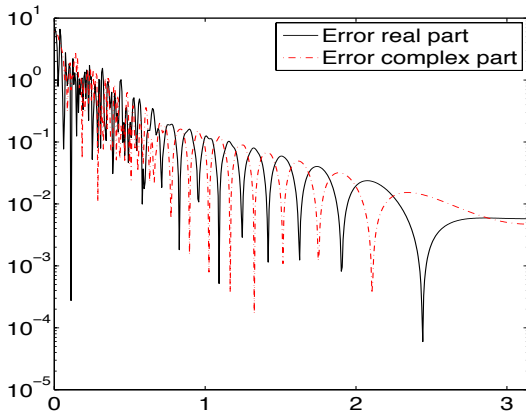
Figure 5.5: Comparison of the far field pattern obtained for the ellipse with  $k_a = 19$  and  $k_b = 20$  and  $d = (1, 0)$  by the Nyström method, labeled here as the Integral Equation, by the Kirchhoff approximation and by the our data generating procedure. In (a), (c) and (e) we have the real part of the far field patterns  $\text{Re}(u_\infty)$ ,  $\text{Re}(\bar{u}_\infty)$  and  $\text{Re}(\tilde{u}_\infty)$ , where black is used for the Nyström method,  $\text{Re}(u_\infty)$ , the red pattern ‘-.’ for the data generating procedure,  $\text{Re}(\bar{u}_\infty)$ , and the red pattern ‘-’ is used for the Kirchhoff approximation,  $\text{Re}(\tilde{u}_\infty)$ , respectively for  $k = 2$ ,  $k = 8$  and  $k = 14$ . In (b), (d) and (f) we have the real part of  $\text{Re}(u_\infty)$ ,  $\text{Re}(\bar{u}_\infty)$  and  $\text{Re}(\tilde{u}_\infty)$ , where black is used for the Nyström method,  $\text{Re}(u_\infty)$ , the red pattern ‘-.’ for the data generating procedure  $\text{Re}(\bar{u}_\infty)$ , and the red pattern ‘-’ is used for the Kirchhoff approximation,  $\text{Re}(\tilde{u}_\infty)$ , respectively for  $k = 2$ ,  $k = 8$  and  $k = 14$ .



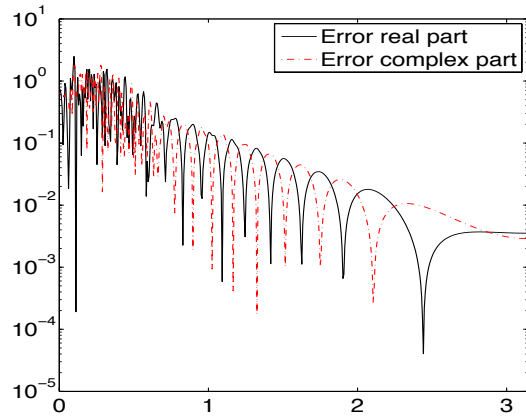
(a) Absolute errors for  $k = 2$



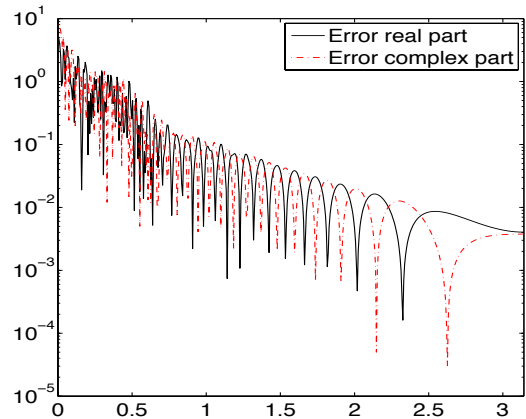
(b) Relative errors for  $k = 2$



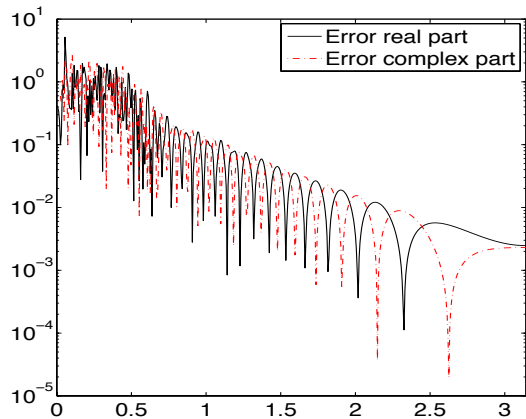
(c) Absolute errors for  $k = 8$



(d) Relative errors for  $k = 8$

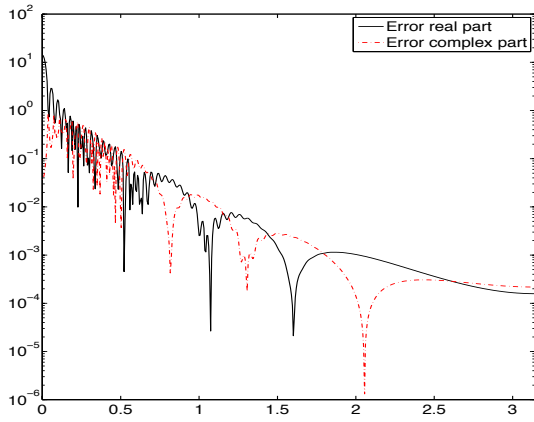


(e) Absolute errors for  $k = 14$

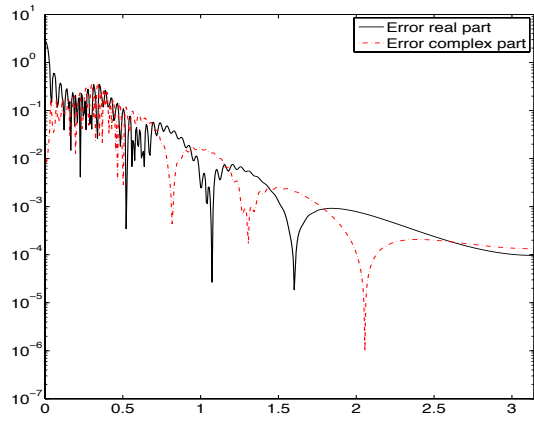


(f) Relative errors for  $k = 14$

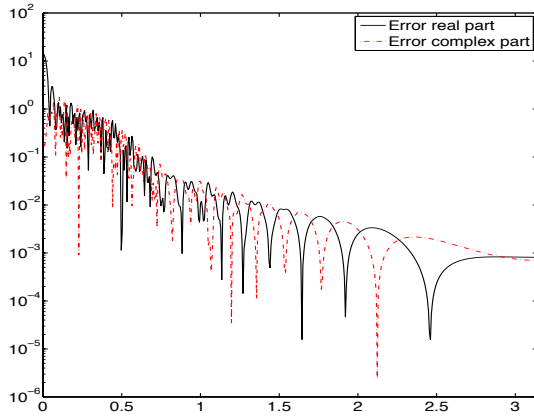
Figure 5.6: Absolute and relative error with respect to the far field obtained with the Nyström method of the data generating procedure for the ellipse using  $k_a = 19$  and  $k_b = 20$ . We have the absolute error for the real part in black and the imaginary part in the red pattern ‘-.’ respectively for the frequencies: (a)  $k = 2$ , (c)  $k = 8$  and (e)  $k = 14$ . In the other figures, the relative error for the real part is in black and for the imaginary part in the red pattern ‘-.’, respectively for the frequencies: (b)  $k = 2$ , (d)  $k = 8$  and (f)  $k = 14$ . Note that we have a log scale on the  $y$ -axis of those graphs.



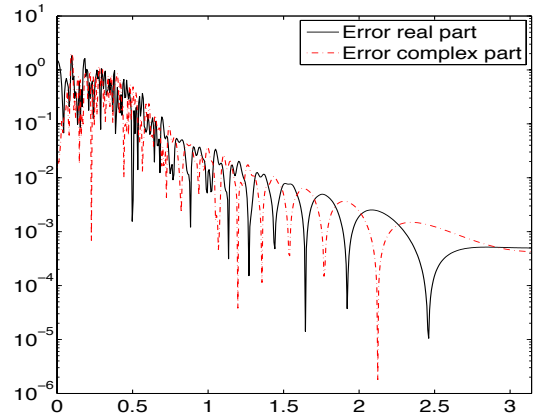
(a) Absolute errors for  $k = 2$



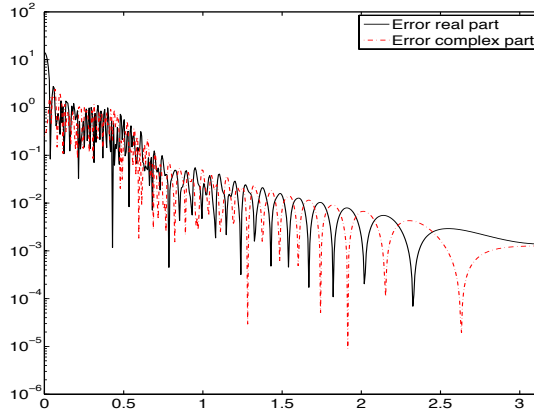
(b) Relative errors for  $k = 2$



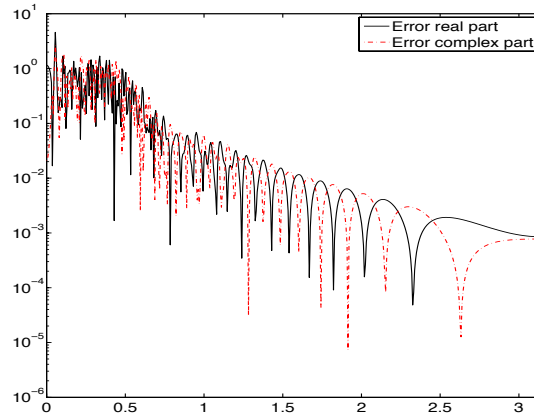
(c) Absolute errors for  $k = 8$



(d) Relative errors for  $k = 8$



(e) Absolute errors for  $k = 14$



(f) Relative errors for  $k = 14$

Figure 5.7: Absolute and relative error with respect to the Kirchhoff approximation of the data generating procedure for the ellipse using  $k_a = 19$  and  $k_b = 20$ . We have the absolute error for the real part in black and the imaginary part in the red pattern ‘-.’ respectively for the frequencies: (a)  $k = 2$ , (c)  $k = 8$  and (e)  $k = 14$ . In the other figures, the relative error for the real part is in black and for the imaginary part in the red pattern ‘-.’, respectively for the frequencies: (b)  $k = 2$ , (d)  $k = 8$  and (f)  $k = 14$ . Note that we have a log scale on the  $y$ -axis of those graphs.

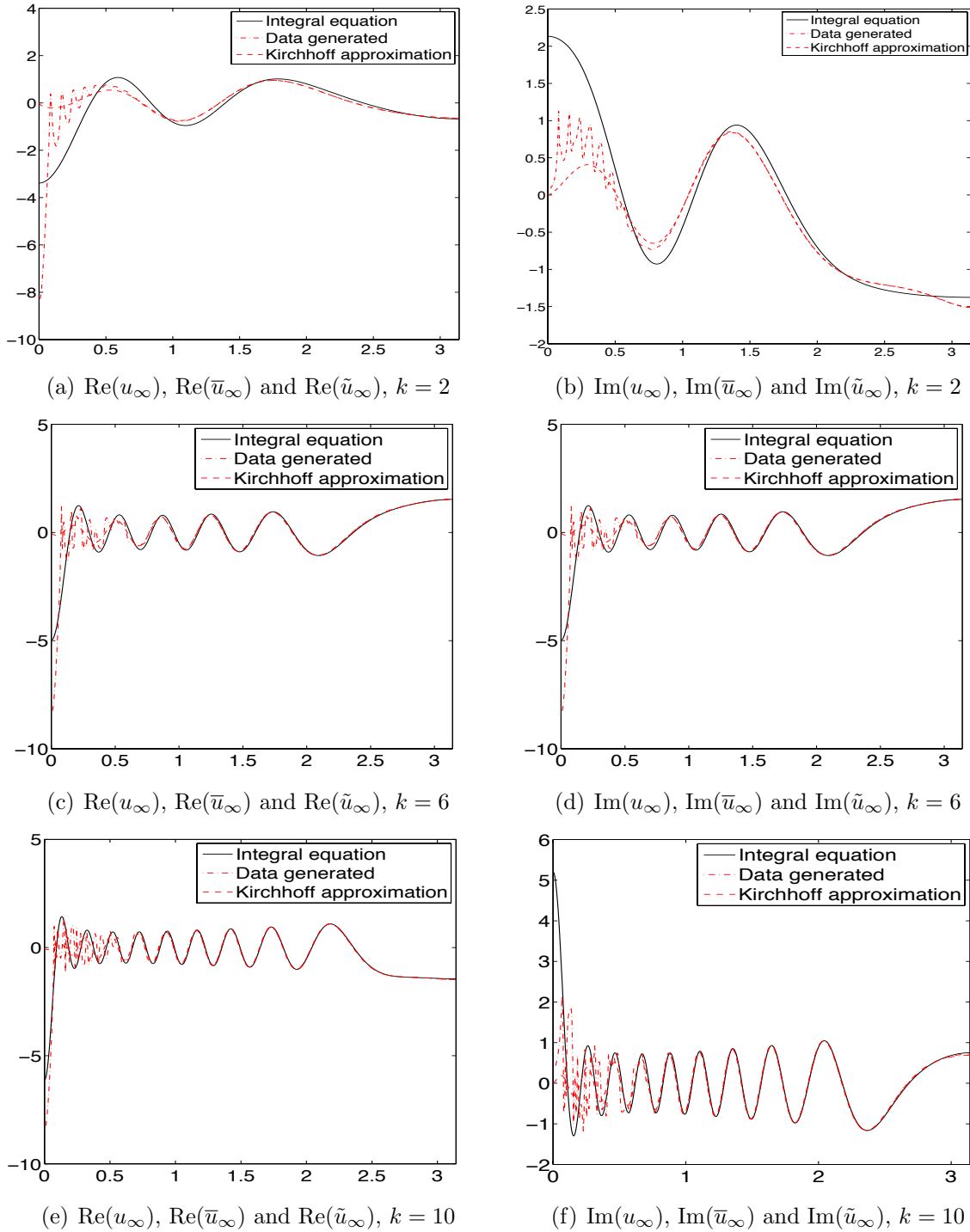
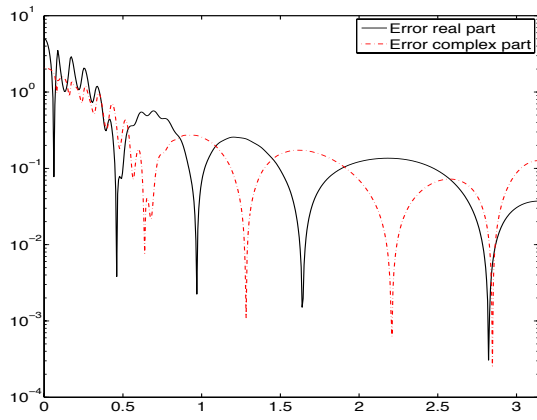
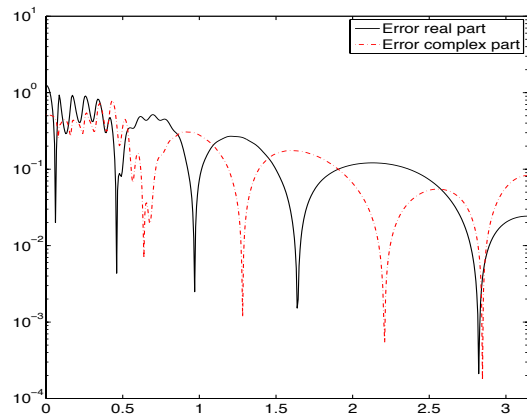


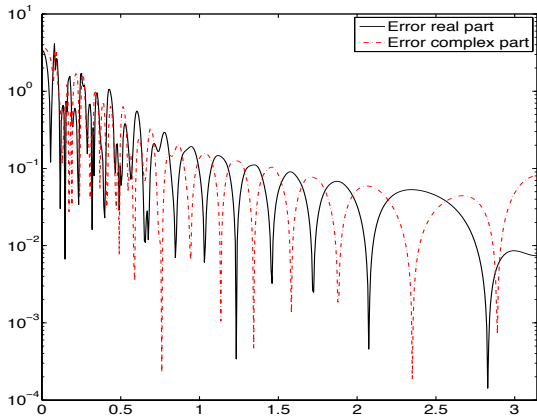
Figure 5.8: Comparison of the far field pattern obtained for the Egg with  $k_a = 11$  and  $k_b = 12$  and  $d = (1,0)$  by the Nyström method, labeled here as the Integral Equation, by the Kirchhoff approximation and by the our data generating procedure. In (a), (c) and (e) we have the real part of the far field patterns  $\text{Re}(u_\infty)$ ,  $\text{Re}(\bar{u}_\infty)$  and  $\text{Re}(\tilde{u}_\infty)$ , where black is used for the Nyström method,  $\text{Re}(u_\infty)$ , the red pattern ‘-.’ for the data generating procedure,  $\text{Re}(\bar{u}_\infty)$ , and the red pattern ‘-’ is used for the Kirchhoff approximation,  $\text{Re}(\tilde{u}_\infty)$ , respectively for  $k = 2$ ,  $k = 6$  and  $k = 10$ . In (b), (d) and (f) we have the real part of  $\text{Re}(u_\infty)$ ,  $\text{Re}(\bar{u}_\infty)$  and  $\text{Re}(\tilde{u}_\infty)$ , where black is used for the Nyström method,  $\text{Re}(u_\infty)$ , the red pattern ‘-.’ for the data generating procedure  $\text{Re}(\bar{u}_\infty)$ , and the red pattern ‘-’ is used for the Kirchhoff approximation,  $\text{Re}(\tilde{u}_\infty)$ , respectively for  $k = 2$ ,  $k = 6$  and  $k = 10$ .



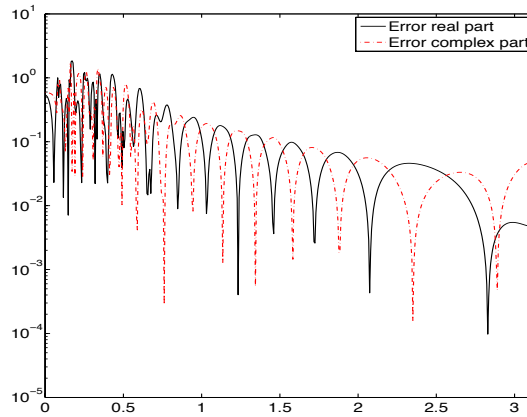
(a) Absolute errors for  $k = 2$



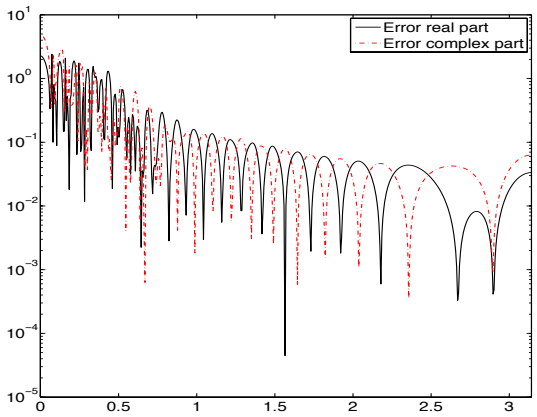
(b) Relative errors for  $k = 2$



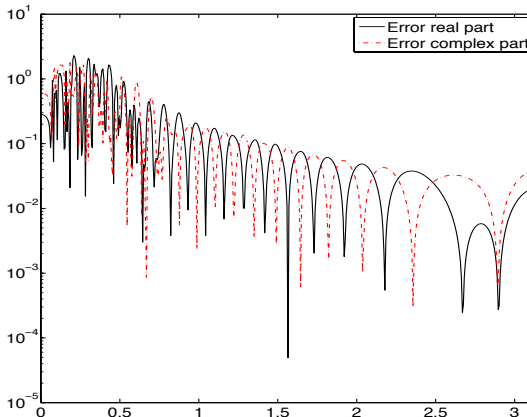
(c) Absolute errors for  $k = 6$



(d) Relative errors for  $k = 6$

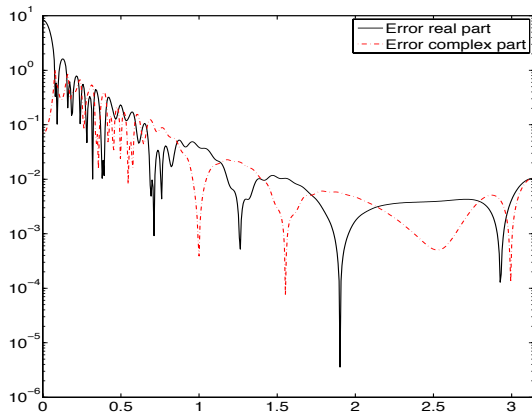


(e) Absolute errors for  $k = 10$

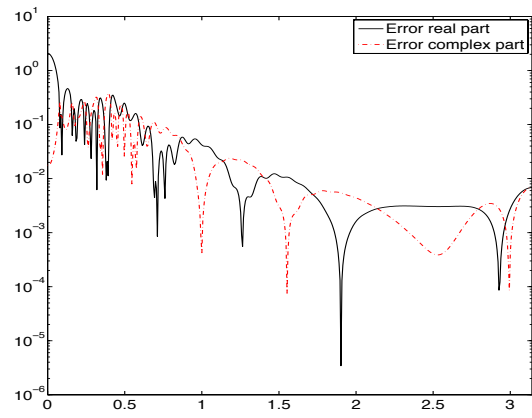


(f) Relative errors for  $k = 10$

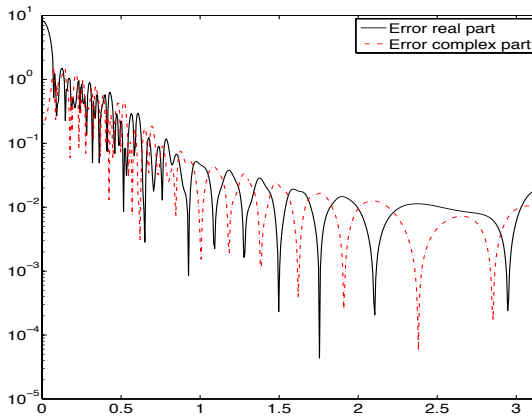
Figure 5.9: Absolute and relative error with respect to the far field obtained with the Nyström method of the data generating procedure for the Egg using  $k_a = 11$  and  $k_b = 12$ . We have the absolute error for the real part in black and the imaginary part in the red pattern ‘-.’ respectively for the frequencies: (a)  $k = 2$ , (c)  $k = 6$  and (e)  $k = 10$ . In the other figures, the relative error for the real part is in black and for the imaginary part in the red pattern ‘-.’, respectively for the frequencies: (b)  $k = 2$ , (d)  $k = 6$  and (f)  $k = 10$ . Note that we have a log scale on the  $y$ -axis of those graphs.



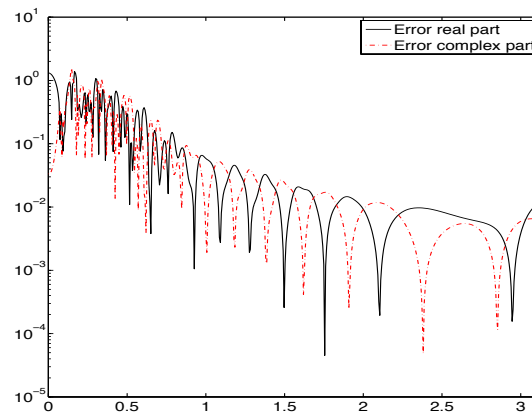
(a) Absolute errors for  $k = 2$



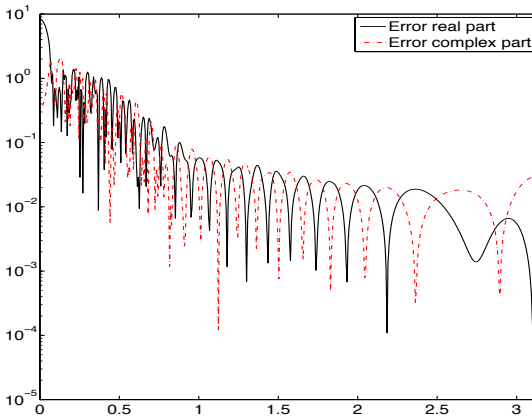
(b) Relative errors for  $k = 2$



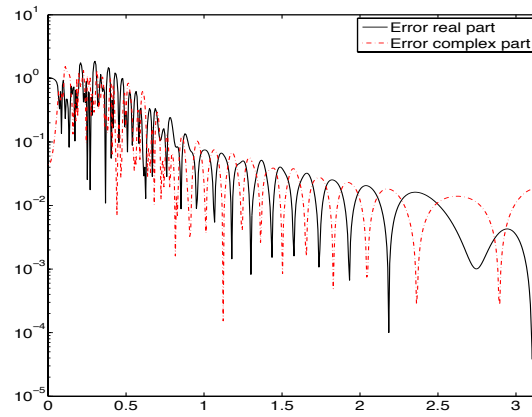
(c) Absolute errors for  $k = 6$



(d) Relative errors for  $k = 6$



(e) Absolute errors for  $k = 10$



(f) Relative errors for  $k = 10$

Figure 5.10: Absolute and relative error with respect to the Kirchhoff approximation of the data generating procedure for the Egg using  $k_a = 11$  and  $k_b = 12$ . We have the absolute error for the real part in black and the imaginary part in the red pattern ‘-.’ respectively for the frequencies: (a)  $k = 2$ , (c)  $k = 6$  and (e)  $k = 10$ . In the other figures, the relative error for the real part is in black and for the imaginary part in the red pattern ‘-.’, respectively for the frequencies: (b)  $k = 2$ , (d)  $k = 6$  and (f)  $k = 10$ . Note that we have a log scale on the  $y$ -axis of those graphs.

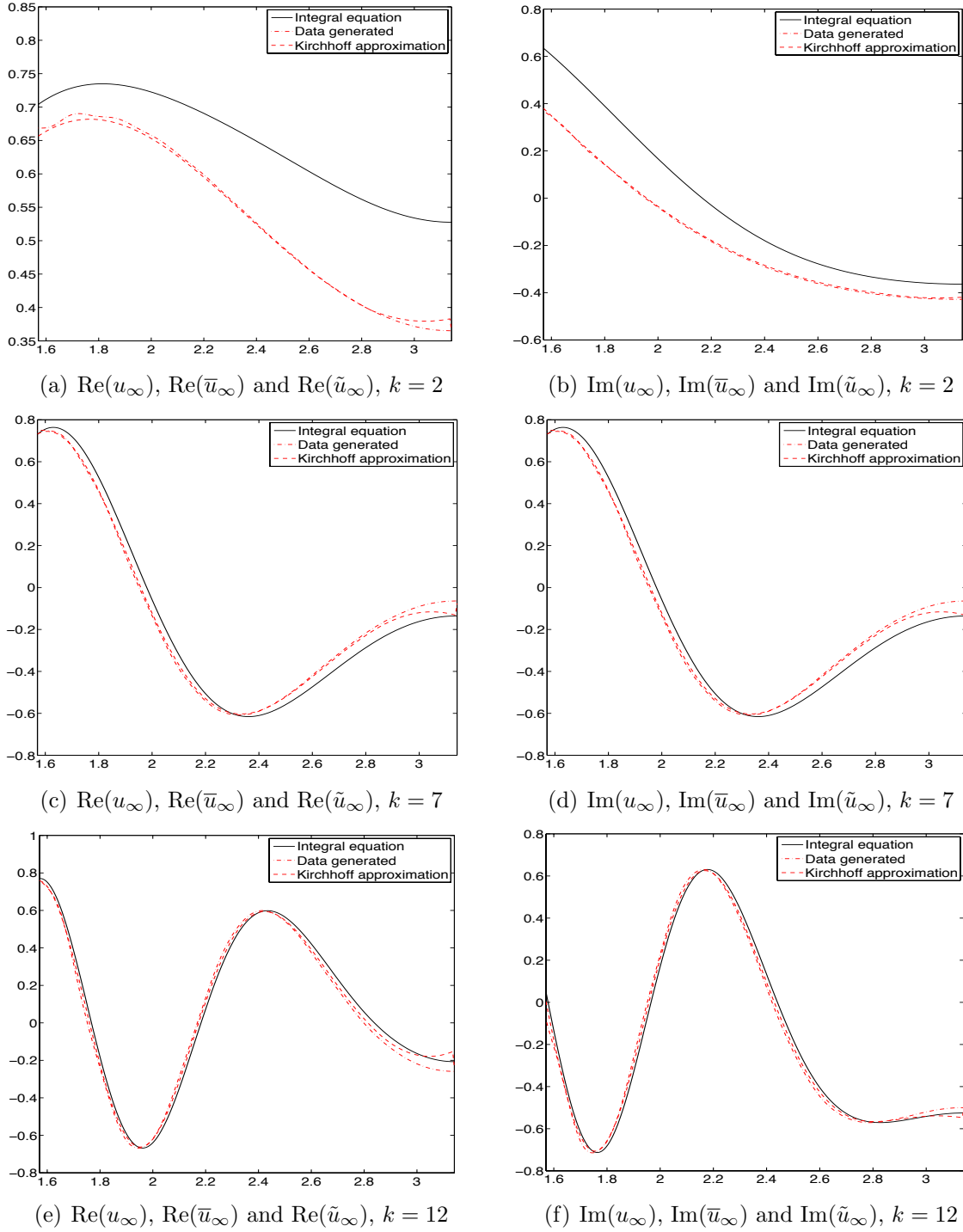


Figure 5.11: Comparison of the far field pattern obtained for the Kite rotated in 180 degrees with  $k_a = 14$  and  $k_b = 15$  and  $d = (1, 0)$  by the Nyström method, labeled here as the Integral Equation, by the Kirchhoff approximation and by the our data generating procedure. In (a), (c) and (e) we have the real part of the far field patterns  $\text{Re}(u_\infty)$ ,  $\text{Re}(\bar{u}_\infty)$  and  $\text{Re}(\tilde{u}_\infty)$ , where black is used for the Nyström method,  $\text{Re}(u_\infty)$ , the red pattern ‘-.’ for the data generating procedure,  $\text{Re}(\bar{u}_\infty)$ , and the red pattern ‘-’ is used for the Kirchhoff approximation,  $\text{Re}(\tilde{u}_\infty)$ , respectively for  $k = 2$ ,  $k = 7$  and  $k = 12$ . In (b), (d) and (f) we have the real part of  $\text{Re}(u_\infty)$ ,  $\text{Re}(\bar{u}_\infty)$  and  $\text{Re}(\tilde{u}_\infty)$ , where black is used for the Nyström method,  $\text{Re}(u_\infty)$ , the red pattern ‘-.’ for the data generating procedure  $\text{Re}(\bar{u}_\infty)$ , and the red pattern ‘-’ is used for the Kirchhoff approximation,  $\text{Re}(\tilde{u}_\infty)$ , respectively for  $k = 2$ ,  $k = 7$  and  $k = 12$ . 113

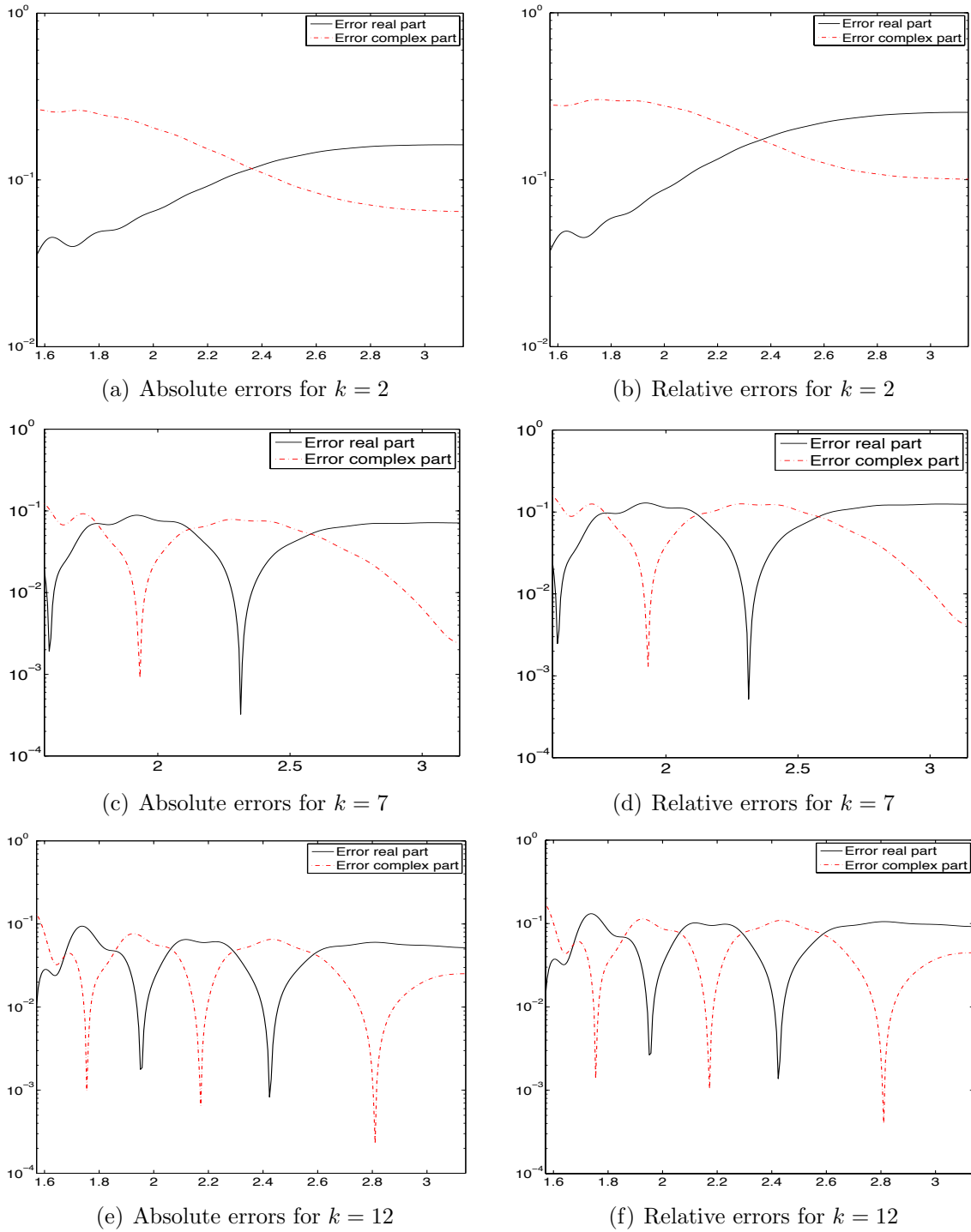
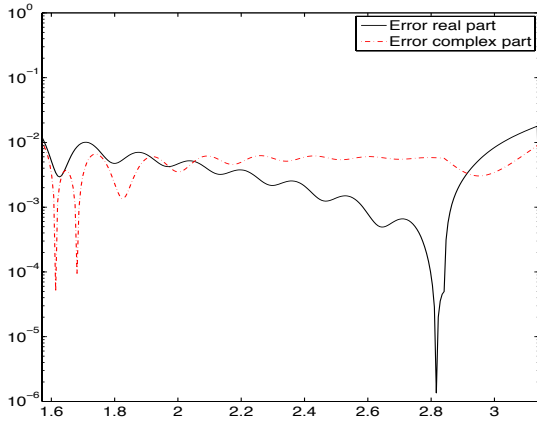
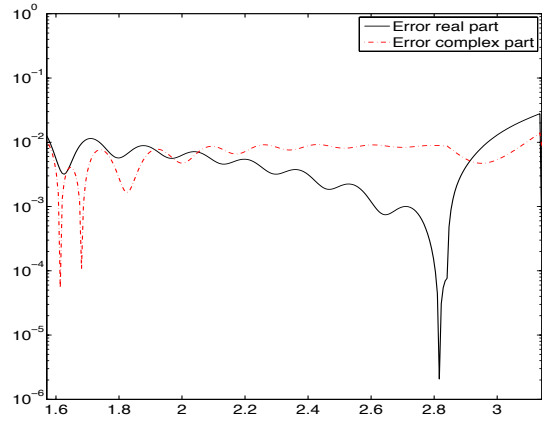


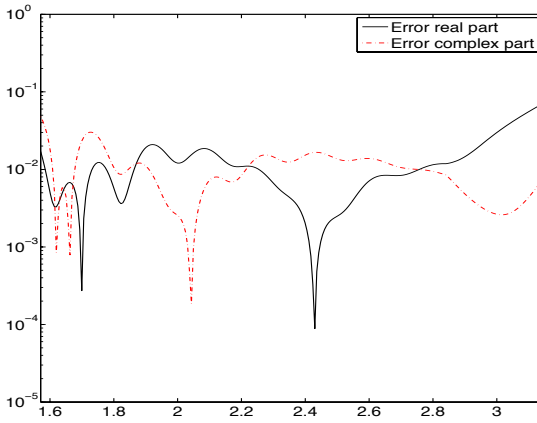
Figure 5.12: Absolute and relative error with respect to the far field obtained with the Nyström method of the data generating procedure for the rotated Kite using  $k_a = 14$  and  $k_b = 15$ . We have the absolute error for the real part in black and the imaginary part in the red pattern ‘-.’ respectively for the frequencies: (a)  $k = 2$ , (c)  $k = 7$  and (e)  $k = 12$ . In the other figures, the relative error for the real part is in black and for the imaginary part in the red pattern ‘-.’, respectively for the frequencies: (b)  $k = 2$ , (d)  $k = 7$  and (f)  $k = 12$ . Note that we have a log scale on the  $y$ -axis of those graphs. The domain of these figures go from  $\pi/2$  to  $\pi$  since it is not possible to take the Kirchhoff approximation from 0 to  $\pi$  because the object is not convex for those values.



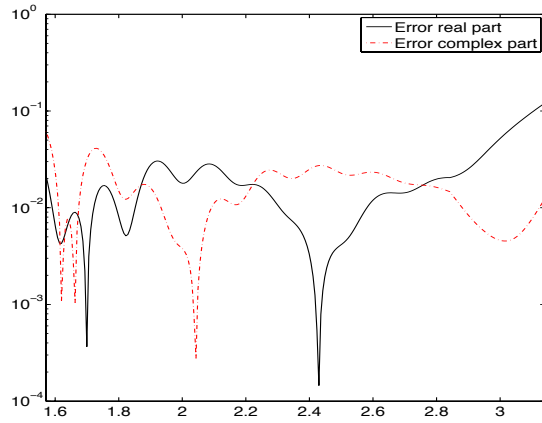
(a) Absolute errors for  $k = 2$



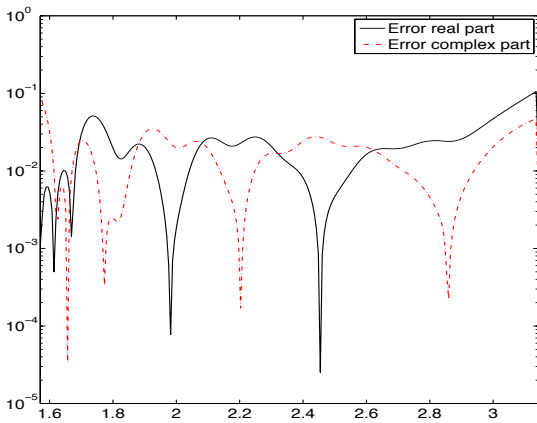
(b) Relative errors for  $k = 2$



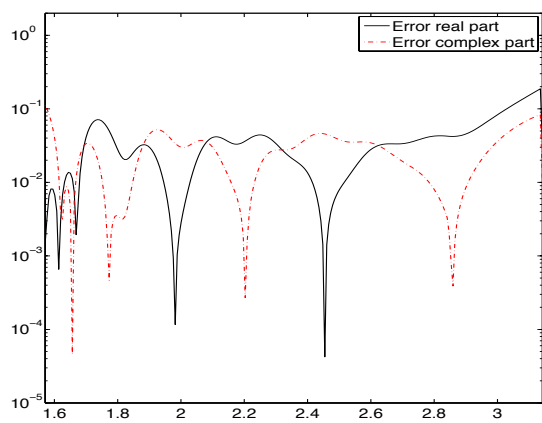
(c) Absolute errors for  $k = 7$



(d) Relative errors for  $k = 7$



(e) Absolute errors for  $k = 12$



(f) Relative errors for  $k = 12$

Figure 5.13: Absolute and relative error with respect to the Kirchhoff approximation of the data generating procedure for the rotated Kite using  $k_a = 14$  and  $k_b = 15$ . We have the absolute error for the real part in black and the imaginary part in the red pattern ‘-.’ respectively for the frequencies: (a)  $k = 2$ , (c)  $k = 7$  and (e)  $k = 12$ . In the other figures, the relative error for the real part is in black and for the imaginary part in the red pattern ‘-.’, respectively for the frequencies: (b)  $k = 2$ , (d)  $k = 7$  and (f)  $k = 12$ . Note that we have a log scale on the  $y$ -axis of those graphs. The domain of these figures go from  $\pi/2$  to  $\pi$  since it is not possible to take the Kirchhoff approximation from 0 to  $\pi$  because the object is not convex for those values.

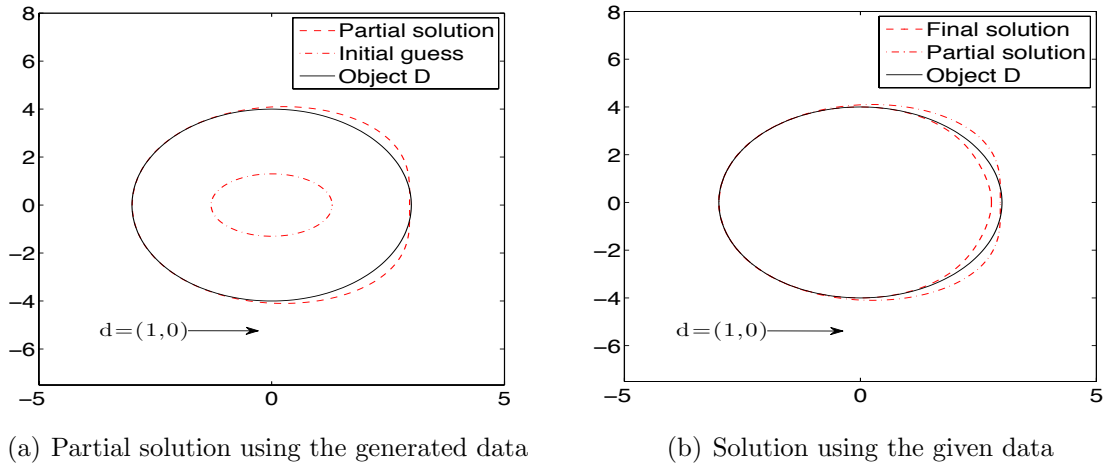


Figure 5.14: We use the RLA-C method to solve the inverse problem for the ellipse with parameterization  $x(t) = (3 \cos(t), 4 \sin(t))$ . We have the far field pattern at the points  $\hat{x}_l = (2l - 1)\pi/N_{ff}$ , for  $l = 1, \dots, N_{ff}$ , with  $N_{ff} = 32$ , generated by the scattering of two incident plane waves with incidence direction  $d = (1, 0)$  and wavenumbers  $k_a = 50$  and  $k_b = 51$ . We generate far field data for wavenumbers  $k_m = m$ , for  $m = 1, \dots, 49$ . We use the parameter  $\epsilon_{\hat{x}} = \pi/2$  to decide the generated far field pattern that we use for Method C. The initial guess  $x^{(0)}$  for the RLA-C method is the circle with center at the origin and radius 1.3. In (a) we present the result obtained applying Method C to the generated data, the object  $D$ , and the initial guess used in the RLA-C method, and in (b) we present the result obtained using the RLA-C method, the object  $D$ , and the answer obtained using Method C.

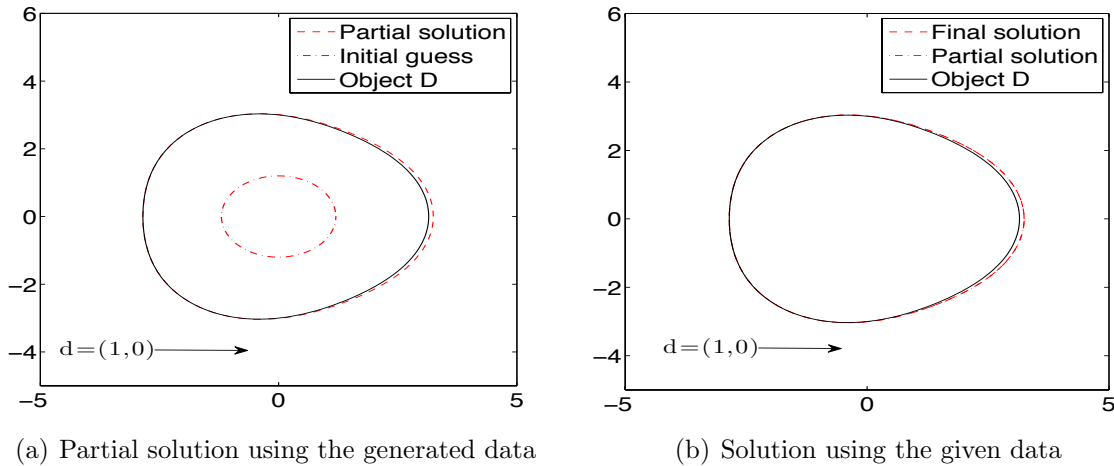
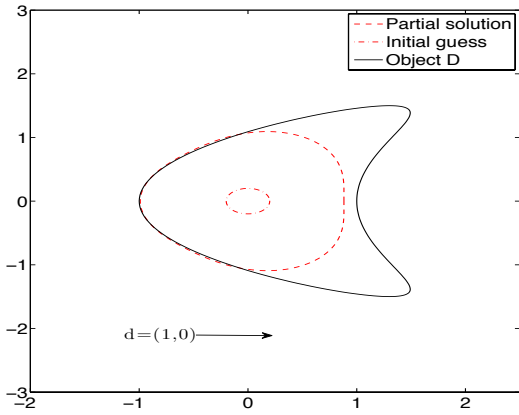
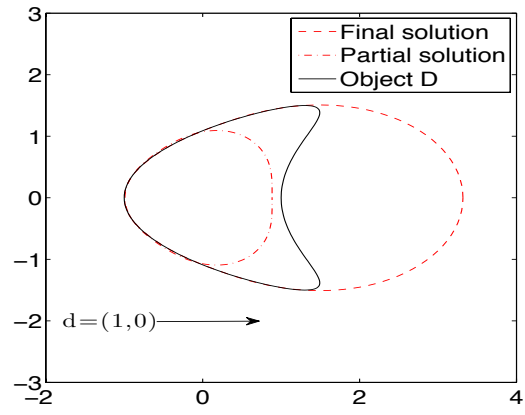


Figure 5.15: We use the RLA-C method to solve the inverse problem for the Egg. We have the far field pattern at the points  $\hat{x}_l = (2l - 1)\pi/N_{ff}$ , for  $l = 1, \dots, N_{ff}$ , with  $N_{ff} = 32$ , generated by the scattering of two incident plane waves with incidence direction  $d = (1, 0)$  and wavenumbers  $k_a = 55$  and  $k_b = 56$ . We generate far field data for wavenumbers  $k_m = m$ , for  $m = 1, \dots, 54$ . We use the parameter  $\epsilon_{\hat{x}} = \pi/2$  to decide the generated far field pattern that we use for Method C. The initial guess  $x^{(0)}$  for the RLA-C method is the circle with center at the origin and radius 1.2. In (a) we present the result obtained applying Method C to the generated data, the object  $D$ , and the initial guess used in the RLA-C method, and in (b) we present the result obtained using the RLA-C method, the object  $D$ , and the answer obtained using Method C.



(a) Partial solution using the generated data



(b) Solution using the given data

Figure 5.16: We use RLA-C method to solve the inverse problem for the rotated Kite. We have the far field pattern at the points  $\hat{x}_l = (2l-1)\pi/N_{ff}$ , for  $l = 1, \dots, N_{ff}$ , with  $N_{ff} = 32$ , generated by the scattering of two incident plane waves with incidence direction  $d = (1, 0)$  and wavenumbers  $k_a = 45$  and  $k_b = 46$ . We generate far field data for wavenumbers  $k_m = m$ , for  $m = 1, \dots, 44$ . We use the parameter  $\epsilon_{\hat{x}} = \pi/2$  to decide the generated far field pattern that we use for Method C. The initial guess  $x^{(0)}$  for the RLA-C method is the circle with center at the origin and radius 0.2. In (a) we present the result obtained applying Method C to the generated data, the object  $D$ , and the initial guess used in the RLA-C method, and in (b) we present the result obtained using the RLA-C method, the object  $D$ , and the answer obtained using Method C.

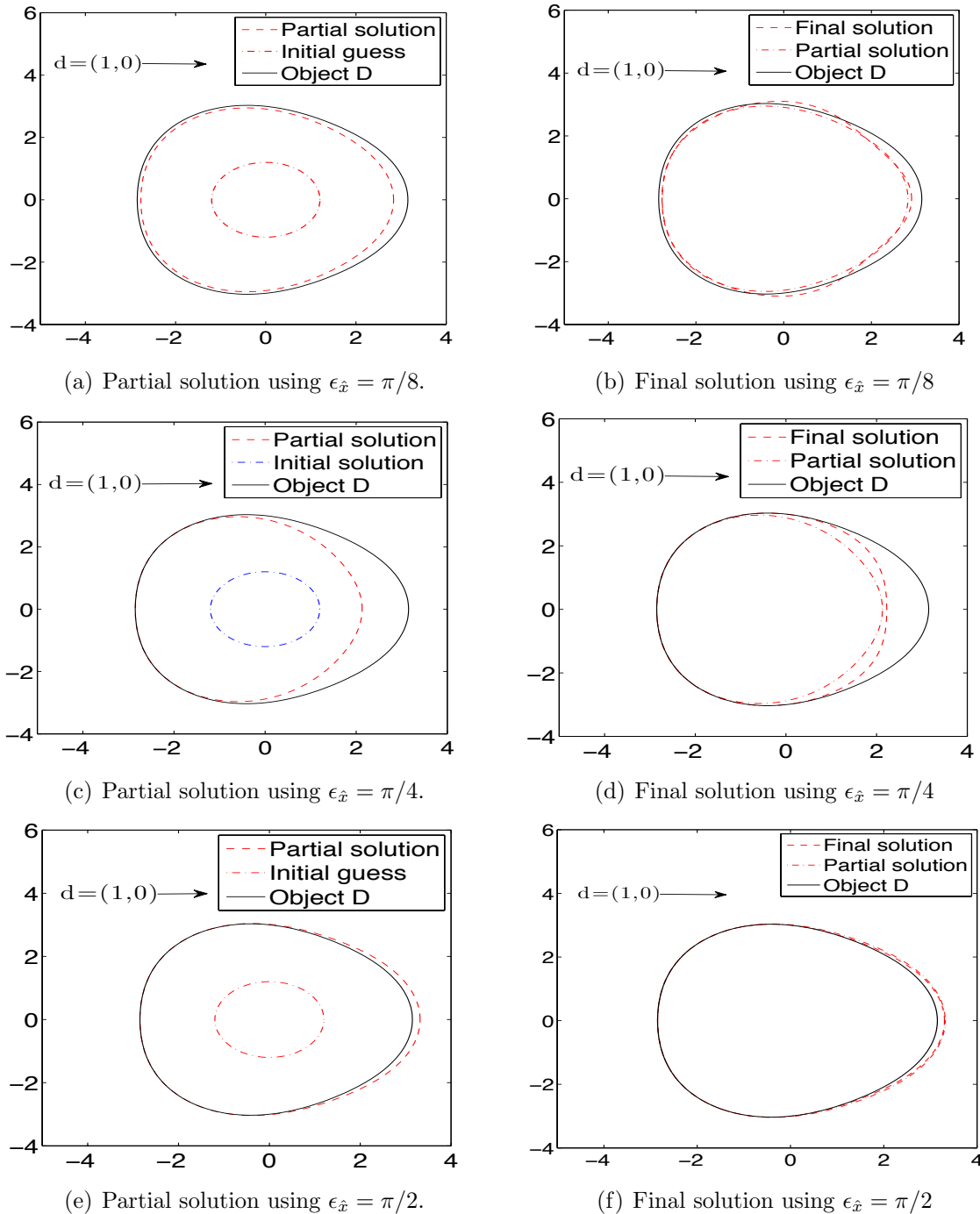


Figure 5.17: We use the RLA-C method to solve the inverse problem for the Egg. We have the far field pattern at the points  $\hat{x}_l = (2l - 1)\pi/N_{ff}$ , for  $l = 1, \dots, N_{ff}$ , with  $N_{ff} = 32$ , generated by the scattering of two incident plane waves with incidence direction  $d = (1, 0)$  and wavenumbers  $k_a = 40$  and  $k_b = 41$ . We generate far field data for wavenumbers  $k_m = m$ , for  $m = 1, \dots, 44$ . We vary the parameter  $\epsilon_{\hat{x}}$  that we use to decide the generated far field pattern that we use for Method C. The initial guess  $x^{(0)}$  for the RLA-C method is the circle with center at the origin and radius 1.2. We have the result obtained applying Method C in the generated data, the object  $D$ , and the initial guess used in the RLA-C method for (a)  $\epsilon_{\hat{x}} = \pi/2$ , (c)  $\epsilon_{\hat{x}} = \pi/4$ , and (e)  $\epsilon_{\hat{x}} = \pi/8$ , and we have the result obtained after using the RLA-C method, the object  $D$ , and the answer obtained using Method C for (b)  $\epsilon_{\hat{x}} = \pi/2$ , (d)  $\epsilon_{\hat{x}} = \pi/4$ , and (f)  $\epsilon_{\hat{x}} = \pi/8$ .

# Chapter 6

## Conclusion

In this thesis, we first presented Method B for the solution of the inverse sound-soft acoustic scattering problem, which is a variation of Johansson and Sleeman’s method (Method A) proposed in [16], that shows to be less computationally expensive than Method A. Method B is based on a two-step procedure like Method A, however, it repeats the second step of the two-step procedure until stopping criteria are reached. The advantage of Method B is that it solves the system in the first step fewer times than it solves the system in the second step, and size of the system in the first step is proportional to the frequency of the incident plane wave, which makes it much larger than the size of the system in the second step, which is proportional to the number of degrees of freedom of the solution to describe the object  $D$  that we seek to reconstruct. In all the examples, we reconstructed star-shaped objects of the form  $x(t) = x_r(t)(\cos(t), \sin(t))$ , and found the function  $x_r(t)$  in two types of solution space: trigonometric polynomials, seen in the work of [3] and many others; and B-splines. Apparently the solutions obtained in the two spaces are very similar, however finding the solution in the trigonometric space seems to be much less computationally expensive than in the space of B-splines. The advantage of the space of B-splines would be the fact that it would not need as many degrees of freedom as the trigonometric polynomials and it would be compatible with CAD tools.

Next, with the objective of obtaining detailed reconstructions of objects, we presented the RLA algorithm proposed in [21] for inhomogeneous media and later shown for Dirichlet problems in [23]. This is a multi-frequency algorithm that, starting from a simple initial guess, solves the inverse problem for each frequency. Instead of using Newton’s method recursively at each frequency, we use Method B. We were able to obtain detailed approximations of the illuminated part of the object using this algorithm, but the quality of the reconstruction of the shadowed part of the object was not satisfactory. To address this problem, using ideas in a work in progress of Sini and Nguyen, we inserted objects in our configuration that are able to reflect the incident plane wave back to the shadowed part of the unknown object. Applying this procedure, we were able to recover the shadowed part of the object.

Subsequently, we studied the problem for convex objects at frequencies out of the resonance region. We started by presenting the Kirchhoff approximation to calculate the far field pattern of the convex object (see [31]). Next, we presented the two-step Method C for solving

the inverse problem to reconstruct the convex object. We showed that this method works for the case of approximating a circle, and that the region of convergence of the method is inversely proportional to the frequency. The biggest problem of the method presented is that we require that the approximation in each step be a convex object. We had problems devising an algorithm to obtain a convex approximation of the object, and we proposed an heuristic that works most of the time, but may not be the best solution.

Next, we developed a globalization technique to obtain better initial guesses for convex obstacles for solving the inverse scattering problem at frequencies out of the resonance region. For use in this globalization technique, we presented a procedure based on the Kirchhoff approximation to generate synthetic data given a pair of measures of the far field pattern of a convex obstacle. The quality of the results obtained depends on the frequency at which we are approximating the far field pattern, and on the position  $\hat{x}$ . The results are better for higher frequencies and close to the point where  $d \cdot \hat{x}$  is minimal.

Finally, we considered the problem of reconstructing a convex object given two frequencies that are not in the resonance region of the object, which means that the wavelengths are bigger than the size of the scatterer. We know that for these frequencies, if we apply any of the single frequency methods presented in Chapter 2, we need an initial guess very close to the solution. We do not have such a close initial guess, so to address this problem, we generated data using our procedure for low frequencies. We used a multi-frequency method based on the RLA. We presented a method that uses the generated data together with Method C to obtain an approximation of the object. This approximation can be used as an initial guess for Method B with the given data, and we call this the RLA-C method. We obtain good reconstructions of the illuminated part of the object with an initial guess that is not very close to the object.

For future work, there are several other directions to pursue. We intend to obtain some convergence results for Method B. There is also the opportunity to try to adapt the ideas of [23] and [22] to try to obtain convergence results for Method B used in the RLA method. We also want to obtain more general results related to the convergence of Method C, not only for the circle, and to use these results together with the multi-frequency ideas to obtain convergence results.

Another path to pursue is the construction of a better algorithm for reconstructing convex objects. We believe that the use of B-splines is the key to obtaining the desired convexity. We might need to understand more properties of B-splines to try to obtain an algorithm for reconstructing a convex object.

Another subject that would be interesting is to use the ideas of [26] and [27] to obtain faster solvers for direct problems at frequencies out of the resonance region. We have already started our work in this area, and have seen that this approach is very effective for very high frequencies. We can still use the RLA-C method and apply those ideas for the last two frequencies to solve the inverse problem with the given data.

With respect to the RLA-C method, it would be interesting to devise a method for objects that have curvature close to zero, positive or even negative, with the idea that these objects do not reflect the wave onto themselves too much. We can try to adapt the RLA-C method for those situations, which would allow us to solve a problem like the pear.

We can adapt all the methods presented here for the sound-hard obstacle (Neumann boundary condition) and for the impedance case (Robin boundary condition). The scattering of time-harmonic electromagnetic waves from infinitely long cylinders with polarization parallel to the cylinder axis also reduces to the two-dimensional Helmholtz equation. Therefore, all the methods presented in this thesis can be adapted for use in inverse electromagnetic scattering problems.

Finally, it is our belief that we can use the algorithms developed in this thesis to test the use of different coatings around objects to achieve an effect of invisibility, or of substantial change of the reconstructed object.

# Bibliography

- [1] R. Kress, “Uniqueness and numerical methods in inverse obstacle scattering,” *Journal of Physics: Conference Series*, vol. 73, no. 1, p. 012003, 2007.
- [2] T. Hohage, “Logarithmic convergence rates of the iteratively regularized Gauss - Newton method for an inverse potential and an inverse scattering problem,” *Inverse Problems*, vol. 13, no. 5, p. 1279, 1997.
- [3] D. Colton and R. Kress, *Inverse Acoustic and Electromagnetic Scattering Theory*. Springer, second ed., 1998.
- [4] R. Kress, “Newton’s method for inverse obstacle scattering meets the method of least squares,” *Inverse Problems*, vol. 19, no. 6, p. S91, 2003.
- [5] A. Kirsch and R. Kress, “An optimization method in inverse acoustic scattering,” *Boudary Elements IX*, vol. 3, pp. 3–18, 1987.
- [6] R. Potthast, “A fast new method to solve inverse scattering problems,” *Inverse Problems*, vol. 12, no. 5, p. 731, 1996.
- [7] R. Potthast, “A point source method for inverse acoustic and electromagnetic obstacle scattering problems,” *IMA Journal of Applied Mathematics*, vol. 61, no. 2, pp. 119–140, 1998.
- [8] R. Potthast, *Point Sources and Multipoles in Inverse Scattering Theory*. Chapman & Hall/CRC Research Notes in Mathematics, Taylor & Francis Group, 2001.
- [9] D. Colton and A. Kirsch, “A simple method for solving inverse scattering problems in the resonance region,” *Inverse Problems*, vol. 12, no. 4, p. 383, 1996.
- [10] R. Potthast, “Stability estimates and reconstructions in inverse acoustic scattering using singular sources,” *Journal of Computational and Applied Mathematics*, vol. 114, no. 2, pp. 247 – 274, 2000.
- [11] A. Kirsch, “Characterization of the shape of a scattering obstacle using the spectral data of the far field operator,” *Inverse Problems*, vol. 14, no. 6, p. 1489, 1998.
- [12] M. Ikehata, “Reconstruction of an obstacle from the scattering amplitude at a fixed frequency,” *Inverse Problems*, vol. 14, no. 4, p. 949, 1998.

- [13] P. Serranho, *A hybrid method for inverse obstacle scattering problems*. Ph.D. dissertation, University of Göttingen, 2007.
- [14] R. Kress and W. Rundell, “Nonlinear integral equations and the iterative solution for an inverse boundary value problem,” *Inverse Problems*, vol. 21, no. 4, p. 1207, 2005.
- [15] O. Ivanyshyn, *Nonlinear Boundary Integral Equations in Inverse Scattering*. Ph.D. dissertation, University of Göttingen, 2007.
- [16] T. Johansson and B. Sleeman, “Reconstruction of an acoustically sound-soft obstacle from one incident field and the far-field pattern,” *IMA Journal of Applied Mathematics*, vol. 72, no. 1, pp. 96–112, February 2007.
- [17] B. D. Sleeman, “The inverse problem of acoustic scattering,” *IMA Journal of Applied Mathematics*, vol. 29, no. 2, pp. 113–142, 1982.
- [18] O. Ivanyshyn and T. Johansson, “Nonlinear integral equation methods for the reconstruction of an acoustically sound-soft obstacle,” *Journal Integral Equations Appl.*, vol. 19, no. 3, pp. 289–308, 2007.
- [19] J. E. Dennis, Jr. and R. B. Schnabel, *Numerical methods for unconstrained optimization and nonlinear equations*, vol. 16 of *Classics in Applied Mathematics*. Philadelphia, PA: Society for Industrial and Applied Mathematics (SIAM), 1996. Corrected reprint of the 1983 original.
- [20] A. R. Conn, N. I. M. Gould, and P. L. Toint, *Trust-region methods*. MPS/SIAM Series on Optimization, Philadelphia, PA: Society for Industrial and Applied Mathematics (SIAM), 2000.
- [21] Y. Chen, “Inverse scattering via Heisenberg’s uncertainty principle,” *Inverse Problems*, vol. 13, no. 2, p. 253, 1997.
- [22] G. Bao and F. Triki, “Error Estimates for the Recursive Linearization of Inverse Medium Problems,” *Journal of Computational Mathematics*, 2010.
- [23] T. Nguyen and M. Sini, “Inverse acoustic obstacle scattering problems using multi-frequency measurements,” *Inverse Problems and Imaging*, vol. 6, no. 4, pp. 749–773, December 2012.
- [24] P. A. Martin, *Multiple Scattering Interaction of Time-Harmonic Waves with  $N$  Obstacles*. Cambridge University Press, 2006.
- [25] M. Ganesh and S. C. Hawkins, “Simulation of acoustic scattering by multiple obstacles in three dimensions,” in *Proceedings of the 14<sup>th</sup> Biennial Computational Techniques and Applications Conference, CTAC-2008* (G. N. Mercer and A. J. Roberts, eds.), vol. 50 of *ANZIAM J.*, pp. C31–C45, Sept. 2008.

- [26] O. P. Bruno, C. A. Geuzaine, J. A. Monro, Jr., and F. Reitich, “Prescribed error tolerances within fixed computational times for scattering problems of arbitrarily high frequency: the convex case,” *Philosophical Transactions of the Royal Society of London. Series A. Mathematical, Physical and Engineering Sciences*, vol. 362, no. 1816, pp. 629–645, 2004.
- [27] E. Giladi, “Asymptotically derived boundary elements for the Helmholtz equation in high frequencies,” *Journal of Computational and Applied Mathematics*, vol. 198, no. 1, pp. 52–74, 2007.
- [28] J. B. Keller, “Diffraction of a convex cylinder,” *Antennas and Propagation, IRE Transactions*, vol. 4, pp. 312–321, July 1956.
- [29] J. B. Keller, “Geometrical theory of diffraction,” *Journal of the Optical Society of America*, vol. 52, pp. 116–130, Feb 1962.
- [30] J. B. Keller, “Rays, waves and asymptotics,” *Bulletin of the American Mathematical Society*, vol. 84, no. 4, pp. 727–750, 1978.
- [31] S. Gutman and A. G. Ramm, “Support function method for inverse obstacle scattering problems,” in *Acoustics, mechanics, and the related topics of mathematical analysis*, pp. 179–184, World Sci. Publ., River Edge, NJ, 2002.
- [32] N. Bleistein and H. Richard, *Asymptotic Expansions of Integrals*. Dover Books on Mathematics Series, Dover Publications, 2010.
- [33] R. Kussmaul, “A numerical method for the exterior Neumann problem for the reduced wave equation,” *Computing*, vol. 4, pp. 246–273, 1969. 10.1007/BF02234773.
- [34] E. Martensen, “Über eine Methode zum räumlichen Neumannschen Problem mit einer Anwendung für torusartige Berandungen,” *Acta Mathematica*, vol. 109, pp. 75–135, 1963. 10.1007/BF02391810.
- [35] D. Colton and R. Kress, *Integral equation methods in scattering theory*. No. v. 1983, pt. 1 in Pure and applied mathematics, Wiley, 1983.
- [36] R. Leis, “Zur Dirichletschen Randwertaufgabe des Außenraumes der Schwingungsgleichung,” *Mathematische Zeitschrift*, vol. 90, pp. 205–211, 1965.
- [37] H. Brakhage and P. Werner, “Über das Dirichletsche Außenraumproblem für die Helmholtzsche Schwingungsgleichung,” *Archiv der Mathematik*, no. 16, pp. 325–329, 1965.
- [38] D. Colton and P. Monk, “A novel method for solving the inverse scattering problem for time-harmonic acoustic waves in the resonance region,” *SIAM J. Appl. Math.*, vol. 45, pp. 1039–1053, 1985.

- [39] D. Colton and P. Monk, “A novel method for solving the inverse scattering problem for time-harmonic acoustic waves in the resonance region ii,” *SIAM J. Appl. Math.*, vol. 46, pp. 506–523, June 1986.
- [40] A. Kirsch and R. Kress, “Two methods for solving the inverse acoustic scattering problem,” *Inverse Problems*, vol. 4, no. 3, p. 749, 1988.
- [41] R. Potthast, “A fast new method to solve inverse scattering problems,” *Inverse Problems*, vol. 12, no. 5, p. 731, 1996.
- [42] R. Kress and W. Rundell, “Inverse scattering for shape and impedance,” *Inverse Problems*, vol. 17, no. 4, p. 1075, 2001.
- [43] R. Kress and P. Serranho, “A hybrid method for two-dimensional crack reconstruction,” *Inverse Problems*, vol. 21, no. 2, p. 773, 2005.
- [44] A. Kirsch, “Characterization of the shape of a scattering obstacle using the spectral data of the far field operator,” *Inverse Problems*, vol. 14, no. 6, p. 1489, 1998.
- [45] M. Ikehata, “Reconstruction of an obstacle from the scattering amplitude at a fixed frequency,” *Inverse Problems*, vol. 14, no. 4, p. 949, 1998.
- [46] J. Hadamard, *Lectures on Cauchy’s Problem in Linear Partial Differential Equations*. Dover Phoenix Editions, Dover Publications, 2003.
- [47] J. Fan and J. Pan, “Inexact Levenberg-Marquardt method for nonlinear equations,” *Discrete Contin. Dyn. Syst. Ser. B*, vol. 4, no. 4, pp. 1223–1232, 2004.
- [48] A. Tikhonov, “Solution of incorrectly formulated problems and the regularization method,” in *Soviet Mathematics Doklady*, vol. 4, pp. 1035–1038, 1963.
- [49] A. N. Tikhonov, “Regularization of incorrectly posed problems,” 1963.
- [50] D. Colton and B. D. Sleeman, “Uniqueness theorems for the inverse problem of acoustic scattering,” *IMA Journal of Applied Mathematics*, vol. 31, no. 3, pp. 253–259, 1983.
- [51] F. Olver, *Bessel functions: Zeros and associated values*. No. pt. 3 in Royal Society mathematical tables, Published for the Royal Society at the University Press, 1960.
- [52] A. Kirsch, “The domain derivative and two applications in inverse scattering theory,” *Inverse Problems*, vol. 9, no. 1, p. 81, 1993.
- [53] C. de Boor, *A Practical Guide to Splines*. No. v. 27 in Applied Mathematical Sciences, Springer, 2001.
- [54] O. Ivanyshyn and R. Kress, “Nonlinear integral equations in inverse obstacle scattering,” 2006.
- [55] H. Walker, “Numerical methods for nonlinear equations - classnotes,” 2002.

- [56] K. Levenberg, “A method for the solution of certain problems in least squares,” *Quart. Applied Math.*, vol. 2, pp. 164–168, 1944.
- [57] D. W. Marquardt, “An Algorithm for Least-Squares Estimation of Nonlinear Parameters,” *Journal of the Society for Industrial and Applied Mathematics*, vol. 11, no. 2, pp. 431–441, 1963.
- [58] N. Yamashita and M. Fukushima, *On the Rate of Convergence of the Levenberg-Marquardt Method*.
- [59] A. Izmailov and M. Solodov, *Otimização volume 2 - Métodos Computacionais*. IMPA, 2007.
- [60] V. Isakov, *Inverse Problems for Partial Differential Equations*. No. v. 127 in Applied Mathematical Sciences, Springer, 1998.
- [61] E. Sincich and M. Sini, “Local stability for soft obstacles by a single measurement,” *Inverse Problems and Imaging*, vol. 2, no. 2, pp. 301–315, 2008.
- [62] A. Ramm, *Multidimensional inverse scattering problems*. Pitman monographs and surveys in pure and applied mathematics, Longman Scientific & Technical, 1992.
- [63] D. Gintides, “Local uniqueness for the inverse scattering problem in acoustics via the faberkrahn inequality,” *Inverse Problems*, vol. 21, no. 4, p. 1195, 2005.
- [64] W. Chew and J. Lin, “A frequency-hopping approach for microwave imaging of large inhomogeneous bodies,” *Microwave and Guided Wave Letters, IEEE*, vol. 5, pp. 439–441, December 1995.
- [65] O. M. Bucci, L. Crocco, T. Isernia, and V. Pascazio, “Inverse scattering problems with multifrequency data: reconstruction capabilities and solution strategies,” *Geoscience and Remote Sensing, IEEE Transactions on*, vol. 38, pp. 1749–1756, July 2000.
- [66] M. Abramowitz and I. Stegun, *Handbook of Mathematical Functions with Formulas, Graphs, and Mathematical Tables*. U.S. Government Printing Office, 1964.
- [67] R. Kress, *Linear Integral Equations*. No. v. 82 in Applied Mathematical Sciences, Springer, 1999.
- [68] R. Kress and I. H. Sloan, “On the numerical solution of a logarithmic integral equation of the first kind for the helmholtz equation,” *Numerische Mathematik*, vol. 66, pp. 199–214, Nov. 1993.
- [69] R. Adams and J. Fournier, *Sobolev Spaces*. No. v. 140 in Pure and Applied Mathematics, Academic Press, 2003.
- [70] L. Hörmander, *The Analysis of Linear Partial Differential Operators 1: Distribution Theory and Fourier Analysis*. Classics in Mathematics Series, Springer-Verlag GmbH, 2003.

- [71] A. Ramm, *Scattering by Obstacles*. Mathematics and its Applications, Springer, 1986.
- [72] C. B. Barber, D. P. Dobkin, and H. Huhdanpaa, “The quickhull algorithm for convex hulls,” *ACM Transactions on Mathematical Software*, vol. 22, pp. 469–483, Dec. 1996.
- [73] J. Ortega, “The Newton-Kantorovich theorem,” *The American Mathematical Monthly*, vol. 75, no. 6, pp. pp. 658–660, 1968.
- [74] L. Kantorovich and G. Forsythe, *Functional Analysis and Applied Mathematics*. NBS report, National Bureau of Standards, 1952.
- [75] L. Kantorovich and G. Akilov, *Functional Analysis in Normed Spaces*. International series of monographs in pure and applied mathematics, Pergamon Press; [distributed in the Western Hemisphere by Macmillan, New York], 1964.